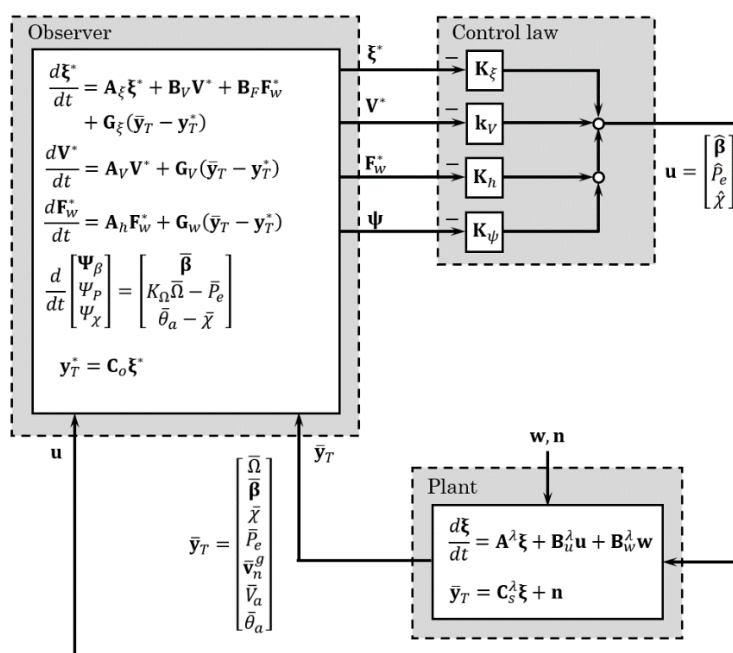# Report

Development of an LQR framework for rapid prototyping of offshore wind turbine controllers, with application to active load control

Author(s)
Karl Merz

KEYWORDS:
Wind energy
Wind turbine control

Report

Development of an LQR framework for rapid prototyping of offshore wind turbine controllers, with application to active load

VERSION	DATE
1.0	2020-03-17

AUTHOR(S)
Karl Merz

CLIENT(S)	CLIENT'S REF.
TotalControl	D3.3

PROJECT NO.	NUMBER OF PAGES/APPENDICES:
502001742	78

ABSTRACT

A linear quadradic regulator (LQR) framework has been developed for rapid prototyping of offshore wind turbine controllers. This enables the study of tradeoffs between conflicting control objectives, such as maximizing energy production, providing grid services, and reducing loads. The LQR framework is based on a linearized model of an offshore wind turbine, which is of a higher fidelity than typical control-oriented models. Nonetheless, it is shown that a controller can be quickly synthesized using this high-fidelity model. The LQR framework is applied to two case studies involving active load control: directional control of fatigue in monopile foundations, and active damping of wave-driven tower resonance when the turbine is idling.

PREPARED BY	SIGNATURE
Karl Merz	

CHECKED BY	SIGNATURE
Harald Svendsen	

APPROVED BY	SIGNATURE
Knut Samdal	

REPORT NO.	ISBN	CLASSIFICATION	CLASSIFICATION THIS PAGE
2020:00257	978-82-14-06281-6	Unrestricted	Unrestricted

Document history

VERSION	DATE	VERSION DESCRIPTION
1.0	2020-03-10	Original document

Contents

ATTACHMENTS

PROJECT
TotalControl

REPORT NUMBER
2020:00257

VERSION
1.0

3 of 78

1 Background

The dynamics of a wind turbine are to a large extent determined by its controller. The controller must provide the basic control of rotor speed and generator electric power; but it may also be called upon to assist in countering the various environmental loads on the turbine structures, as well as provide services to the electric grid, in the form of tracking an electric power command. These control objectives are partly in conflict, and there is a three-way tradeoff between production (revenue), structural loading, and actuator wear.

It is important to consider these tradeoffs when studying the system dynamics of wind turbines and wind power plants. This involves modifying the design and tuning of the wind turbine controller. Reference controllers are available (van der Hooft *et al.* 2003, Jonkman *et al.* 2009, Hansen and Henriksen 2013, Mulders and van Wingerden 2018), but these are single designs, and none of them include the complete set of features required to study all the relevant tradeoffs. It is also necessary to retune the control gains and filter parameters in order to study the tradeoffs; and, since the tuning may influence the interaction between separate control loops, then the stability properties and performance must be checked for each tuning.

Consequently, there is a need for tools to rapidly synthesize wind turbine controllers of a varied nature. Within the confines of linear systems theory, linear-quadratic (LQR) control synthesis – whether in its time-domain or $\mathcal{H}_\infty$ frequency-domain forms – provides precisely what is needed. We can establish a cost function in terms of the tradeoffs in which we are interested, and vary the relative weights. The structure and tuning of the resulting controller is then determined algorithmically, saving the repetitive manual work that would be needed with a multiple-loop proportional-integral (PI) approach.

There is a long precedence of applying linear-quadratic synthesis to wind energy systems: Liebst (1985), Wright (2004), Munteanu *et al.* (2005), Bottasso *et al.* (2013), and Fleming *et al.* (2013) are some relevant examples. When it comes to the details of the implementation, there are a wide variety of options, no single one of which is "correct": different approaches can lead to a workable controller. To a degree, then, the choice is philosophical. One thing the existing approaches have all had in common is that they have been built "bottom-up" around a minimal model of the wind turbine. The designer studies the dynamics, and selects a minimal number and type of degrees-of-freedom that approximate the plant behavior over a relevant frequency band: for instance, controller models with 2, 6, 9, and 33 states were employed in the references cited previously.

The design of controllers for complex systems may benefit from a "top-down" approach, where a high(er)-fidelity system model is employed in the tuning of gains and as a state observer. Stevens and Lewis (2003), for instance, mention a case where such an approach was necessary for model-based control of an aircraft engine. Zhou *et al.* (1996) also recommend, from the perspective of robustness, to design a controller around a refined system model, and then simplify the controller, rather than the alternative of designing the controller around a simplified system model.

We should not be critical of the use of simplified models in control design and state observation: experience has shown that these often provide good performance. However, it is of interest to explore top-down control synthesis, and the various questions that arise along the way: Is there a convenient, automated way to ensure controllability and observability? What are the practical limits of algebraic Riccati equation solvers? How can one recognize a good observer tuning? How can we understand the resulting controller gains and system response? The motivation is ultimately to apply the approach to design a wind power plant supervisory controller that can make intelligent tradeoffs between production, grid services, and wind turbine loads.

Here, as an initial investigation, we apply the top-town philosophy to a more restricted case: the design of load-rejecting control functions for a single offshore wind turbine. (Bossanyi 2003) Two themes are considered in particular. The first theme, following a recent thesis by Smilden (2019), involves the directional control of alternating loads on the foundation. Here we define the goal to "steer" the load away from a certain critical location, where there is assumed to be a material flaw.

PROJECT
TotalControl

REPORT NUMBER
2020:00257

VERSION
1.0

4 of 78

The second theme is active damping during idling, where the objective is to damp wave-driven resonant vibrations of the foundation, at some cost in electric power drawn from the grid.

We begin in Section 2 with a derivation of the wind turbine model. This is best understood in relation to the previous (Merz 2018) derivation of the aeroelastic equations in STAS. The present derivation – as well as the implementation of the equations in the accompanying software – have been streamlined, in particular by absorbing into the transformation matrices some of the "extra" terms that arise when taking time derivatives and linearizing.

One way of understanding the dynamics of complex systems is by observing how power flows and oscillates within the system: Section 2.1.9 provides the relevant theory. In particular, the steady, second-order, dissipative power can explain which elements of the system are providing the all-important dissipation of energy that causes oscillations to decay – or, if we are unlucky, where energy is being fed into the system to cause instability.

The controllers are evaluated under realistic conditions of atmospheric turbulence and ocean waves, using the spectral analysis techniques of Section 2.1.10. The control of wind turbines in a plant may include yawing with respect to the incoming wind, and the rotationally-sampled turbulence spectra have been extended in Section 2.1.11 to account for yaw.

The modal dynamics of a 10 MW offshore wind turbine (Bak *et al.* 2013, Anaya-Lara *et al.* 2018) are investigated in Section 2.3, with a particular emphasis on resonant vibration of the foundation. It is found that the relevant dynamics, including active damping, are captured by a selection of four modes. This puts the dynamics – namely, the interaction between the aeroelastic wind turbine and active load controls – within the realm of human-understandability. Some effort is made to describe in detail the modes, showing how interaction between control and plant states "blend" the modes from each.

Section 3 presents the proposed control architecture, and an abbreviated derivation is given for the solution to the optimal observer and control gains. It is this solution that constitutes the synthesis – the structure and tuning – of the controller, and the setup of the optimization problem is critical to achieving a design with favorable performance. The controller includes simplistic models of the wind and waves that act on the turbine, which give it the ability to anticipate, to some extent, the incoming disturbances.

The directional control of foundation loads is analyzed in Section 4. A series of controllers are synthesized, progressively introducing load-reduction capabilities. A biased strategy, attemping to steer the motion of the foundation in a particular direction, is compared against a strategy that attempts to reject motions in all directions. While it is possible to steer the motion to some extent, it appears that it is more practical to reject motions uniformly. It is shown – in fact, it is a natural outcome of the optimal control synthesis – that by modulating individual blade pitch the load-rejecting performance of the controller is improved.

It is demonstrated in Section 5 that both the proposed active-damping strategies can reduce resonant vibrations of the support structure, when the wind turbine is idling in low winds. The use of blade pitch offers the potential for a higher level of damping, but only when the rotor speed is above a certain minimum, roughly 0.2 rad/s. An alternate strategy using the generator can provide a smaller but still important amount of damping under low-speed rotation. Since the aerodynamic dissipation is small, it is important to tune the controller such that the generator acts both to extract energy from the oscillating tower and feed it into the rotor; and to extract energy from the rotor and feed it into the grid.

1.1 Notation and coordinate systems

(The following is a slightly modified excerpt from Merz (2018); further details can be found in that reference.)

Vectors and matrices are denoted with a bold font, for instance the state vector **x** and matrix **A**. When a vector or matrix has a certain coordinate system as a basis, then this is indicated by the use of

PROJECT
TotalControl

REPORT NUMBER
2020:00257

VERSION
1.0

5 of 78

a superscript. It may be important to keep track of two coordinate systems, one the basis in which the components of a vector are expressed, and another relative to which the vector is measured. In this case the basis is indicated by a superscript, and the relative is indicated by a slash in the subscript. Thus the position of a node $\mathbf{r}$ – that is, the vector from the origin to the node – might be measured relative to the global coordinate system, but the components expressed in a local body coordinate system; this would be written as $\mathbf{r}^B_{/g}$.

Subscripts are frequently used in other contexts as well. When a spatial vector has a subscript, for instance the induced velocity $\mathbf{V}_i$, then one of the spatial components is indicated by an additional subscript outside a parentheses; so the Z^r component of the induced velocity, a scalar, would be written $(\mathbf{V}_i)_z$. Where there is no need to be so explicit, the shorthand convention $\mathbf{v} = [v_x, v_y, v_z]$ is also used. Subscripts never denote derivatives.

The structural and aerodynamic analyses employ a variety of coordinate systems. Most of these are sketched in Fig. 1. For clarity, the following description is given as if the structure were rigid. The formulation of structural displacements (Merz 2018) allows for elastic rotations which may misalign the various coordinate systems.

The foundation coordinate system is located at the bottom node of the foundation. The X^F axis is parallel with the undisturbed ocean surface and indicates the direction of zero yaw angle; at zero yaw, the X^F axis points downwind. The Z^F axis is normal to the undisturbed ocean surface and typically passes through the center of the undeformed tower.

The tower coordinate system is located at the base of the tower, or equivalently, for offshore turbines, the top of the transition piece. In the undeformed state it is aligned with the foundation coordinate system.

The yaw coordinate system indicates the position of the yaw bearing. At zero yaw and no deformation, the yaw coordinate system is aligned with the tower and foundation coordinate systems. A positive yaw angle χ involves a rotation about the $Z^y = Z^T$ axis.

The nacelle coordinate system is aligned with the axis of rotation of the driveshaft. The Z^n axis points in the direction of the X^y axis, except that it is rotated about the Y^y axis by the driveshaft tilt angle δ: positive tilt angle raises the rotor hub. Note that the yaw coordinate system is the reference coordinate system for the nacelle structure. The "nacelle" coordinate system serves as an intermediate frame against which driveshaft rotation is measured.

Thus, the driveshaft coordinate system is rotated, with respect to the nacelle coordinate system, by the azimuth angle Ψ about the $Z^d = Z^n$ axis.

The rotorplane coordinate system is used in the aerodynamic analysis. It is aligned with the nacelle coordinate system, but has its origin at the center of the rotor hub. Quantities expressed in rotorplane coordinates have in general an "axial" component, in the Z^r direction, and a "tangential" component, which is tangent to a particular radius, for instance

$$(\mathbf{V}^r_i)_t := (\mathbf{V}^r_i)_x \sin \Psi_b + (\mathbf{V}^r_i)_y \cos \Psi_b. \tag{1}$$

This decomposition of the coordinates is convenient, because the spanwise component of relative velocity is neglected when computing aerodynamic forces.

The remaining coordinate systems occur in triplets, one associated with each blade. The hub coordinate system is not shown in Fig. 1. Its origin is the same as the rotorplane coordinate system, at the center of the rotor hub, and the X^h axis points from the axis of rotation to the pitch bearing. The hub coordinate system is aligned with the driveshaft coordinate system for Blade 1, and is rotated about the $Z^h = Z^d$ axis by the blade offset angle of $2\pi/3$ for Blade 2 and $4\pi/3$ for Blade 3.

The blade coordinate system is located at the pitch bearing. It is rotated, with respect to the hub coordinate systesm, about the $Y^h = Y^b$ axis by the blade cone angle ϕ. (The blade cone angle is not shown in Fig. 1.)

The blade pitch coordinate system is offset from the hub coordinates system by rotation about the $X^b = X^p$ axis by the *negative* of the pitch angle. The negative sign is required such that, by convention, positive pitch rotates the leading edge of the blades into the wind.

PROJECT
TotalControl

REPORT NUMBER
2020:00257

VERSION
1.0

6 of 78
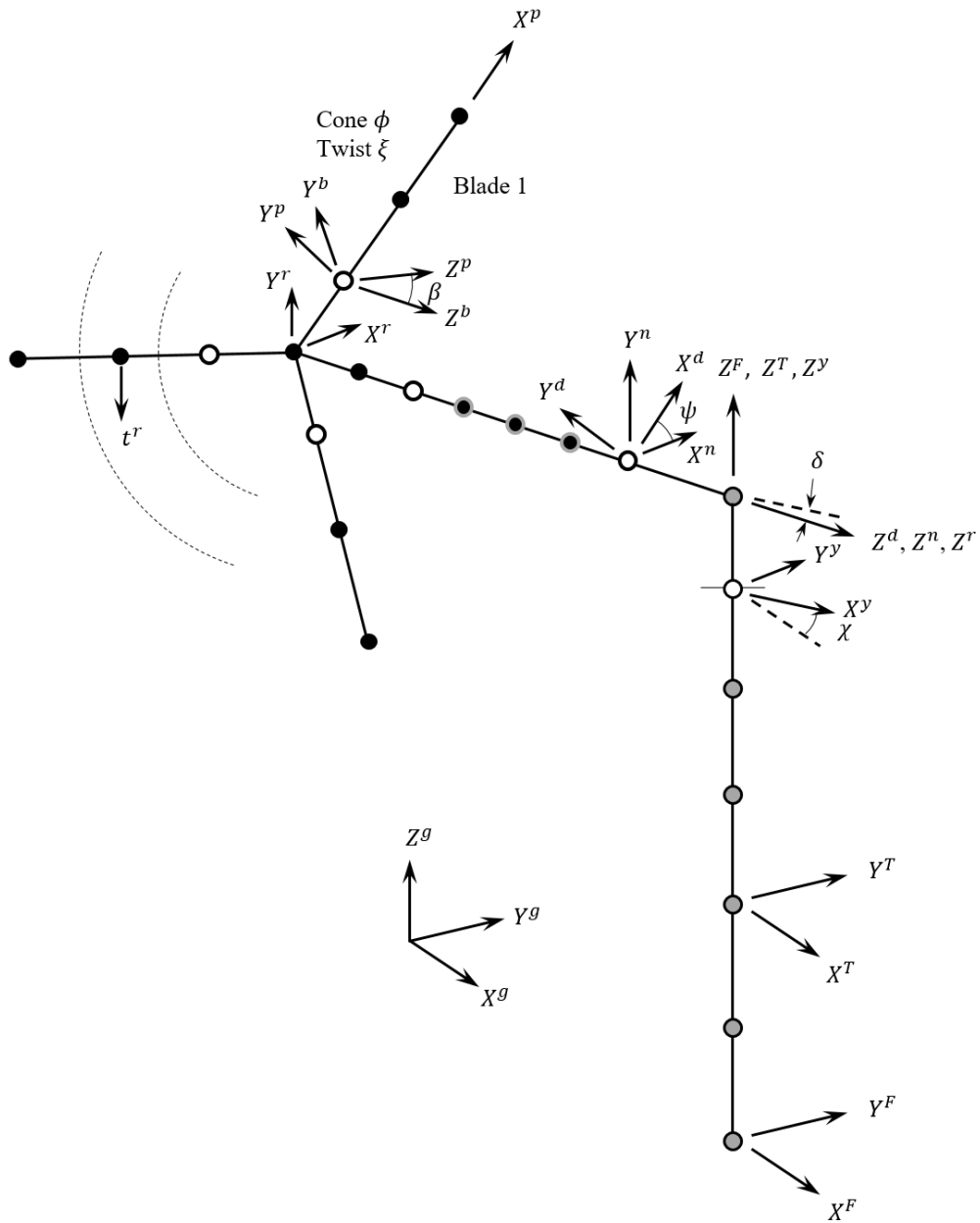
Figure 1: Important coordinate systems and angles used in the wind turbine model. The wind turbine structures are represented by finite beam elements. Rotating nodes are shown by black dots, and fixed nodes by gray dots. White dots show joints. All joints restrain 5 degrees-of-freedom, allowing one rotational degree-of-freedom, with the exception of the front driveshaft bearing, which restrains only X^n and Y^n displacements.

PROJECT
TotalControl

REPORT NUMBER
2020:00257

VERSION
1.0

7 of 78
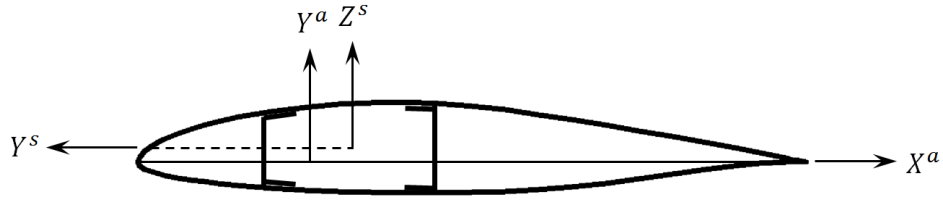
Figure 2: The airfoil and blade section coordinate systems.

There are additional coordinate systems associated with each blade element in the aerodynamic analysis. These are shown in Fig. 2. The section coordinate system is offset from the pitch coordinate system by rotation about the $X^p = X^s$ axis by the *negative* of the blade aerodynamic twist angle. The airfoil coordinate system is the traditional one used to represent lift and drag, or normal and chordwise, forces. The origin is one quarter-chord aft from the leading edge, and the X^a axis lies along the chordline.

Structural finite elements also have associated nodal and section coordinate systems; descriptions of these can be found in Merz (2018).

2 Modal dynamics of a grid-connected offshore wind turbine on a monopile foundation

Modal analysis makes the dynamics of complex systems human-understandable. The validity of the modes is limited to local perturbations about a chosen operating point; though what constitutes "local" depends on the degree of nonlinearity.[1] In any case, in the neighborhood of the operating point, the modes break the system response down into simple pieces, each of which can be studied in isolation, with their superposition providing the total response.

2.1 Theory

Let the dynamics of a system be described by the nonlinear equations

$$\mathbf{N}\frac{d\mathbf{x}}{dt} = \mathbf{f}(\mathbf{x}, \mathbf{u}), \tag{2}$$

with the dynamics in the vicinity of an operating point described by the linearized system

$$\mathbf{f}(\mathbf{x}_0, \mathbf{u}_0) = \mathbf{0}, \tag{3}$$

$$\mathbf{N}_0\frac{d\Delta\mathbf{x}}{dt} = \tilde{\mathbf{A}}\,\Delta\mathbf{x} + \tilde{\mathbf{B}}\,\Delta\mathbf{u}, \tag{4}$$

with

$$\tilde{\mathbf{A}} = \left.\frac{\partial\mathbf{f}}{\partial\mathbf{x}}\right|_0 \quad \text{and} \quad \tilde{\mathbf{B}} = \left.\frac{\partial\mathbf{f}}{\partial\mathbf{u}}\right|_0. \tag{5}$$

The $\mathbf{N}$ matrix on the left-hand side of (2) and (4) is invertible – but it is retained explicitly on the left-hand side in order to allow proper partitioning and elimination of unused degrees-of-freedom from the model, should this be necessary.[2] Let us assume that this has been done. The eigenmodes of the system are the solutions to the eigenvalue problem

$$(i\omega\mathbf{N}_0 - \tilde{\mathbf{A}})\boldsymbol{\varphi} = \mathbf{0} \tag{6}$$

---

[1]For linear systems, the modes obtained at any operating point are valid globally.

[2]The response obtained by partitioning and reducing $\mathbf{N}\,d\mathbf{x}/dt = \mathbf{f}$ is *not* the same as that obtained by striking the corresponding rows from $d\mathbf{x}/dt = \mathbf{N}^{-1}\mathbf{f}$; and it is the former result that is desired. See Merz (2019a) Section 2.7.

PROJECT
TotalControl

REPORT NUMBER
2020:00257

VERSION
1.0

8 of 78

or equivalently

$$(i\omega\mathbf{I} - \mathbf{N}_0^{-1}\tilde{\mathbf{A}})\boldsymbol{\varphi} = \mathbf{0}. \tag{7}$$

Each eigenmode – say, the kth – consists of a shape vector (eigenvector) $\boldsymbol{\varphi}_k$ and corresponding root (eigenvalue) λ_k. The unforced eigenmode evolves dynamically according to

$$\mathbf{x}_k = \boldsymbol{\varphi}_k \exp(\lambda_k t). \tag{8}$$

The shape and root may be real or complex. The eigenmode either decays exponentially, if $\Re\{\lambda_k\} < 0$, or grows exponentially, if $\Re\{\lambda_k\} > 0$. The imaginary part $\Im\{\lambda_k\}$ contains the natural frequency, if the mode is oscillatory. In this case, where $\Im\{\lambda_k\} \neq 0$, the root occurs in complex conjugate pairs, $(\boldsymbol{\varphi}_k, \lambda_k)$ and $(\boldsymbol{\varphi}_k^*, \lambda_k^*)$. The scaling of the eigenmode shapes is arbitrary, and it is most convenient if they are all scaled to unit magnitude, that is, $|\boldsymbol{\varphi}_k| = 1$.

The present wind turbine model is constructed such that there are no repeated eigenvalues, and no zero eigenvalues (pure integrators, rigid-body motion).

Laying the eigenmode shapes $\boldsymbol{\varphi}$ together, with each shape occupying a column, forms the square matrix $\boldsymbol{\Phi}$. This is invertible: let the inverse be $\boldsymbol{\Psi} = \boldsymbol{\Phi}^{-1}$. Let $\mathbf{A} = \mathbf{N}_0^{-1}\tilde{\mathbf{A}}$ and $\mathbf{B} = \mathbf{N}_0^{-1}\tilde{\mathbf{B}}$. Then the state equations take the standard form

$$\frac{d\,\Delta\mathbf{x}}{dt} = \mathbf{A}\,\Delta\mathbf{x} + \mathbf{B}\,\Delta\mathbf{u}. \tag{9}$$

The matrices $\boldsymbol{\Phi}$ and $\boldsymbol{\Psi}$ diagonalize the $\mathbf{A}$ matrix; making the substitution $\Delta\mathbf{x} = \boldsymbol{\Phi}\,\Delta\boldsymbol{\xi}$, where $\Delta\boldsymbol{\xi}$ are modal amplitudes, and premultiplying by $\boldsymbol{\Psi}$, (9) becomes

$$\frac{d\,\Delta\boldsymbol{\xi}}{dt} = \boldsymbol{\Psi}\mathbf{A}\boldsymbol{\Phi}\,\Delta\boldsymbol{\xi} + \boldsymbol{\Psi}\mathbf{B}\,\Delta\mathbf{u} = \mathbf{A}^{\lambda}\,\Delta\boldsymbol{\xi} + \boldsymbol{\Psi}\mathbf{B}\,\Delta\mathbf{u}. \tag{10}$$

Here $\mathbf{A}^{\lambda}$ is a diagonal matrix, which, if the eigenmode shapes are of unit length, contains the eigenvalues $\boldsymbol{\lambda}$ along its diagonal. Note the implication: in the absence of external inputs, each of the eigenmodes evolves independently of all the others. The eigenmodes are, however, linked by way of the input term $\boldsymbol{\Psi}\mathbf{B}\,\Delta\mathbf{u}$.

The states in (9) or (10) represent a variety of physical quantities and may be scaled differently. A glance at one of the normalized (unit-length) mode shapes $\boldsymbol{\varphi}_k$ does not reveal which states are actually active, since a dominant state may, depending on the relative scaling, appear as a small quantity $\ll 1$, and a benign state appear as a quantity close to 1. Modal *participation factors* provide the desired insight, correcting for the scaling and providing a metric that indicates the degree to which each state participates in each mode. The matrix of participation factors is computed as

$$\boldsymbol{\Pi} = \boldsymbol{\Psi}^T \circ \boldsymbol{\Phi}, \tag{11}$$

where the "$\circ$" symbol indicates elementwise multiplication (Hadamard product). The matrix of participation factors has the property that the sum along each of its rows and columns is 1. Each column corresponds to a given eigenmode, and indicates the relative participation of each state in that eigenmode. Each row, then, corresponds to the relative participation of a given state across all the eigenmodes.

Transfer functions in the frequency domain are both a convenient way to visualize the system dynamics, and a prelude to spectral analysis of the response under stochastic loading. The matrix of transfer functions between the inputs and states is

$$\frac{\partial\boldsymbol{\xi}}{\partial\mathbf{u}} = (i\omega\mathbf{I} - \mathbf{A}^{\lambda})^{-1}\boldsymbol{\Psi}\mathbf{B}. \tag{12}$$

For a particular input j and state k, this reduces to

$$\frac{\partial\boldsymbol{\xi}_k}{\partial\mathbf{u}_j} = \frac{1}{i\omega - \lambda_k}\boldsymbol{\psi}_k\mathbf{b}_j, \tag{13}$$

PROJECT
TotalControl

REPORT NUMBER
2020:00257

VERSION
1.0

9 of 78

where $\mathbf{b}_j$ is the column of the $\mathbf{B}$ matrix corresponding to the jth input. If an output equation is defined as

$$\mathbf{y} = \mathbf{C}\mathbf{x} = \mathbf{C}\boldsymbol{\Phi}\,\Delta\boldsymbol{\xi}, \tag{14}$$

then the transfer function from the jth input to m^{th} output is

$$\frac{\partial y_m}{\partial u_j} = \sum_k \frac{1}{i\omega - \lambda_k}(\mathbf{c}_m\boldsymbol{\varphi}_k)(\boldsymbol{\psi}_k\mathbf{b}_j). \tag{15}$$

Note that if y_m is defined to be a sensor output, and u_j is a control input, then $\boldsymbol{\psi}_k\mathbf{b}_j$ indicates the controllability of the kth eigenmode, and $\mathbf{c}_m\boldsymbol{\varphi}_k$ the observability. Defining

$$H_k(\omega) = \frac{1}{i\omega - \lambda_k}(\mathbf{c}_m\boldsymbol{\varphi}_k)(\boldsymbol{\psi}_k\mathbf{b}_j), \tag{16}$$

the contribution of an individual eigenmode to a given input-output transfer function, as a function of frequency, can be visualized by projecting the eigenmode's transfer function H_k into the direction of the total transfer function H:

$$\mathcal{P}_k(\omega) = \Re\left\{\frac{H_k^*(\omega)\,H(\omega)}{|H(\omega)|^2}\right\}. \tag{17}$$

In general, the matrix $\mathbf{A}^\lambda$ is complex, as is $\boldsymbol{\Psi}$, and sometimes it is convenient to convert these to real matrices. This can be done by applying the transform (Stevens and Lewis 2003)

$$\Delta\boldsymbol{\xi} = \mathbf{Y}\,\Delta\mathbf{z}, \qquad \mathbf{Y} = \frac{1}{2}\begin{bmatrix} 1 & i \\ 1 & -i \end{bmatrix}, \qquad \mathbf{Y}^{-1} = \begin{bmatrix} 1 & 1 \\ -i & i \end{bmatrix} \tag{18}$$

to each pair of complex conjugate eigenmodes; $\mathbf{Y}$ is the identity matrix for real, first-order eigenmodes. The $\mathbf{Y}$ transform converts each pair of complex conjugate eigenmodes to a pair of real modes, at the cost that the real modes are then coupled.

Letting $\mathbf{Y}$ now represent the assembly of transforms (18) spanning all of the states, the transformed state equations

$$\frac{d\,\Delta\mathbf{z}}{dt} = \mathbf{Y}^{-1}\mathbf{A}^\lambda\mathbf{Y}\,\Delta\mathbf{z} + \mathbf{Y}^{-1}\boldsymbol{\Psi}\mathbf{B}\,\Delta\mathbf{u} = \tilde{\mathbf{A}}^\lambda\Delta\mathbf{z} + \mathbf{B}^\lambda\Delta\mathbf{u} \tag{19}$$

are purely real. The $\tilde{\mathbf{A}}^\lambda$ matrix is no longer diagonal, since there are off-diagonal terms associated with the coupling of the complex-conjugate eigenmodes by the transform (19). Let us now define what we mean by a "mode", and differentiate this from an "eigenmode":

- Each pair of complex-conjugate, oscillatory eigenmodes is considered to be one second-order oscillatory mode. This definition applies both to the complex-conjugate form (8), provided that the pair of eigenmodes is considered together and operated upon simultaneously; or to the real form, coupled through the transform (19).

- Each purely-real eigenmode is considered to be one first-order mode; that is, for real eigenvalues, "mode" and "eigenmode" are synonymous.

Therefore, if there are N_r real eigenvalues and N_c complex eigenvalues, there are N_r first-order modes and $N_c/2$ oscillatory modes. When we speak of, say, the "first tower resonant mode", what is meant is the pair of eigenmodes that together form the resonant response.

PROJECT
TotalControl

REPORT NUMBER
2020:00257

VERSION
1.0

10 of 78

2.1.1 Fundamental principles of active load control

Each oscillatory mode (13) behaves dynamically as a single-degree-of-freedom oscillator. If we wish to understand the fundamentals of active load control, then it is sufficient to examine a single mass-spring-damper system as an archetype – at least, for systems whose linearized form provides a useful description of the local system dynamics. Starting with the equation of motion

$$\frac{d}{dt}\begin{bmatrix} x \\ \dot{x} \end{bmatrix} = \begin{bmatrix} 0 & 1 \\ -\omega_n^2 & -2\zeta\omega_n \end{bmatrix}\begin{bmatrix} x \\ \dot{x} \end{bmatrix} + \begin{bmatrix} 0 \\ 1 \end{bmatrix}\tilde{F}, \tag{20}$$

where $\tilde{F} = F/m$, the input-to-state transfer function is

$$\frac{\partial}{\partial\tilde{F}}\begin{bmatrix} x \\ \dot{x} \end{bmatrix} = \frac{1}{\omega_n^2 - \omega^2 + i2\zeta\omega_n\omega}\begin{bmatrix} 1 \\ i\omega \end{bmatrix}. \tag{21}$$

This transfer function has three regimes:

1. stiffness-dominated, at low frequency $\omega \ll \omega_n$;

2. resonant, when $\omega \approx \omega_n$; and,

3. mass-dominated, at high frequency $\omega \gg \omega_n$.

In the stiffness-dominated regime,

$$\frac{\partial x}{\partial\tilde{F}} \approx \frac{1}{\omega_n^2}, \tag{22}$$

so at low frequency the displacement is in-phase with the applied force. An energy budget would show the power from the applied force being stored as potential energy in the spring, and then returned, in equal quantity, to the applied force. In the mass-dominated regime,

$$\frac{\partial x}{\partial\tilde{F}} \approx -\frac{1}{\omega^2}, \tag{23}$$

so at high frequency the applied force is in-phase with, but opposing, the displacement. An energy budget would show the (small amount of) power being transferred from the applied force to the kinetic energy of the mass, and then returned in equal quantity to the applied force. At the resonant frequency,

$$\frac{\partial x}{\partial\tilde{F}} \approx -i\frac{1}{2\zeta\omega_n^2}, \tag{24}$$

and the displacement lags the applied force by 90°; the applied force is in-phase with the velocity. There is therefore net dissipation of energy. An energy budget would show a large amount of power sloshing between the kinetic energy of the mass and potential energy of the spring, and the force-times-velocity power of the applied force balancing the damping-force-times-velocity power of the dissipative elements.

With the above system dynamics in mind, we now define three types of active load control: load reduction, load rejection, and active damping. *Load reduction* is a strategy where the steady-state operating strategy of the system is altered in order to reduce the steady-state loads, displacements, and stresses. *Load rejection* involves active use of the actuators to reduce the severity of load fluctuations away from the resonant frequency, in either the stiffness-dominated or (rarely) the mass-dominated regimes. Load rejection involves producing a control signal that is in-phase with the modal displacements and applied forces – opposing them, in the stiffness-dominated regime, or augmenting them, in the mass-dominated regime. The purpose of load rejection is not to dissipate the energy; rather, it can be thought of as providing a parallel pathway for storing and returning energy, either stiffening the system, or increasing its inertia. Finally, *active damping* makes use of a control action opposing

PROJECT
TotalControl

REPORT NUMBER
2020:00257

VERSION
1.0

11 of 78

the velocity of motion, in the vicinity of the resonant frequency, in order to dissipate additional energy from the resonant oscillations.

It remains to connect the single degree-of-freedom system (20) with the more general case of an oscillatory mode. The eigenvalues of (20) are

$$\lambda = \begin{cases} -\zeta\omega_n + i\omega_n\sqrt{1-\zeta^2} \\ -\zeta\omega_n - i\omega_n\sqrt{1-\zeta^2} \end{cases} \tag{25}$$

with

$$|\lambda| = \omega_n \quad \text{and} \quad \lambda - \lambda^* = i2\omega_n\sqrt{1-\zeta^2}. \tag{26}$$

One of the possible solutions for the eigenvectors is

$$\tilde{\mathbf{\Phi}} = \frac{1}{\sqrt{1+|\lambda|^2}}\begin{bmatrix} 1 & 1 \\ \lambda & \lambda^* \end{bmatrix}, \tag{27}$$

which has an inverse

$$\tilde{\mathbf{\Psi}} = \frac{\sqrt{1+|\lambda|^2}}{\lambda - \lambda^*}\begin{bmatrix} -\lambda^* & 1 \\ \lambda & -1 \end{bmatrix}. \tag{28}$$

With $\mathbf{x} = \tilde{\mathbf{\Phi}}\boldsymbol{\xi}$, the input-to-state transfer functions for the eigenmodes are, from (13),

$$\frac{\partial\xi_k}{\partial\tilde{F}} = \frac{1}{i\omega - \lambda_k}\tilde{\boldsymbol{\psi}}_k\tilde{\mathbf{b}} = \pm\frac{1}{i\omega - \lambda_k}\left(\frac{\sqrt{1+|\lambda|^2}}{\lambda - \lambda^*}\right), \tag{29}$$

where in the latter expression we have used the fact that $\tilde{\mathbf{b}} = [0, 1]^T$.

If we extract a pair of eigenmodes from a complex system, together forming one oscillatory mode, then the equation of motion for these modes, subject to some input u, is

$$\frac{d\Delta\boldsymbol{\xi}}{dt} = \begin{bmatrix} \lambda & 0 \\ 0 & \lambda^* \end{bmatrix}\Delta\boldsymbol{\xi} + \begin{bmatrix} \boldsymbol{\psi} \\ \boldsymbol{\psi}^* \end{bmatrix}\mathbf{b}\,\Delta u. \tag{30}$$

Here the $\boldsymbol{\psi}$ vector and $\mathbf{b}$ vector represent the full system, and may have many entries. As it was possible to obtain an equation of this form from (20), it is also possible to reverse the process. Defining

$$\omega_n = |\lambda| \quad \text{and} \quad \zeta = -\frac{\Re\{\lambda\}}{\omega_n} \tag{31}$$

and using (27) and (28), an equation of precisely the form (20) is obtained, as

$$\frac{d\,\Delta\mathbf{z}}{dt} = \tilde{\mathbf{\Phi}}\begin{bmatrix} \lambda & 0 \\ 0 & \lambda^* \end{bmatrix}\tilde{\mathbf{\Psi}}\Delta\mathbf{z} + \tilde{\mathbf{\Phi}}\begin{bmatrix} \boldsymbol{\psi} \\ \boldsymbol{\psi}^* \end{bmatrix}\mathbf{b}\,\Delta u = \begin{bmatrix} 0 & 1 \\ -\omega_n^2 & -2\zeta\omega_n \end{bmatrix}\Delta\mathbf{z} + \tilde{\mathbf{\Phi}}\begin{bmatrix} \boldsymbol{\psi} \\ \boldsymbol{\psi}^* \end{bmatrix}\mathbf{b}\,\Delta u. \tag{32}$$

This equation is real, and represents an alternative version of the transform (18). With $\mathbf{z} = [z, \dot{z}]$, the "position" z and "velocity" $\dot{z}$ are orthogonal in phase. However, they are not uniquely defined, since the mapping back to physical variables,

$$\Delta\mathbf{x} = \begin{bmatrix} \boldsymbol{\varphi} & \boldsymbol{\varphi}^* \end{bmatrix}\tilde{\mathbf{\Psi}}\Delta\mathbf{z}, \tag{33}$$

still depends on the arbitrary phase chosen for the system mode shapes $\mathbf{\Phi}$ and related modal displacements $\Delta\boldsymbol{\xi}$.

PROJECT
TotalControl

REPORT NUMBER
2020:00257

VERSION
1.0

12 of 78

2.1.2 A concise derivation of the state equations for structural dynamics

The equations describing the structural dynamics of a wind turbine can be written

$$\mathbf{M}(\mathbf{q}) \, \frac{d^2\mathbf{q}}{dt^2} = \mathbf{R}(\mathbf{q}, \dot{\mathbf{q}}) + \mathbf{Q}(\mathbf{q}) \, \mathbf{F}(\mathbf{q}, \dot{\mathbf{q}}, \mathbf{x}_n, \mathbf{u}). \tag{34}$$

The degrees-of-freedom associated with (34) are denoted $\mathbf{q}$. These consist of nodal displacements and rotations. On each body, one node is designated as the reference node, and the six degrees-of-freedom associated with this node specify the global position and orientation (rotation) of the body. The remaining degrees-of-freedom specify the position and orientation, with respect to the reference node, of the other nodes on each body. These are given in the body's reference coordinate system. The details are described in Merz (2018) and need not be elaborated here; the key point is that the $\mathbf{q}$ vector consists of a mixture of multiple types of degrees-of-freedom, referring to different coordinate frames, and is therefore handled as a set of generalized coordinates. Nonetheless, the elements of $\mathbf{q}$ are lengths or angles, and the units of (34) are those of forces and moments.[3]

The left-hand side of (34) consists of the inertia matrix $\mathbf{M}$ multiplying the accelerations $d^2\mathbf{q}/dt^2$. On the right-hand side of (34) are two vectors of forces: $\mathbf{R}$, which contains internal forces, and $\mathbf{QF}$, containing external forces. The internal forces can be expanded as

$$\mathbf{R} = -\mathbf{G}(\mathbf{q}, \dot{\mathbf{q}}) + \mathbf{H}(\mathbf{q}, \dot{\mathbf{q}}) - \mathbf{D}(\mathbf{q}, \dot{\mathbf{q}}) - \mathbf{K}(\mathbf{q}), \tag{35}$$

respectively the gyroscopic, centrifugal, dissipative (damping), and stiffness forces. The external forces $\mathbf{QF}$ may be functions of the non-structural states in the system $\mathbf{x}_n$ that influence the structural forces, and system inputs $\mathbf{u}$. Also, the structural displacements and velocities may feed back as external forces; for instance, the aerodynamic forces on the wind turbine blades depend on the deformed position and motion of the blades.

2.1.3 Gravity loads

The gravitational forces on each body act as if the body were made to accelerate uniformly in the direction opposite the gravitational vector. This effect is achieved by applying the gravitational acceleration to each body's reference node; let this give a constant vector $\mathbf{g}$ of nodal accelerations. Then,

$$\mathbf{R}_g = \mathbf{M}(\mathbf{q}) \, \mathbf{g} \tag{36}$$

can be considered as a component of the right-hand side forces in (34). The structure of the mass matrix ensures that the acceleration of the reference node results in the appropriate forces on the other nodes in the body.

2.1.4 Constraints and modal transformation

The structural equations are constrained and reduced through three transformations of the degrees-of-freedom:

- the bodies in the structure (foundation, tower, nacelle, driveshaft, and blades) are linked together at fixed or rotary joints, and redundant degrees-of-freedom are eliminated;

- the nodal degrees-of-freedom are constrained to follow certain mode shapes that are computed for the structural bodies, and only a subset of these mode shapes is retained;

- dependence of the terms in (34) on the azimuth angle of the rotor is eliminated by a multi-blade coordinate transform.

---

[3]In the discussion that follows, we shall use the terms "displacements" and "forces" generically, including both linear and rotational quantities.

PROJECT
TotalControl

REPORT NUMBER
2020:00257

VERSION
1.0

13 of 78

The first of these transformations can be written as

$$\mathbf{C}(\hat{\mathbf{q}}, \mathbf{q}_s) = \mathbf{0}, \quad \text{with solution} \quad \mathbf{q} = \begin{bmatrix} \hat{\mathbf{q}} \\ \mathbf{q}_s(\hat{\mathbf{q}}) \end{bmatrix}, \tag{37}$$

where $\mathbf{C}$ is a set of nonlinear constraint equations, $\hat{\mathbf{q}}$ are the retained degrees-of-freedom, and $\mathbf{q}_s$ are the redundant (slave) degrees-of-freedom. The body-mode reduction is accomplished by the linear transformation

$$\hat{\mathbf{q}} = \boldsymbol{\Phi}\boldsymbol{\eta}, \tag{38}$$

where $\boldsymbol{\Phi}$ is a constant matrix that is computed upfront. The transformation to multi-blade coordinates is written

$$\boldsymbol{\eta} = \mathbf{T}_\psi^B(\Psi)\,\boldsymbol{\eta}^\psi, \tag{39}$$

where Ψ is the rotor azimuth angle. We have, at this point, not specified what the transformations are; but (37) through (39) fix the terminology of the transformed degrees-of-freedom. For reasons that will become apparent, we will postpone the discussion of the multi-blade coordinate transform until Section 2.1.7.

Now, (34) can be written in state-space form as

$$\begin{bmatrix} \mathbf{I} & \mathbf{0} \\ \mathbf{0} & \mathbf{M} \end{bmatrix} \frac{d}{dt} \begin{bmatrix} \mathbf{q} \\ \dot{\mathbf{q}} \end{bmatrix} = \begin{bmatrix} \dot{\mathbf{q}} \\ \mathbf{R} + \mathbf{QF} \end{bmatrix}. \tag{40}$$

We want to write (40) in terms of the states $(\boldsymbol{\eta}, \dot{\boldsymbol{\eta}})$, followed by a transformation of the equations (forces) to the same basis. Towards this end, we shall establish a sequence of two transforms

$$\mathbf{T}_\eta^q = \mathbf{T}_{\hat{q}}^q \mathbf{T}_\eta^{\hat{q}} \tag{41}$$

that are applied to the structural state equations as

$$\begin{bmatrix} \mathbf{I} & \mathbf{0} \\ \mathbf{0} & \mathbf{M} \end{bmatrix} \mathbf{T}_\eta^q \frac{d}{dt} \begin{bmatrix} \boldsymbol{\eta} \\ \dot{\boldsymbol{\eta}} \end{bmatrix} = \begin{bmatrix} \dot{\mathbf{q}} \\ \mathbf{R} + \mathbf{QF} \end{bmatrix}. \tag{42}$$

We begin with $\mathbf{T}_{\hat{q}}^q$. The variation of (37) gives

$$\frac{\partial \mathbf{C}}{\partial \mathbf{q}} \delta \mathbf{q} = \mathbf{0}. \tag{43}$$

Defining $\mathbf{L} = \partial \mathbf{C}/\partial \mathbf{q}$ and partitioning (43), we can write

$$\hat{\mathbf{L}}\,\delta\hat{\mathbf{q}} + \mathbf{L}_s \delta\mathbf{q}_s = \mathbf{0}, \tag{44}$$

or

$$\delta\mathbf{q} = \boldsymbol{\Lambda}\,\delta\hat{\mathbf{q}}, \qquad \boldsymbol{\Lambda} = \begin{bmatrix} \mathbf{I} \\ -\mathbf{L}_s\hat{\mathbf{L}} \end{bmatrix}. \tag{45}$$

As the constraint equations have no direct time dependence, it follows that their time derivative leads to

$$\frac{d\mathbf{q}}{dt} = \boldsymbol{\Lambda}(\mathbf{q}) \frac{d\hat{\mathbf{q}}}{dt}. \tag{46}$$

Furthermore,

$$\frac{d^2\mathbf{q}}{dt^2} = \boldsymbol{\Lambda}\frac{d^2\hat{\mathbf{q}}}{dt^2} + \frac{\partial\boldsymbol{\Lambda}}{\partial q_k}\frac{d\hat{\mathbf{q}}}{dt}\frac{dq_k}{dt} = \boldsymbol{\Lambda}\frac{d^2\hat{\mathbf{q}}}{dt^2} + \frac{\partial\boldsymbol{\Lambda}}{\partial q_k}\frac{d\hat{\mathbf{q}}}{dt}\boldsymbol{\Lambda}_k\frac{d\hat{\mathbf{q}}}{dt} \tag{47}$$

and we can write compactly

$$\frac{d^2\mathbf{q}}{dt^2} = \boldsymbol{\Lambda}\frac{d^2\hat{\mathbf{q}}}{dt^2} + \boldsymbol{\Gamma}\frac{d\hat{\mathbf{q}}}{dt}. \tag{48}$$

PROJECT
TotalControl

REPORT NUMBER
2020:00257

VERSION
1.0

14 of 78

It follows that

$$\mathbf{T}_{\hat{q}}^{q} = \begin{bmatrix} \mathbf{\Lambda}(\hat{\mathbf{q}}) & \mathbf{0} \\ \mathbf{\Gamma}(\hat{\mathbf{q}}, \dot{\hat{\mathbf{q}}}) & \mathbf{\Lambda}(\hat{\mathbf{q}}) \end{bmatrix}. \tag{49}$$

The body-mode transformation (38) gives simply

$$\frac{d\hat{\mathbf{q}}}{dt} = \mathbf{\Phi}\frac{d\boldsymbol{\eta}}{dt} \quad \text{and} \quad \frac{d^2\hat{\mathbf{q}}}{dt^2} = \mathbf{\Phi}\frac{d^2\boldsymbol{\eta}}{dt^2}, \tag{50}$$

leading to

$$\mathbf{T}_{\eta}^{\hat{q}} = \begin{bmatrix} \mathbf{\Phi} & \mathbf{0} \\ \mathbf{0} & \mathbf{\Phi} \end{bmatrix}. \tag{51}$$

Combining the constraints and body-mode transformation, the state equations (40) become

$$\begin{bmatrix} \mathbf{I} & \mathbf{0} \\ \mathbf{0} & \mathbf{M} \end{bmatrix} \begin{bmatrix} \mathbf{\Lambda} & \mathbf{0} \\ \mathbf{\Gamma} & \mathbf{\Lambda} \end{bmatrix} \begin{bmatrix} \mathbf{\Phi} & \mathbf{0} \\ \mathbf{0} & \mathbf{\Phi} \end{bmatrix} \frac{d}{dt} \begin{bmatrix} \boldsymbol{\eta} \\ \dot{\boldsymbol{\eta}} \end{bmatrix} = \begin{bmatrix} \mathbf{\Lambda}\mathbf{\Phi}\dot{\boldsymbol{\eta}} \\ \mathbf{R} + \mathbf{QF} \end{bmatrix}. \tag{52}$$

There are more equations than unknowns in (52), and therefore some of the equations must be eliminated.[4]

2.1.5 Virtual work and reduction of the state equations

The lower partition of the state equations (52), the momentum balance equation, has units of force. The definition of a force is a quantity that does an incremental work when subjected to an incremental displacement. The total work done by a vector of nodal forces during an incremental displacement is

$$\delta W = (\delta \mathbf{x}_{/g}^{g})^{T} \mathbf{F}^{g}. \tag{53}$$

Then,

$$\frac{\partial W}{\partial \mathbf{q}} = \frac{\partial (\mathbf{x}_{/g}^{g})^{T}}{\partial \mathbf{q}} \mathbf{T}_{B}^{g} \mathbf{F}^{B}. \tag{54}$$

Defining

$$\mathbf{Q} = \frac{\partial (\mathbf{x}_{/g}^{g})^{T}}{\partial \mathbf{q}} \mathbf{T}_{B}^{g}, \tag{55}$$

a detailed expression for which is given in Merz (2018), the (generalized) force applied to the equations of motion is $\mathbf{QF}^{B}$, or just $\mathbf{QF}$ for the time being. Note that the leading term in $\mathbf{Q}$ is a derivative of a physical displacement, relative to the global coordinate system, with respect to the degrees-of-freedom. From this it can be discerned that *forces transform, with respect to the degrees-of-freedom, like the transpose of a velocity.* This can be seen by writing

$$\mathbf{v}_{/g}^{g} = \frac{d\mathbf{x}_{/g}^{g}}{dt} = \frac{\partial \mathbf{x}_{/g}^{g}}{\partial \mathbf{q}} \frac{d\mathbf{q}}{dt}, \tag{56}$$

where the same partial derivative $\partial \mathbf{x}_{/g}^{g}/\partial \mathbf{q}$ as in (55) appears. To be explicit, if we have a change of basis (52),

$$\mathbf{q} = \mathbf{h}_0(\boldsymbol{\eta}), \qquad \frac{d\mathbf{q}}{dt} = \mathbf{\Lambda}\mathbf{\Phi}\frac{d\boldsymbol{\eta}}{dt},$$

then a force vector will transform, through the same change of basis, as

$$\mathbf{F}_{\eta} = \mathbf{\Phi}^{T}\mathbf{\Lambda}^{T}\mathbf{QF}.$$

---

[4]For our ultimate purposes of linearization and modal analysis, a minimal-state model is preferred over a Lagrange multiplier approach.

PROJECT
TotalControl

REPORT NUMBER
2020:00257

VERSION
1.0

15 of 78

The state equation (52) can then be reduced to

$$
\begin{bmatrix} \mathbf{I} & \mathbf{0} \\ \mathbf{0} & \boldsymbol{\Phi}^T \end{bmatrix}
\begin{bmatrix} \mathbf{I} & \mathbf{0} \\ \mathbf{0} & \boldsymbol{\Lambda}^T \end{bmatrix}
\begin{bmatrix} \mathbf{I} & \mathbf{0} \\ \mathbf{0} & \mathbf{M} \end{bmatrix}
\begin{bmatrix} \mathbf{I} & \mathbf{0} \\ \boldsymbol{\Gamma} & \boldsymbol{\Lambda} \end{bmatrix}
\begin{bmatrix} \mathbf{I} & \mathbf{0} \\ \mathbf{0} & \boldsymbol{\Phi} \end{bmatrix}
\frac{d}{dt}
\begin{bmatrix} \boldsymbol{\eta} \\ \dot{\boldsymbol{\eta}} \end{bmatrix}
=
\begin{bmatrix} \mathbf{I} & \mathbf{0} \\ \mathbf{0} & \boldsymbol{\Phi}^T \end{bmatrix}
\begin{bmatrix} \mathbf{I} & \mathbf{0} \\ \mathbf{0} & \boldsymbol{\Lambda}^T \end{bmatrix}
\begin{bmatrix} \dot{\boldsymbol{\eta}} \\ \mathbf{R} + \mathbf{QF} \end{bmatrix},
\qquad (57)
$$

where we have implicitly applied the operation $(\boldsymbol{\Lambda}\boldsymbol{\Phi})^{-1}$ to the upper half. The extra degrees-of-freedom are eliminated, constraining the equations and converting to a basis of body modes.[5] For short, we write

$$
(\tilde{\mathbf{T}}_\eta^q)^T
\begin{bmatrix} \mathbf{I} & \mathbf{0} \\ \mathbf{0} & \mathbf{M} \end{bmatrix}
\mathbf{T}_\eta^q \frac{d}{dt}
\begin{bmatrix} \boldsymbol{\eta} \\ \dot{\boldsymbol{\eta}} \end{bmatrix}
= (\tilde{\mathbf{T}}_\eta^q)^T
\begin{bmatrix} \boldsymbol{\Lambda}\boldsymbol{\Phi}\dot{\boldsymbol{\eta}} \\ \mathbf{R} + \mathbf{QF} \end{bmatrix},
\qquad
(\tilde{\mathbf{T}}_\eta^q)^T =
\begin{bmatrix} (\boldsymbol{\Lambda}\boldsymbol{\Phi})^{-1} & \mathbf{0} \\ \mathbf{0} & (\boldsymbol{\Lambda}\boldsymbol{\Phi})^T \end{bmatrix}.
\qquad (58)
$$

2.1.6   Modal damping

In STAS it is allowed – recommended, in fact – to apply structural damping not through the dissipative nodal force $\mathbf{D}$ in (35), but rather as a modal damping ratio. This approach avoids frequency dependence of the damping ratio, which is consistent with experimental data (Blevins 1990). Modal damping is implemented as a diagonal matrix, containing the damping factor

$$
C_\lambda = 2\zeta\sqrt{M_\lambda K_\lambda}
\qquad (59)
$$

for each mode (Merz 2018). A damping force vector, in the modal η basis, is computed as

$$
\mathbf{D}_\lambda = \mathbf{C}_\lambda \dot{\boldsymbol{\eta}}.
\qquad (60)
$$

This is appended to (58), like

$$
(\tilde{\mathbf{T}}_\eta^q)^T
\begin{bmatrix} \mathbf{I} & \mathbf{0} \\ \mathbf{0} & \mathbf{M} \end{bmatrix}
\mathbf{T}_\eta^q \frac{d}{dt}
\begin{bmatrix} \boldsymbol{\eta} \\ \dot{\boldsymbol{\eta}} \end{bmatrix}
= (\tilde{\mathbf{T}}_\eta^q)^T
\begin{bmatrix} \dot{\mathbf{q}} \\ \mathbf{R} + \mathbf{QF} \end{bmatrix}
-
\begin{bmatrix} \mathbf{0} \\ \mathbf{D}_\lambda \end{bmatrix}.
\qquad (61)
$$

2.1.7   Multi-blade coordinates and final form of the state equations

The states $\mathbf{x}$ in (2) – not only the structural states $\boldsymbol{\eta}$ and $\dot{\boldsymbol{\eta}}$ in (57), but also the other states like angles-of-attack and blade pitch commands that are associated with each blade – are transformed to multi-blade coordinates.[6] When it comes to the structural portion of the model, expressing the state equations in multi-blade coordinates eliminates the dependence on the rotor azimuth angle of the inertia matrix $\mathbf{M}$, the internal forces $\mathbf{R}$, and, ideally, the applied forces $\mathbf{QF}$. The equations then become, for practical purposes, time-invariant. Time invariance means that the equations can be solved for steady-state operating points that include the spinning rotor, and linearized with constant $\mathbf{A}$ and $\mathbf{B}$ matrices. Working in multi-blade coordinates leads to some subtleties in how the equations need to be manipulated, especially when it comes to power flow analysis (Section 2.1.9).

The multi-blade coordinate transform is

$$
\mathbf{T}_\psi^B =
\begin{bmatrix}
1 & \cos\Psi_1 & \sin\Psi_1 \\
1 & \cos\Psi_2 & \sin\Psi_2 \\
1 & \cos\Psi_3 & \sin\Psi_3
\end{bmatrix}
\quad \text{and} \quad
\mathbf{T}_B^\psi = (\mathbf{T}_\psi^B)^{-1} = \frac{1}{3}
\begin{bmatrix}
1 & 1 & 1 \\
2\cos\Psi_1 & 2\cos\Psi_2 & 2\cos\Psi_3 \\
2\sin\Psi_1 & 2\sin\Psi_2 & 2\sin\Psi_3
\end{bmatrix},
\qquad (62)
$$

such that

$$
\mathbf{z}^B = \mathbf{T}_B^\psi \mathbf{z}^\psi
\quad \text{and} \quad
\mathbf{z}^\psi = \mathbf{T}_\psi^B \mathbf{z}^B,
\quad \text{with} \quad
\mathbf{z} =
\begin{bmatrix} z_1 \\ z_2 \\ z_3 \end{bmatrix}
\qquad (63)
$$

---

[5] It would seem that premultiplying (52) by $(\mathbf{T}_\eta^q)^T$ would give a more consistent transformation. This was attempted initially, however it was observed that the resulting upper-half equations admitted incorrect steady-state solutions with nonzero rates-of-change $\dot{\boldsymbol{\eta}}$. Also, we can't multiply by $(\mathbf{T}_\eta^q)^{-1}$, because although this would result in a valid set of state equations, the momentum equations would not be in the correct basis for computing power flows (Section 2.1.9).

[6] See Merz (2015c), Bir (2008), and Johnson (1994).

PROJECT
TotalControl

REPORT NUMBER
2020:00257

VERSION
1.0

16 of 78

and z_1, z_2, and z_3 are triplets of some quantity z associated with blades 1, 2, and 3. Where a vector like $\boldsymbol{\eta}$ includes quantities associated with both the blades and other parts of the system, we can still write

$$\boldsymbol{\eta}^\psi = \mathbf{T}_B^\psi \boldsymbol{\eta}^B,$$

filling in the identity matrix for those parts of $\mathbf{T}_B^\psi$ not associated with the blades.

A question now arises: Since we are applying the multi-blade coordinate transform to a system model that includes complex interconnections between variables, how do we extend the transformation to include the whole set of variables? It may not be obvious which variables are derivatives of others. The answer is that it is not necessary to take multiple time derivatives; we can implement a straightforward version of the multi-blade coordinate transform to the state variables,

$$\mathbf{x}^B = \mathbf{T}_\psi^B \mathbf{x}^\psi, \tag{64}$$

that does not consider higher time derivatives. For justification, consider the generic nonlinear transformation

$$\mathbf{y} = \mathbf{G}(\mathbf{z})\,\mathbf{z}. \tag{65}$$

The first time derivative is

$$\frac{d\mathbf{y}}{dt} = \left(\mathbf{G}_j + \frac{\partial \mathbf{G}}{\partial z_j}\mathbf{z}\right)\frac{dz_j}{dt}, \tag{66}$$

the second time derivative is

$$\frac{d^2\mathbf{y}}{dt^2} = \left(\mathbf{G}_j + \frac{\partial \mathbf{G}}{\partial z_j}\mathbf{z}\right)\frac{d^2 z_j}{dt^2} + \left(\frac{\partial \mathbf{G}_j}{\partial z_k} + \frac{\partial \mathbf{G}_k}{\partial z_j} + \frac{\partial^2 \mathbf{G}}{\partial z_j \partial z_k}\mathbf{z}\right)\frac{dz_j}{dt}\frac{dz_k}{dt}, \tag{67}$$

and so on. As an alternative, define the variables $\dot{\mathbf{z}}'$ and $\ddot{\mathbf{z}}'$ such that

$$\frac{d\mathbf{y}}{dt} = \mathbf{G}\dot{\mathbf{z}}' \quad \text{and} \quad \frac{d^2\mathbf{y}}{dt^2} = \mathbf{G}\ddot{\mathbf{z}}'. \tag{68}$$

Note the difference between the two bases $(\mathbf{z}, \dot{\mathbf{z}}, \ddot{\mathbf{z}})$ and $(\mathbf{z}, \dot{\mathbf{z}}', \ddot{\mathbf{z}}')$: In the former case, $\dot{\mathbf{z}}$ is the rate-of-change of $\mathbf{z}$, while in the latter case, $\dot{\mathbf{y}}$ is the transformation through $\mathbf{G}$ of $\dot{\mathbf{z}}'$, and so forth for higher time derivatives. Either case leads to a valid state space representation. The "catch" is that in the latter case

$$\dot{\mathbf{z}}' \neq \frac{d\mathbf{z}}{dt}.$$

Applying the transformation (64) to (2),

$$(\mathbf{T}_{x,\psi}^x)^T \mathbf{N} \mathbf{T}_{x,\psi}^x \frac{d\mathbf{x}^\psi}{dt} = (\mathbf{T}_{x,\psi}^x)^T \mathbf{f} \tag{69}$$

or

$$(\mathbf{T}_{x,\psi}^x)^T \mathbf{N} \mathbf{T}_{x,\psi}^x \frac{d\mathbf{x}^\psi}{dt} = (\mathbf{T}_{x,\psi}^x)^T \mathbf{T}_\psi^B \mathbf{f}^\psi \tag{70}$$

with

$$\mathbf{T}_{x,\psi}^x = \mathbf{T}_\psi^B + \frac{d\mathbf{T}_\psi^B}{d\Psi}\mathbf{x}^\psi \boldsymbol{\delta}_\Omega^T. \tag{71}$$

Here $\boldsymbol{\delta}_\Omega^T$ is a row vector, with a value of 1 in the entry corresponding to the state Ω. That is, the latter term appears as a vector that adds to the column of $\mathbf{T}_\psi^B$ corresponding to the rotor speed in $d\mathbf{x}^\psi/dt$.

PROJECT
TotalControl

REPORT NUMBER
2020:00257

VERSION
1.0

17 of 78

2.1.8 Linearization of the state equations

The task at hand is to linearize (69), obtaining system state matrices $\mathbf{A}^\psi$ and $\mathbf{B}^\psi$. A key observation is that the equations

$$\mathbf{N}\frac{d\mathbf{x}}{dt} = \mathbf{f}, \quad \text{or} \quad \mathbf{N}\mathbf{T}_z^x\frac{d\mathbf{z}}{dt} = \mathbf{f}, \tag{72}$$

prior to a generic $\mathbf{x} \to \mathbf{z}$ transformation, are satisfied. When any transform is applied to both sides of (72), such as

$$(\mathbf{T}_z^x)^T\mathbf{N}\mathbf{T}_z^x\frac{d\mathbf{z}}{dt} = (\mathbf{T}_z^x)^T\mathbf{f}, \tag{73}$$

and a linearization is performed, the terms

$$\left.\frac{\partial(\mathbf{T}_z^x)^T}{\partial\mathbf{z}}\right|_0\left(\mathbf{N}_0(\mathbf{T}_z^x)_0\left.\frac{d\mathbf{z}}{dt}\right|_0\right)\Delta\mathbf{z} = \left.\frac{\partial(\mathbf{T}_z^x)^T}{\partial\mathbf{z}}\right|_0\mathbf{f}_0\Delta\mathbf{z}, \tag{74}$$

balance, and can be eliminated from the equations. In other words, *the transform of the linearized equations is identical to the linearization of the transformed equations.*

Linearization of the structural state equations (52) gives

$$\begin{bmatrix}\mathbf{I} & \mathbf{0} \\ \mathbf{0} & \mathbf{M}_0\end{bmatrix}\mathbf{T}_{\eta,0}^q\frac{d}{dt}\begin{bmatrix}\Delta\boldsymbol{\eta} \\ \Delta\dot{\boldsymbol{\eta}}\end{bmatrix} = \left(\begin{bmatrix}\mathbf{0} & \mathbf{I} \\ \mathbf{A}_{21} & \mathbf{A}_{22}\end{bmatrix} - \begin{bmatrix}\mathbf{A}_M + \mathbf{A}_T & \mathbf{A}_{\dot{T}}\end{bmatrix}\right)\mathbf{T}_{\eta,0}^q\begin{bmatrix}\Delta\boldsymbol{\eta} \\ \Delta\dot{\boldsymbol{\eta}}\end{bmatrix} + \begin{bmatrix}\mathbf{0} \\ \mathbf{Q}_0\end{bmatrix}\Delta\mathbf{F}. \tag{75}$$

with

$$\mathbf{A}_{21} = \left.\frac{\partial\mathbf{R}}{\partial\mathbf{q}}\right|_0 + \left.\frac{\partial\mathbf{Q}}{\partial\mathbf{q}}\right|_0\mathbf{F}_0, \tag{76}$$

$$\mathbf{A}_{22} = \left.\frac{\partial\mathbf{R}}{\partial\dot{\mathbf{q}}}\right|_0, \tag{77}$$

$$\mathbf{A}_M = \begin{bmatrix}\mathbf{0} & \mathbf{0} \\ \mathbf{0} & \partial\mathbf{M}_0/\partial\mathbf{q}\end{bmatrix}\mathbf{T}_{\eta,0}^q\frac{d}{dt}\begin{bmatrix}\boldsymbol{\eta} \\ \dot{\boldsymbol{\eta}}\end{bmatrix}_0 \tag{78}$$

$$\mathbf{A}_T = \begin{bmatrix}\mathbf{I} & \mathbf{0} \\ \mathbf{0} & \mathbf{M}_0\end{bmatrix}\left.\frac{\partial\mathbf{T}_\eta^q}{\partial\mathbf{q}}\right|_0\frac{d}{dt}\begin{bmatrix}\boldsymbol{\eta} \\ \dot{\boldsymbol{\eta}}\end{bmatrix}_0 \tag{79}$$

and

$$\mathbf{A}_{\dot{T}} = \begin{bmatrix}\mathbf{I} & \mathbf{0} \\ \mathbf{0} & \mathbf{M}_0\end{bmatrix}\left.\frac{\partial\mathbf{T}_\eta^q}{\partial\dot{\mathbf{q}}}\right|_0\frac{d}{dt}\begin{bmatrix}\boldsymbol{\eta} \\ \dot{\boldsymbol{\eta}}\end{bmatrix}_0. \tag{80}$$

We now consider the linearization of the multi-blade coordinate transformed state equations (69). This gives a mean equation

$$(\mathbf{T}_{x,\psi}^x)_0^T\mathbf{N}_0(\mathbf{T}_{x,\psi}^x)_0\left.\frac{d\mathbf{x}^\psi}{dt}\right|_0 = (\mathbf{T}_{x,\psi}^x)_0^T\mathbf{f}_0 \tag{81}$$

and perturbed equation

$$(\mathbf{T}_{x,\psi}^x)_0^T\mathbf{N}_0(\mathbf{T}_{x,\psi}^x)_0\frac{d\Delta\mathbf{x}^\psi}{dt} =$$

$$(\mathbf{T}_{x,\psi}^x)_0^T\left(\left.\frac{\partial\mathbf{f}}{\partial\mathbf{x}^\psi}\right|_0 - \mathbf{N}_0\left.\frac{\partial\mathbf{T}_{x,\psi}^x}{\partial\mathbf{x}^\psi}\right|_0\left.\frac{d\mathbf{x}^\psi}{dt}\right|_0 - \left.\frac{\partial\mathbf{N}}{\partial\mathbf{x}^\psi}\right|_0(\mathbf{T}_{x,\psi}^x)_0\left.\frac{d\mathbf{x}^\psi}{dt}\right|_0\right)\Delta\mathbf{x}^\psi$$

$$+ (\mathbf{T}_{x,\psi}^x)_0^T\left.\frac{\partial\mathbf{f}}{\partial\mathbf{u}^\psi}\right|_0\Delta\mathbf{u}^\psi. \tag{82}$$

PROJECT
TotalControl

REPORT NUMBER
2020:00257

VERSION
1.0

18 of 78

Noting that

$$\Delta\mathbf{x} = \mathbf{T}^x_{x,\psi}\,\Delta\mathbf{x}^\psi, \quad \text{or} \quad \frac{\partial\mathbf{x}}{\partial\mathbf{x}^\psi} = \mathbf{T}^x_{x,\psi}, \tag{83}$$

and similarly for $\mathbf{u}$, it is convenient to write the perturbed equation (82) as

$$(\mathbf{T}^x_{x,\psi})^T_0 \mathbf{N}_0 (\mathbf{T}^x_{x,\psi})_0 \frac{d\Delta\mathbf{x}^\psi}{dt} =$$
$$(\mathbf{T}^x_{x,\psi})^T_0 \left(\left.\frac{\partial\mathbf{f}}{\partial\mathbf{x}}\right|_0 - \left.\frac{\partial\mathbf{N}}{\partial\mathbf{x}}\right|_0 \left.\frac{d\mathbf{x}}{dt}\right|_0 \right)(\mathbf{T}^x_{x,\psi})_0\Delta\mathbf{x}^\psi - (\mathbf{T}^x_{x,\psi})^T_0 \mathbf{N}_0 \left.\frac{\partial\mathbf{T}^x_{x,\psi}}{\partial\mathbf{x}^\psi}\right|_0 \left.\frac{d\mathbf{x}^\psi}{dt}\right|_0 \Delta\mathbf{x}^\psi$$
$$+ (\mathbf{T}^x_{x,\psi})^T_0 \left.\frac{\partial\mathbf{f}}{\partial\mathbf{u}}\right|_0 (\mathbf{T}^u_{u,\psi})_0\Delta\mathbf{u}^\psi. \tag{84}$$

It can be recognized that

$$(\mathbf{T}^x_{x,\psi})^T_0 \mathbf{N}_0 (\mathbf{T}^x_{x,\psi})_0 \frac{d\Delta\mathbf{x}^\psi}{dt} =$$
$$(\mathbf{T}^x_{x,\psi})^T_0 \mathbf{A}(\mathbf{T}^x_{x,\psi})_0\Delta\mathbf{x}^\psi - (\mathbf{T}^x_{x,\psi})^T_0 \mathbf{N}_0 \left.\frac{\partial\mathbf{T}^x_{x,\psi}}{\partial\mathbf{x}^\psi}\right|_0 \left.\frac{d\mathbf{x}^\psi}{dt}\right|_0 \Delta\mathbf{x}^\psi + (\mathbf{T}^x_{x,\psi})^T_0 \mathbf{B}(\mathbf{T}^u_{u,\psi})_0\Delta\mathbf{u}^\psi, \tag{85}$$

where $\mathbf{A}$ and $\mathbf{B}$ come from linearizations of the equations prior to performing the multi-blade coordinate transformation. The $\mathbf{N}$ matrix term on the right-hand-side of (85) includes

$$\left.\frac{\partial\mathbf{T}^x_{x,\psi}}{\partial\mathbf{x}^\psi}\right|_0 \left.\frac{d\mathbf{x}^\psi}{dt}\right|_0 \Delta\mathbf{x}^\psi = \Omega_0 \left.\frac{d\mathbf{T}^B_\psi}{d\Psi}\right|_0 \Delta\mathbf{x}^\psi + \left(\left.\frac{d\mathbf{T}^B_\psi}{d\Psi}\right|_0 \left.\frac{d\mathbf{x}^\psi}{dt}\right|_0 + \Omega_0 \left.\frac{d^2\mathbf{T}^B_\psi}{d\Psi^2}\right|_0 \mathbf{x}^\psi_0 \right)\Delta\Psi. \tag{86}$$

To be concise we can write (85) as

$$\mathbf{N}^\psi \frac{d\Delta\mathbf{x}^\psi}{dt} = \mathbf{A}^\psi\Delta\mathbf{x}^\psi + \mathbf{B}^\psi\Delta\mathbf{u}^\psi. \tag{87}$$

2.1.9 Power flow

In studying mode shapes, and the overall response, it is of interest to know how power flows through the system. Power is rate of change of energy; (generalized) force times (generalized) velocity; torque times angular velocity; or voltage times current.

We are generally interested in power-flow analysis in order to explain features of the modal dynamics, like modes with marginal stability.[7] As such we can isolate a single mode of interest, and observe the system as it oscillates or decays in this mode.

The mechanics of the calculation are simple; but there are subtleties in how the power flows should be interpreted. To fix ideas, let us consider the linear single-degree-of-freedom oscillator (20), written in the form

$$\begin{bmatrix} 1 & 0 \\ 0 & m \end{bmatrix} \frac{d}{dt} \begin{bmatrix} x \\ \dot{x} \end{bmatrix} = \begin{bmatrix} 0 & 1 \\ -k & -c \end{bmatrix} \begin{bmatrix} x \\ \dot{x} \end{bmatrix} + \begin{bmatrix} 0 \\ 1 \end{bmatrix} F, \tag{88}$$

along with eigenvalues (25) and mode shapes (27). Power is obtained by multiplying the momentum equation, whose terms have units of force, by the velocity:

$$\dot{x}m\frac{d\dot{x}}{dt} = -\dot{x}kx - \dot{x}c\dot{x} + \dot{x}F. \tag{89}$$

Under harmonic forcing,

$$F = \hat{F}\exp(i\omega t) + \hat{F}^*\exp(-i\omega t), \quad x = \hat{x}\exp(i\omega t) + \hat{x}^*\exp(-i\omega t), \tag{90}$$

---

[7]Here we are talking about *system modes* computed for the entire wind turbine, not the body modes of (38).

PROJECT
TotalControl

REPORT NUMBER
2020:00257

VERSION
1.0

19 of 78

a generic velocity-force product like vF consists of terms like

$$vF = \hat{v}\hat{F}\exp(i2\omega t) + \hat{v}^*\hat{F}^*\exp(-i2\omega t) + \hat{v}\hat{F}^* + \hat{v}^*\hat{F}. \tag{91}$$

Integrating over a cycle, the oscillating terms disappear; the mean power is given by

$$\overline{vF} = \hat{v}\hat{F}^* + \hat{v}^*\hat{F}. \tag{92}$$

Only the component of velocity in-phase with F contributes to the mean power. Thus intuitively we should expect that under harmonic forcing the mean powers of the terms

$$\dot{x}m\frac{d\dot{x}}{dt} \quad \text{and} \quad \dot{x}kx$$

are zero, and the net power introduced by the harmonic force is dissipated in the damper.

Applying a modal transformation to (88) gives a solution in terms of the eigenmodes,

$$\frac{d}{dt}\begin{bmatrix} \xi \\ \xi^* \end{bmatrix} = \begin{bmatrix} \lambda & 0 \\ 0 & \lambda^* \end{bmatrix}\begin{bmatrix} \xi \\ \xi^* \end{bmatrix} + \tilde{\boldsymbol{\Psi}}\begin{bmatrix} 1 & 0 \\ 0 & m \end{bmatrix}^{-1}\begin{bmatrix} 0 \\ 1 \end{bmatrix}F = \begin{bmatrix} \lambda & 0 \\ 0 & \lambda^* \end{bmatrix}\begin{bmatrix} \xi \\ \xi^* \end{bmatrix} + \frac{\sqrt{1+|\lambda|^2}}{\lambda - \lambda^*}\begin{bmatrix} 1 \\ -1 \end{bmatrix}m^{-1}F, \tag{93}$$

with

$$\begin{bmatrix} \lambda & 0 \\ 0 & \lambda^* \end{bmatrix} = \tilde{\boldsymbol{\Psi}}\begin{bmatrix} 1 & 0 \\ 0 & m \end{bmatrix}^{-1}\begin{bmatrix} 0 & 1 \\ -k & -c \end{bmatrix}\tilde{\boldsymbol{\Phi}}. \tag{94}$$

What is interesting about (93) in the present context is that we no longer have an equation like $dx/dt = \dot{x}$ making the velocity naturally orthogonal to the displacement. Rather, the unforced dynamics

$$\frac{d\xi}{dt} = \lambda\xi,$$

with the mode shape

$$\boldsymbol{\varphi} = \frac{1}{\sqrt{1+|\lambda|^2}}\begin{bmatrix} 1 \\ \lambda \end{bmatrix},$$

means that the velocities within the eigenmode are *not* orthogonal to the displacements, except in the rare case where $\Re\{\lambda\} = 0$ precisely.

Returning to the form (88), let us apply a modal transformation of the states, giving

$$\begin{bmatrix} 1 & 0 \\ 0 & m \end{bmatrix}\tilde{\boldsymbol{\Phi}}\frac{d}{dt}\begin{bmatrix} \xi \\ \xi^* \end{bmatrix} = \begin{bmatrix} 0 & 1 \\ -k & -c \end{bmatrix}\tilde{\boldsymbol{\Phi}}\begin{bmatrix} \xi \\ \xi^* \end{bmatrix} + \begin{bmatrix} 0 \\ 1 \end{bmatrix}F \tag{95}$$

or

$$\frac{1}{\sqrt{1+|\lambda|^2}}\begin{bmatrix} 1 & 1 \\ m\lambda & m\lambda^* \end{bmatrix}\frac{d}{dt}\begin{bmatrix} \xi \\ \xi^* \end{bmatrix} = \frac{1}{\sqrt{1+|\lambda|^2}}\begin{bmatrix} \lambda & \lambda^* \\ -k-c\lambda & -k-c\lambda^* \end{bmatrix}\begin{bmatrix} \xi \\ \xi^* \end{bmatrix} + \begin{bmatrix} 0 \\ 1 \end{bmatrix}F. \tag{96}$$

The velocity is

$$\dot{x} = \begin{bmatrix} \varphi_v & \varphi_v^* \end{bmatrix}\begin{bmatrix} \xi \\ \xi^* \end{bmatrix} = \frac{1}{\sqrt{1+|\lambda|^2}}\begin{bmatrix} \lambda & \lambda^* \end{bmatrix}\begin{bmatrix} \xi \\ \xi^* \end{bmatrix}, \tag{97}$$

so the power-flow equation is, term-by-term,

$$\begin{bmatrix} \xi & \xi^* \end{bmatrix}\begin{bmatrix} \varphi_v \\ \varphi_v^* \end{bmatrix}m\begin{bmatrix} \varphi_v & \varphi_v^* \end{bmatrix}\frac{d}{dt}\begin{bmatrix} \xi \\ \xi^* \end{bmatrix} = \frac{m}{1+|\lambda|^2}\begin{bmatrix} \xi & \xi^* \end{bmatrix}\begin{bmatrix} \lambda^2 & \lambda\lambda^* \\ \lambda\lambda^* & (\lambda^*)^2 \end{bmatrix}\frac{d}{dt}\begin{bmatrix} \xi \\ \xi^* \end{bmatrix}, \tag{98}$$

$$-\begin{bmatrix} \xi & \xi^* \end{bmatrix}\begin{bmatrix} \varphi_v \\ \varphi_v^* \end{bmatrix}k\begin{bmatrix} \varphi_d & \varphi_d^* \end{bmatrix}\begin{bmatrix} \xi \\ \xi^* \end{bmatrix} = -\frac{k}{1+|\lambda|^2}\begin{bmatrix} \xi & \xi^* \end{bmatrix}\begin{bmatrix} \lambda & \lambda \\ \lambda^* & \lambda^* \end{bmatrix}\begin{bmatrix} \xi \\ \xi^* \end{bmatrix}, \tag{99}$$

$$-\begin{bmatrix} \xi & \xi^* \end{bmatrix}\begin{bmatrix} \varphi_v \\ \varphi_v^* \end{bmatrix}c\begin{bmatrix} \varphi_v & \varphi_v^* \end{bmatrix}\begin{bmatrix} \xi \\ \xi^* \end{bmatrix} = -\frac{c}{1+|\lambda|^2}\begin{bmatrix} \xi & \xi^* \end{bmatrix}\begin{bmatrix} \lambda^2 & \lambda\lambda^* \\ \lambda\lambda^* & (\lambda^*)^2 \end{bmatrix}\begin{bmatrix} \xi \\ \xi^* \end{bmatrix}, \tag{100}$$

PROJECT
TotalControl

REPORT NUMBER
2020:00257

VERSION
1.0

20 of 78

and

$$\begin{bmatrix} \xi & \xi^* \end{bmatrix} \begin{bmatrix} \varphi_v \\ \varphi_v^* \end{bmatrix} \begin{bmatrix} 0 \\ 1 \end{bmatrix} F = \frac{1}{\sqrt{1 + |\lambda|^2}} \begin{bmatrix} \xi & \xi^* \end{bmatrix} \begin{bmatrix} \lambda \\ \lambda^* \end{bmatrix} F. \tag{101}$$

The important thing to note here is that, under harmonic forcing, *it appears as though the mass and stiffness terms are delivering net power to the system.* The power flows from the various terms balance, and the correct net power is obtained; yet the presence of "extra" power in the equations complicates the physical interpretation of the results, when we move to a more complex system.[8]

Due to these issues, we take the strategy of examining the power flows under free decay. That is, we allow the selected mode to evolve according to

$$\frac{d}{dt} \begin{bmatrix} \xi \\ \xi^* \end{bmatrix} = \begin{bmatrix} \lambda & 0 \\ 0 & \lambda^* \end{bmatrix} \begin{bmatrix} \xi \\ \xi^* \end{bmatrix}.$$

This does not make the powers delivered by the mass and stiffness terms disappear; quite the contrary, it gives them an appropriate physical interpretation: net power flows from the kinetic and potential energies into the dissipative elements.

Let us now turn to the state equations (70), with linearization (87). Say that we have an isolated mode,

$$\Delta \mathbf{x}^\psi = \begin{bmatrix} \varphi & \varphi^* \end{bmatrix} \Delta \boldsymbol{\xi}, \qquad \Delta \boldsymbol{\xi} = \begin{bmatrix} \Delta \xi \\ \Delta \xi^* \end{bmatrix} = \begin{bmatrix} \hat{\xi} \exp \lambda t \\ \hat{\xi}^* \exp \lambda^* t \end{bmatrix}, \tag{102}$$

where (φ, φ^*) are the relevant columns from the mode shape matrix $\mathbf{\Phi}$; also let (ψ, ψ^*) be the corresponding rows from the inverse mode shape matrix $\mathbf{\Psi}$. The amplitude and phase of $\hat{\xi}$ is arbitrary, and can be chosen such that a convenient state or output variable is of unit magnitude and zero phase. The equation of motion for free decay is

$$\mathbf{N}^\psi \frac{d\Delta \mathbf{x}^\psi}{dt} = \mathbf{A}^\psi \Delta \mathbf{x}^\psi, \tag{103}$$

or applying the modal transformation (102),

$$\mathbf{N}^\psi \begin{bmatrix} \varphi & \varphi^* \end{bmatrix} \frac{d\Delta \boldsymbol{\xi}}{dt} = \mathbf{A}^\psi \begin{bmatrix} \varphi & \varphi^* \end{bmatrix} \Delta \boldsymbol{\xi}, \tag{104}$$

such that

$$\frac{d\Delta \boldsymbol{\xi}}{dt} = \begin{bmatrix} \psi \\ \psi^* \end{bmatrix} (\mathbf{N}^\psi)^{-1} \mathbf{A}^\psi \begin{bmatrix} \varphi & \varphi^* \end{bmatrix} \Delta \boldsymbol{\xi} = \begin{bmatrix} \lambda & 0 \\ 0 & \lambda^* \end{bmatrix} \begin{bmatrix} \xi \\ \xi^* \end{bmatrix}. \tag{105}$$

We can extract the rows of (104) corresponding to the structural dynamics. Let

$$\varphi = \begin{bmatrix} \varphi_d \\ \varphi_v \\ \varphi_s \end{bmatrix}, \tag{106}$$

where φ_d is associated with the generalized displacements $\Delta \boldsymbol{\eta}^\psi$, φ_v the generalized velocities $\Delta \dot{\boldsymbol{\eta}}^\psi$, and φ_s the other system states. Then, the structural equations of motion take the form[9]

$$\mathbf{M}^\psi \begin{bmatrix} \lambda \varphi_v & \lambda^* \varphi_v^* \end{bmatrix} \begin{bmatrix} \Delta \xi \\ \Delta \xi^* \end{bmatrix} = -\mathbf{K}^\psi \begin{bmatrix} \varphi_d & \varphi_d^* \end{bmatrix} \begin{bmatrix} \Delta \xi \\ \Delta \xi^* \end{bmatrix} - \boldsymbol{\mathcal{D}}^\psi \begin{bmatrix} \varphi_v & \varphi_v^* \end{bmatrix} \begin{bmatrix} \Delta \xi \\ \Delta \xi^* \end{bmatrix} + \mathbf{A}_s^\psi \begin{bmatrix} \varphi_s & \varphi_s^* \end{bmatrix} \begin{bmatrix} \Delta \xi \\ \Delta \xi^* \end{bmatrix}. \tag{107}$$

---

[8]This caused the author quite some confusion during initial investigations, isolating a mode and looking at the power term-by-term: why were selected springs and masses delivering a steady power to the system, under constant-amplitude harmonic motion?

[9]Please do not confuse the dissipative matrix $\boldsymbol{\mathcal{D}}^\psi$ with the $\mathbf{D}^\psi$ matrix in the full state equations.

PROJECT
TotalControl

REPORT NUMBER
2020:00257

VERSION
1.0

21 of 78

Multiplying by the generalized velocities gives the modal power equation

$$
-\begin{bmatrix} \Delta\xi & \Delta\xi^* \end{bmatrix} \begin{bmatrix} \boldsymbol{\varphi}_v^T \\ (\boldsymbol{\varphi}_v^*)^T \end{bmatrix} \mathbf{M}^\psi \begin{bmatrix} \lambda\boldsymbol{\varphi}_v & \lambda^*\boldsymbol{\varphi}_v^* \end{bmatrix} \begin{bmatrix} \Delta\xi \\ \Delta\xi^* \end{bmatrix} - \begin{bmatrix} \Delta\xi & \Delta\xi^* \end{bmatrix} \begin{bmatrix} \boldsymbol{\varphi}_v^T \\ (\boldsymbol{\varphi}_v^*)^T \end{bmatrix} \mathbf{K}^\psi \begin{bmatrix} \boldsymbol{\varphi}_d & \boldsymbol{\varphi}_d^* \end{bmatrix} \begin{bmatrix} \Delta\xi \\ \Delta\xi^* \end{bmatrix}
$$

$$
-\begin{bmatrix} \Delta\xi & \Delta\xi^* \end{bmatrix} \begin{bmatrix} \boldsymbol{\varphi}_v^T \\ (\boldsymbol{\varphi}_v^*)^T \end{bmatrix} \boldsymbol{\mathcal{D}}^\psi \begin{bmatrix} \boldsymbol{\varphi}_v & \boldsymbol{\varphi}_v^* \end{bmatrix} \begin{bmatrix} \Delta\xi \\ \Delta\xi^* \end{bmatrix} + \begin{bmatrix} \Delta\xi & \Delta\xi^* \end{bmatrix} \begin{bmatrix} \boldsymbol{\varphi}_v^T \\ (\boldsymbol{\varphi}_v^*)^T \end{bmatrix} \mathbf{A}_s^\psi \begin{bmatrix} \boldsymbol{\varphi}_s & \boldsymbol{\varphi}_s^* \end{bmatrix} \begin{bmatrix} \Delta\xi \\ \Delta\xi^* \end{bmatrix} = \mathbf{0}. \quad (108)
$$

With this sign convention, once the terms in (108) are expanded into their numerical values, a positive number means "power is leaving the term", and a negative number means "power is entering the term."

The dissipated power is of particular interest, as this shows which elements are providing modal stability. If we draw a control surface around the wind turbine, it is primarily the aerodynamic forces and generator torque that are responsible for the damping of structural modes (positive or negative!), with soil, hydrodynamic, and structural damping providing a secondary contribution. To isolate these effects requires that we reformulate (108), in the form of (34), with nodal displacements and forces as a basis. Getting there is straightforward, since we have

$$
\begin{bmatrix} \Delta\mathbf{q} \\ \Delta\dot{\mathbf{q}} \end{bmatrix} = \mathbf{T}_\eta^q\big|_0 \, \mathbf{T}_{x,\psi}^\eta\big|_0 \begin{bmatrix} \boldsymbol{\varphi} & \boldsymbol{\varphi}^* \end{bmatrix} \Delta\boldsymbol{\xi}, \quad (109)
$$

and

$$
\frac{d}{dt}\begin{bmatrix} \Delta\mathbf{q} \\ \Delta\dot{\mathbf{q}} \end{bmatrix} = \left(\mathbf{T}_{x,\psi}^q\big|_0 \begin{bmatrix} \lambda\boldsymbol{\varphi} & \lambda^*\boldsymbol{\varphi}^* \end{bmatrix} + \frac{\partial\mathbf{T}_{x,\psi}^q}{\partial\mathbf{x}^\psi}\bigg|_0 \frac{d\mathbf{x}^\psi}{dt}\bigg|_0 \begin{bmatrix} \boldsymbol{\varphi} & \boldsymbol{\varphi}^* \end{bmatrix} \right) \Delta\boldsymbol{\xi}. \quad (110)
$$

In the common case of linearization about an equilibrium point,

$$
\frac{d\mathbf{x}^\psi}{dt}\bigg|_0 = \mathbf{0},
$$

which simplifies (110).

2.1.10 Spectral analysis of stochastic loads

Random signals are often represented as spectra in the frequency domain, for purposes of engineering calculations. It is assumed that the stochastic processes in question are stationary and Gaussian.[10] With these assumptions, the joint probability distribution is a multivariate Gaussian, and its properties are fully described by a mean value and a covariance. Since the systems under consideration are linear, we can restrict the discussion to a pair of stochastic signals; the effects of additional signals can be obtained by considering all permutations of pairs in turn.

Consider then a pair of signals $s_1(t)$ and $s_2(t)$, which may be the same (a signal and itself) or different. It is not so important at first that the signals are Gaussian; what is important is that we are looking to characterize the mean value of each signal, and the covariance between the signals as a function of the time offset τ between two points. (Stationarity ensures us that the result will be the same regardless of which two points are chosen.) The covariance is

$$
Q_{12}(\tau) = E[(s_1(t) - \bar{s}_1)(s_2(t+\tau) - \bar{s}_2)], \quad (111)
$$

where the expected value is taken over the time t. The spectrum is the Fourier transform, in τ, of the covariance function,

$$
S_{12}(f) = \int_{-\infty}^{\infty} Q_{12}(\tau) \exp(-i2\pi f\tau)\, d\tau. \quad (112)
$$

---

[10]A thorough treatment of the theory is out of the question, as it involves the mathematics of multivariable probability and Fourier analysis, and its application contains many subtleties – for instance, why is it reasonable to approximate non-stationary, non-Gaussian stochastic phenomena like atmospheric turbulence and ocean waves as stationary Gaussian processes?

PROJECT
TotalControl

REPORT NUMBER
2020:00257

VERSION
1.0

22 of 78

In numerical calculations of stochastic processes like turbulence and ocean waves, we may be given many realizations (or one long realization) of $s_1(t)$ and $s_2(t)$, in which case the spectrum can be computed via (111) and (112). Alternatively, it may be possible to formulate an expression for $Q_{12}(\tau)$ or $S_{12}(f)$ theoretically. In the STAS program, the ocean wave force spectra are obtained by the former approach, and the rotationally-sampled turbulence spectra by the latter (Merz 2015a).

In either case, the numerical implementation deals with discrete timesteps and discrete frequencies. We illustrate the process that begins with realizations (time series) because this is the most general. Let the signals represent the inputs $\mathbf{u}$ to a linear dynamic system, with mean value $\mathbf{u}_0$ and perturbations $\Delta\mathbf{u}$. These inputs are defined at $N/2$ timesteps $p\Delta t$, with p the set of integers $0 \le p \le N/2 - 1$.

We take the signal and mirror it in time, such that it is periodic over N steps, $-N/2 \le p \le N/2-1$. We then perform a Fourier transform, obtaining the coefficients $\boldsymbol{v}$ on a representation of the signal of the form

$$\Delta\mathbf{u} = \sum_{k=-N/2}^{N/2-1} \boldsymbol{v}_k \exp(-i2\pi\, kp/N). \tag{113}$$

In the exponential, we have employed the relationship

$$\Delta f = \frac{1}{N\Delta t} \tag{114}$$

such that

$$\exp(\mp i2\pi\, k\Delta f\, p\Delta t) = \exp(\mp i2\pi\, kp/N). \tag{115}$$

Since the time signal is real, $\boldsymbol{v}_{-k} = \boldsymbol{v}_k^*$.

The covariance matrix is

$$\mathbf{Q}_u(m\Delta\tau) = E[\Delta u(p\Delta t)\, \Delta u(p\Delta t + m\Delta\tau)]. \tag{116}$$

Using (113), and the definition of expected value,

$$\mathbf{Q}_u(m\Delta\tau) = \frac{1}{N} \sum_{p=-N/2}^{N/2-1} \left\{ \left(\sum_{j=-N/2}^{N/2-1} \boldsymbol{v}_j \exp(-i2\pi\, jp/N) \right) \left(\sum_{k=-N/2}^{N/2-1} \boldsymbol{v}_k^T \exp(-i2\pi\, k(p+m)/N) \right) \right\}. \tag{117}$$

For a given j, when summed over p, the product in braces is zero except when $k = -j$. In this case,

$$\mathbf{Q}_u(m\Delta\tau) = \frac{1}{N} \sum_{j=-N/2}^{N/2-1} \boldsymbol{v}_j \boldsymbol{v}_j^{*T} \exp(i2\pi\, jm/N) \sum_{p=-N/2}^{N/2-1} (1) = \sum_{j=-N/2}^{N/2-1} \boldsymbol{v}_j \boldsymbol{v}_j^{*T} \exp(i2\pi\, jm/N). \tag{118}$$

The spectral matrix is the Fourier transform of (118) in τ,

$$\mathbf{S}_u(k\Delta f) = \Delta t \sum_{m=-N/2}^{N/2-1} \sum_{j=-N/2}^{N/2-1} \boldsymbol{v}_j \boldsymbol{v}_j^{*T} \exp(i2\pi\, jm/N) \exp(-i2\pi\, km/N). \tag{119}$$

This is zero, except when $j = k$, in which case

$$\mathbf{S}_u(k\Delta f) = \boldsymbol{v}_k \boldsymbol{v}_k^{*T}\, \Delta t \sum_{m=-N/2}^{N/2-1} (1) = N\Delta t\, \boldsymbol{v}_k \boldsymbol{v}_k^{*T} = \frac{1}{\Delta f} \boldsymbol{v}_k \boldsymbol{v}_k^{*T}. \tag{120}$$

In other words, *the spectral matrix is the outer product of the signals' Fourier coefficients with their complex conjugate*, divided by the width of the frequency bin $\Delta f = 1/(N\Delta t)$.

PROJECT
TotalControl

REPORT NUMBER
2020:00257

VERSION
1.0

23 of 78

As a sanity check, we know that the area under the spectrum of a signal should equal its variance, which in turn should equal $Q(0)$ by definition. From (118) we see that

$$\mathbf{Q}_u(0) = \sum_{j=-N/2}^{N/2-1} \boldsymbol{\upsilon}_j \boldsymbol{\upsilon}_j^{*T}. \tag{121}$$

Indeed, integrating (120) over frequency gives the identical result

$$\Delta f \sum_{k=-N/2}^{N/2-1} \mathbf{S}_u(k\Delta f) = \sum_{k=-N/2}^{N/2-1} \boldsymbol{\upsilon}_k \boldsymbol{\upsilon}_k^{*T}. \tag{122}$$

If a transfer function $\mathbf{H}(f) = \mathbf{H}(k\Delta f) = \mathbf{H}_k$ is defined, such that

$$\Delta \mathbf{y} = \sum_{k=-N/2}^{N/2-1} \mathbf{H}_k \boldsymbol{\upsilon}_k \exp(-i2\pi\, kp/N), \tag{123}$$

then it is seen that the spectral matrix transforms as

$$\mathbf{S}_y(k\Delta f) = \mathbf{H}_k \mathbf{S}_u(k\Delta f)\, \mathbf{H}_k^{*T}. \tag{124}$$

2.1.11 Rotationally-sampled turbulence spectra in multi-blade coordinates

Atmospheric turbulence is input to the STAS turbine model as a spectral matrix. The matrix contains the cross-spectra for every component of turbulence at every blade element, in the global coordinate frame, transformed into multi-blade coordinates. That is,

$$\mathbf{S}_v^\psi(f) = \mathbf{S}^\psi(\mathbf{v}_{j/g}^g, \mathbf{v}_{k/g}^g, f) \tag{125}$$

for all pairs (j, k) of blade elements. As a simplification, these spectra are generated without taking account of the way in which the wind turbine wake and induction field at the rotor distort the atmospheric turbulence.

Since the blades are rotating, this motion is included, assuming a constant rotational speed, in the spectra: they are *rotationally sampled* spectra. This can be formulated analytically for isotropic turbulence, which is assumed here. Alternatively, spectra can be generated from time series using (113) through (120), sampling rotating paths traced through a grid of turbulence. The latter time-series approach can capture a more realistic turbulence field, whereas the analytical approach has the advantage of being numerically smooth, employing no random numbers. Note that it is possible to scale a set of spectra, within reason, to different wind speeds and rotor speeds; see Merz *et al.* (2019).

The present version of the STAS Aeroelastic module (Merz 2018) accepts wind inputs in the global coordinate frame. This allows arbitrary blade deformations and yaw or tilt misalignments to be considered, within the bounds of validity of the blade element momentum method. When there is some asymmetry in the flow relative to the rotor, be this yaw, wind shear, or partial-wake conditions, the resulting flow velocities seen by a blade are composed – conceptually, though not always in reality – of three components:

1. the steady-state flow pattern about the rotor;

2. a periodic signal obtained as the blade rotates through the asymmetries in the steady-state flow pattern; and

3. a stochastic signal as the blade rotates through the fluctuating turbulence field associated with the flow.

PROJECT
TotalControl

REPORT NUMBER
2020:00257

VERSION
1.0

24 of 78

Provided that the geometry and flow patterns do not change much – that is, for small perturbations about the steady-state yaw orientation and flow patterns – items (2) and (3) can be implemented as part of the rotationally-samped turbulence spectra, generated upfront.

The development proceeds in seven steps:

1. Formulate covariance functions for atmospheric turbulence, as a function of the $(\mathbf{v}^g)_x, (\mathbf{v}^g)_y, (\mathbf{v}^g)_z$ component and distance of separation between points. In the present treatment, this is done analytically with help from the theory of isotropic turbulence.

2. Formulate the paths traced through the *combined mean and turbulent* flow fields by each blade element.

3. Obtain the rotationally-sampled covariance functions $\mathbf{Q}_v(\tau)$ for $(\mathbf{v}^g)_x, (\mathbf{v}^g)_y, (\mathbf{v}^g)_z$ turbulent velocity components, experienced by the rotating blades.

4. Take the numerical Fourier transform of the covariance functions to get the turbulence spectra $\mathbf{S}_v(f)$.

5. Compute the periodic time series associated with the mean flow field around one full rotor rotation. The mean flow field includes yaw misalignment, wind shear, and tower shadow effects.

6. Take the numerical Fourier transform of the time series and apply (120) to obtain the spectra $\mathbf{S}_V(f)$ for the mean flow.

7. Perform the multi-blade coordinate transform of the spectral matrices. The separate spectra for turbulence and mean flow can be superposed to obtain the total spectra, $\mathbf{S}_v^\psi(f) + \mathbf{S}_V^\psi(f)$.

The covariance functions chosen to represent atmospheric turbulence are those described by Merz (2015a), based on Connell (1982) and Kristensen and Frandsen (1982). The point-to-point covariance function for isotropic turbulence, following the Von Karman spectrum, is

$$Q_{ss}(s,0) = \frac{2\sigma_v^2}{\Gamma(1/3)} \left(\frac{s}{2.68L_u} \right) K_{1/3} \left(\frac{s}{1.34L_u} \right), \tag{126}$$

with derivative

$$\frac{dQ_{ss}(s,0)}{ds} = -\left(\frac{2\sigma_v^2}{\Gamma(1/3)} \right) \left(\frac{1}{1.34L_u} \right) \left(\frac{s}{2.68L_u} \right)^{1/3} K_{-2/3} \left(\frac{s}{1.34L_u} \right). \tag{127}$$

Here

$$s = |\mathbf{s}| = \sqrt{s_x^2 + s_y^2 + s_z^2} \tag{128}$$

is a distance in space, σ_v^2 is the single-point variance in the turbulence field, L_u is a length scale, which tends to be on the order of 100 to 200 m for the lower atmospheric boundary layer, Γ is the gamma function, and K is the modified Bessel function of the second kind. The spatial correlations between turbulence at any two points are (Davidson 2004)

$$Q_{jj}(s,0) = Q_{ss}(s,0) + \frac{s}{2} \frac{dQ_{ss}(s,0)}{ds} - \frac{s_j^2}{2s} \frac{dQ_{ss}(s,0)}{ds} \tag{129}$$

for velocity components in the same direction, and

$$Q_{jk}(s,0) = -\frac{s_j s_k}{2s} \frac{dQ_{ss}(s,0)}{ds} \tag{130}$$

for orthogonal components.

PROJECT
TotalControl

REPORT NUMBER
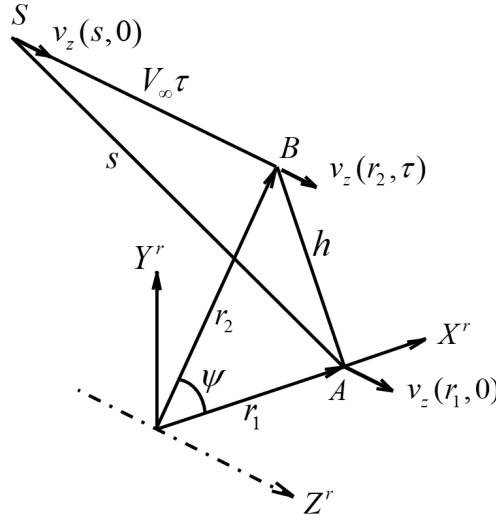2020:00257

VERSION
1.0

25 of 78

Figure 3: An idealized geometry illustrating how the assumptions of frozen turbulence and uniform convection velocity can be used to convert time separation in τ to spatial separation at the initial time $t = 0$.

If one knows the path traced by a particle relative to the features in the turbulence – which for purposes of analyzing a single wind turbine can be assumed to be frozen in time and convected at the mean hub-height wind speed – then s_x, s_y, and s_z relative to a second particle can be formulated, and (129) and (130) used to compute the covariance functions. Figure 3 shows an example that illustrates the basic idea. Here we wish to find the covariance between the v_z component of wind at radial coordinate r_1 and the same component at coordinate r_2, at time τ. Between $t = 0$ and $t = \tau$, the blade has rotated through an angle $\psi = \Omega\tau$, and the wind has convected a distance $V_\infty\tau$. Therefore, the covariance between $v_z(r_1, 0)$ and $v_z(r_2, \tau)$ is the same as that between $v_z(0, 0)$ and $v_z(s, 0)$, with s *upstream* of (r_2, τ) by a distance $V_\infty\tau$, as shown in the figure.

Figure 3 is a somewhat idealized case where the flow and the global coordinate system are aligned with the rotor plane. Figure 4, on the other hand, shows the more general case. Given some coordinate system with its origin on the axis of rotation, and assuming that the deformed shape of the blades does not change significantly around the azimuth,[11] such that its only motion is to revolve rigidly about the axis of rotation, the position of a point on one of the blades at time τ can be written

$$\mathbf{r}^g_{p/g}(\tau) = \mathbf{O}^g_{r/g} + \mathbf{T}^g_y \mathbf{T}^y_n \mathbf{T}^n_d(\psi)\, \mathbf{r}^d_{p/r}, \qquad \psi = \Omega\tau. \tag{131}$$

The driveshaft coordinate system rotates with the blades, and the transform $\mathbf{T}^n_d(\psi)$ is the only variable quantity: the vectors $\mathbf{O}^g_{r/g}$ and $\mathbf{r}^d_{p/d}$, and the transforms $\mathbf{T}^y_n$ (nacelle to yaw) and $\mathbf{T}^g_y$ (yaw to global), are constant. The vector $\mathbf{s}^g$ is then

$$\mathbf{s}^g(\tau) = \mathbf{r}^g_{2/g}(\tau) - \mathbf{r}^g_{1/g}(0) - \mathbf{V}^g_\infty\tau. \tag{132}$$

Using (131),

$$\mathbf{s}^g(\tau) = \mathbf{T}^g_y \mathbf{T}^y_n \left[\mathbf{T}^n_d(\psi)\, \mathbf{r}^d_{2/r} - \mathbf{T}^n_d(0)\, \mathbf{r}^d_{1/r} \right] - \mathbf{V}^g_\infty\tau. \tag{133}$$

Wind shear and tower shadow are, we assume, periodic and deterministic effects associated with the mean flow. Nonetheless, their correlation functions and spectra can be computed and superposed with those of the turbulence. Figure 5 illustrates the concept. At right is a sketch of the 2D potential flow field around the tower, along a two-dimensional plane orthogonal to the tower centerline.[12] This

---

[11]Given that the length scale of the turbulence is on the order of 100 m, it is difficult to imagine that the blades could deflect by an amount that would significantly influence the covariance function.

[12]The profile computed by potential theory is valid upwind, but not directly downwind, of the tower.

PROJECT
TotalControl

REPORT NUMBER
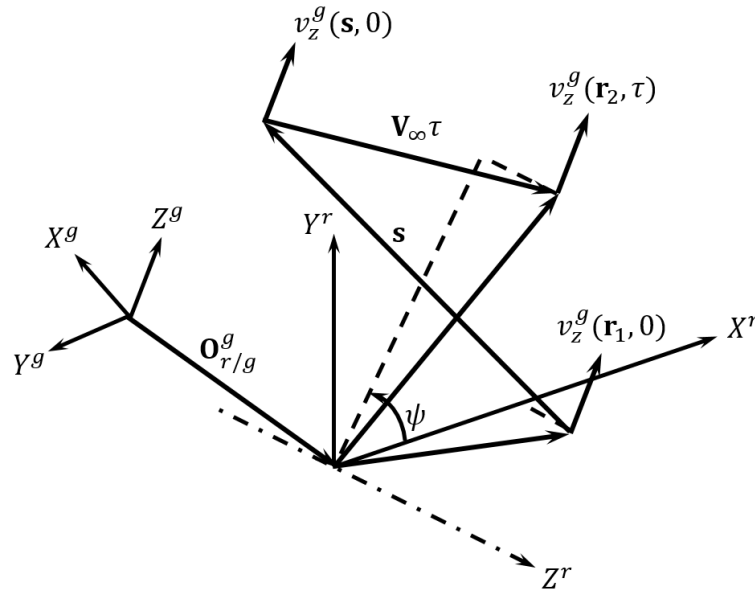2020:00257

VERSION
1.0

26 of 78

Figure 4: The general case where neither the points, the wind, nor the global coordinate system are aligned with the rotorplane.

is defined relative to a wind coordinate system, whose X^w axis is aligned with the wind direction; it is assumed that the tilt in the flow relative to the tower is small. The Z^d axis (driveshaft coordinate system) indicates the rotor's axis of rotation. A point on one of the blades, located at $\mathbf{r}^d$ relative to the driveshaft coordinate system, describes a circle, revolving about the Z^d axis. This is seen from above in the figure at right (which is simplified, since the plane of rotation need not be perfectly in-line with the tower) and from the front in the figure at left. We want to know the vector $\mathbf{s}$ from the tower centerline, at the height where the blade element passes, to the location of the blade element, shown as a white circle.

The stream function for the potential flow field about a cylinder, in wind coordinates, with ($x = 0, y = 0$) at the tower centerline, is (Burton *et al.* 2001)

$$\phi = V_\infty y \left(1 - \frac{D^2}{4(x^2 + y^2)} \right). \tag{134}$$

Velocity components are then

$$(\mathbf{V}_t^w)_x = \frac{\partial \phi}{\partial y} = V_\infty \left[1 - \left(\frac{D^2}{4} \right) \frac{x^2 - y^2}{(x^2 + y^2)^2} \right] \tag{135}$$

and

$$(\mathbf{V}_t^w)_y = -\frac{\partial \phi}{\partial x} = -V_\infty \left(\frac{D^2}{2} \right) \frac{xy}{(x^2 + y^2)^2}. \tag{136}$$

For purposes of the covariance, we want not the total velocity, but the perturbation with respect to the mean flow; this is

$$(\mathbf{v}_t^w)_x = (\mathbf{V}_t^w)_x - V_\infty = -V_\infty \left(\frac{D^2}{4} \right) \frac{x^2 - y^2}{(x^2 + y^2)^2}, \tag{137}$$

with $(\mathbf{v}_t^w)_y = (\mathbf{V}_t^w)_y$.

The vector $\mathbf{s}^g$ can be written

$$\mathbf{s}^g = \mathbf{T}_y^g \mathbf{T}_n^y \mathbf{T}_d^n(\psi) \mathbf{r}_{p/r}^d - \mathbf{T}_y^g \begin{bmatrix} 0 \\ 0 \\ \{\mathbf{T}_n^y \mathbf{T}_d^n(\psi_0) \mathbf{r}_{p/r}^d\}_z \end{bmatrix} \tag{138}$$
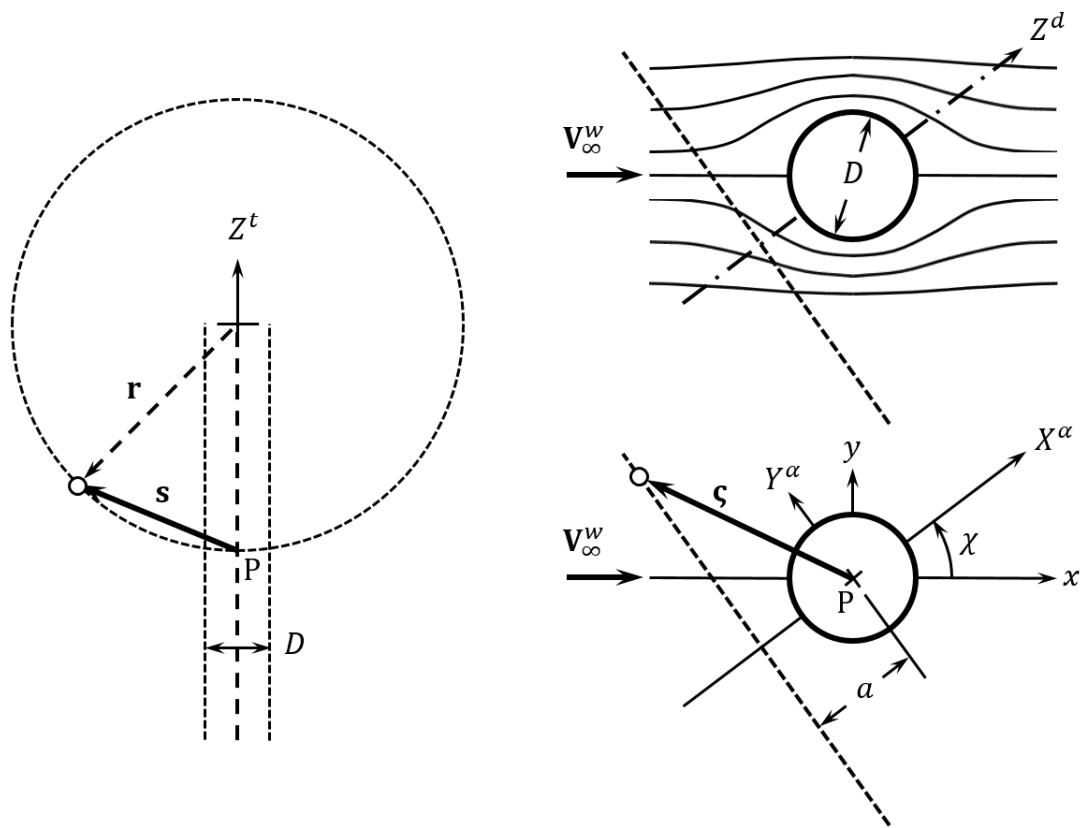
PROJECT
TotalControl

REPORT NUMBER
2020:00257

VERSION
1.0

27 of 78

Figure 5: Geometry for the computation of wind shear and tower shadow.

PROJECT
TotalControl

REPORT NUMBER
2020:00257

VERSION
1.0

28 of 78

where ψ_0 is the rotor azimuth that places the element in-line with point P. The rotor azimuth ψ is the only quantity in (138) that varies dynamically.

In order to link the vector $\mathbf{s}^g$ with x and y in (134), we define a special "analysis" coordinate system, denoted by α. This is a two-dimensional space, in the plane of the flow at Point P (Fig. 5). Define

$$\boldsymbol{\varsigma} = \begin{bmatrix} x^\alpha \\ y^\alpha \end{bmatrix} = \begin{bmatrix} -a \\ \sqrt{|\mathbf{s}|^2 - a^2} \end{bmatrix}. \tag{139}$$

Then,

$$\begin{bmatrix} x \\ y \end{bmatrix} = \mathbf{T}_\alpha^w(\chi)\,\boldsymbol{\varsigma}. \tag{140}$$

In words, we map the length of the vector $\mathbf{s}$ to a vector $\boldsymbol{\varsigma}$ in the two-dimensional potential-flow analysis plane. The offset in the y^α direction is the difference in length between $\mathbf{s}$ and its minimum value, the offset a. The y^α coordinate attains a maximum value of twice the blade-element radius when the element is oriented straight up, at which point it loops around from the opposite side of the analytical domain.

Once the velocity perturbations due to tower shadow are obtained in wind coordinates, they can be transformed to global coordinates,

$$\mathbf{v}_t^g = \mathbf{T}_w^g\,\mathbf{v}_t^w. \tag{141}$$

The wind coordinate system is defined according to the incoming wind field at Point P.

The above assumptions are reasonable when the radial coordinate of the blade element is much smaller than the tower radius. Some inaccuracy is to be expected near the blade root, where the blade element radius is on the same order as the tower diameter, and the presence of the nacelle disturbs the flow. In any case, it is the loading on the outer portion of the blades that is of concern; and here it is expected that the approximations are valid.

Wind shear is implemented by defining the mean wind vector $\mathbf{V}_\infty^g$ as a function of elevation z^g. Unless stated otherwise, for the analyses in this report a logarithmic profile

$$\mathbf{V}_\infty^g = \mathbf{V}_{\mathrm{ref}}^g \frac{\ln(z^g/h_0)}{\ln(z_{\mathrm{ref}}^g/h_0)} \tag{142}$$

has been used, with $h_0 = 0.01$ m. It is also possible to implement veer (a change in wind direction with height) but this is not considered at present. The global position of the blade element, to an accuracy sufficient for generating the wind spectra, is approximately

$$\mathbf{x}_{e/g}^g = \mathbf{O}_{d/g}^g + \mathbf{T}_d^g(\psi)\,\mathbf{r}^d. \tag{143}$$

The wind shear and tower shadow velocity fluctuations are correlated with each other, but they are assumed to be uncorrelated with the turbulence. This means that the covariance functions and spectra for wind shear and tower shadow should be computed together; but they can then be superposed with the corresponding turbulent quantities.

Figures 6 and 7 illustrate the wind velocity profiles seen by a rotating blade element, for respectively aligned and yawed flow conditions. Yawing rotates the tower shadow and wind shear profiles relative to the blade path, such that the deep flow-direction velocity deficit appears in both the axial and transverse components of wind speed, relative to the rotor.

Figure 8 shows some examples of the covariance functions of rotationally-sampled turbulence under ideal operating conditions, when the wind is aligned with the rotor, with the exception of a small rotor tilt angle. Looking at the single-point autocovariance, whose curve is shown in every plot, there is a slow decay in coherence with a period of about 100 s – the enveloping curve connecting the peaks – that represents the length scale of the turbulence being convected past the rotor. On top of this is an oscillatory signal associated with the rotor rotation: the coherence drops when the blade is oriented

PROJECT
TotalControl

REPORT NUMBER
2020:00257

VERSION
1.0

29 of 78
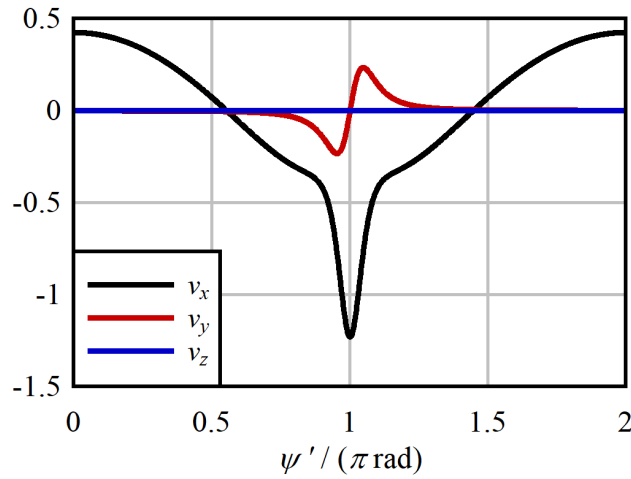
Figure 6: *The perturbation in the wind velocity due to shear and tower shadow. Units are m/s, and the average wind speed is 10 m/s in the X^g direction. For purposes of this plot, the ψ' angle is zero when the blade is straight up. (In the standard rotor coordinate system, $\psi = 0$ is horizontal.)*

Figure 7: *The perturbation in the wind velocity, in coordinates aligned with the rotor, due to shear and tower shadow, as a function of the wind angle (or yaw misalignment).*

Figure 8: Examples of turbulence covariance functions. Upper left: covariance of the $(\mathbf{v}^g)_x$ component (almost parallel with the axis of rotor rotation, except for the tilt angle) between two elements on the same blade. Upper right: autocovariance of the three velocity components at the same element. Lower left: covariance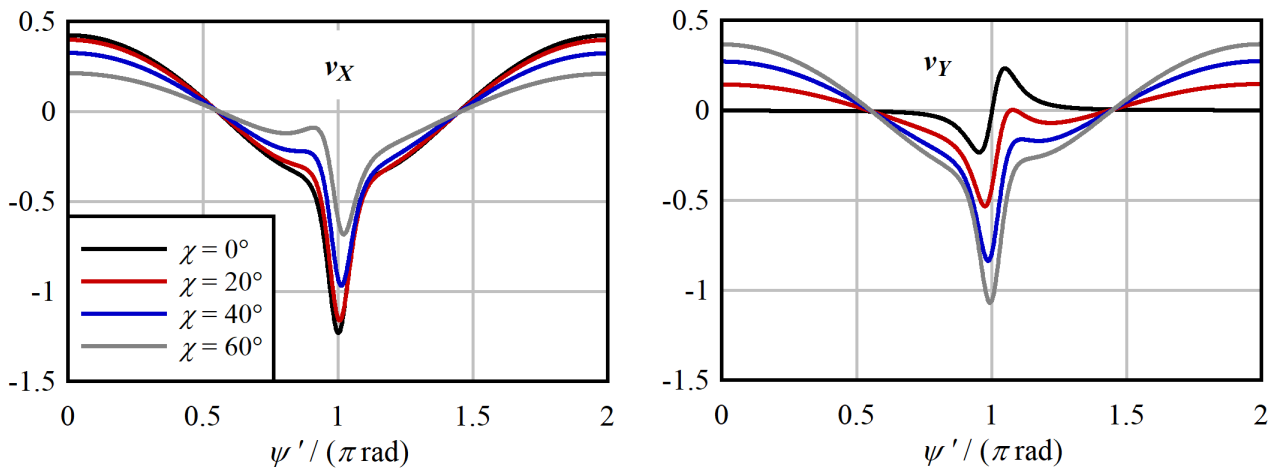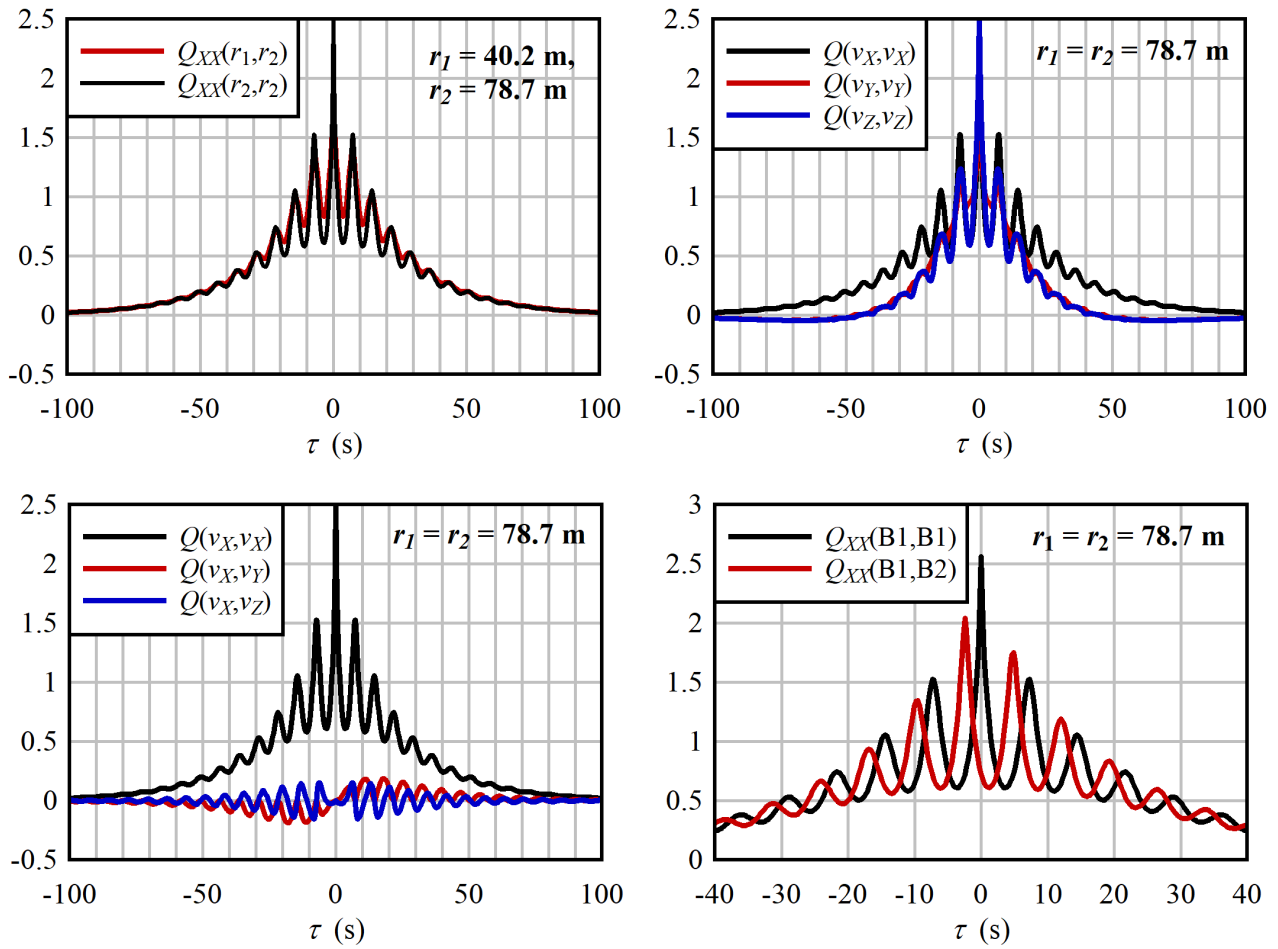 between the $(\mathbf{v}^g)_x$ component of velocity and the three components of $\mathbf{v}^g$ (the x component being the autocovariance) at the same element. Lower right: covariance of the $(\mathbf{v}^g)_x$ component between two blades, compared with the autocovariance; the time axis is magnified in order to emphasize the phase offset. Results were obtained using the following input parameters: $V_\infty = 10$ m/s, $I = 0.16$, $L_u = 180$ m, and $\Omega = 0.867$ rad/s.

at the opposite side of the rotor, and increases as the blade returns to its original azimuth. The plot at lower right shows the covariance obtained between different blades, where the phase offset of one-third the rotational period is evident. At lower left there are two curves showing the covariance of orthogonal components; these are uncorrelated if measured at a single point $\tau = 0$ but, due ultimately to the conservation of mass (Davidson 2004), they are weakly correlated over some distance.

The autocovariance of the $(\mathbf{v}^g)_x$ component of velocity is shown at the left of Fig. 9, and its Fourier transform, the spectrum, at right. The case of aligned flow is compared against that where the flow direction is misaligned by 40° in yaw. In these plots, which include only turbulence, not periodic effects like wind shear and tower shadow, yaw misalignment has a minor influence on the spectrum.[13]

The turbulence covariance functions (129) and (130) can be transformed into multi-blade coordin-

---

[13]As the spectra of wind shear and tower shadow occur as spikes of fixed area (discrete delta functions) at multiples of the rotational frequency, the height of the spikes depends on the discretization of the frequency, that is, the step size Δf. It therefore isn't so useful to plot their contribution alongside the stochastic turbulence spectrum, because the heights cannot be directly compared.
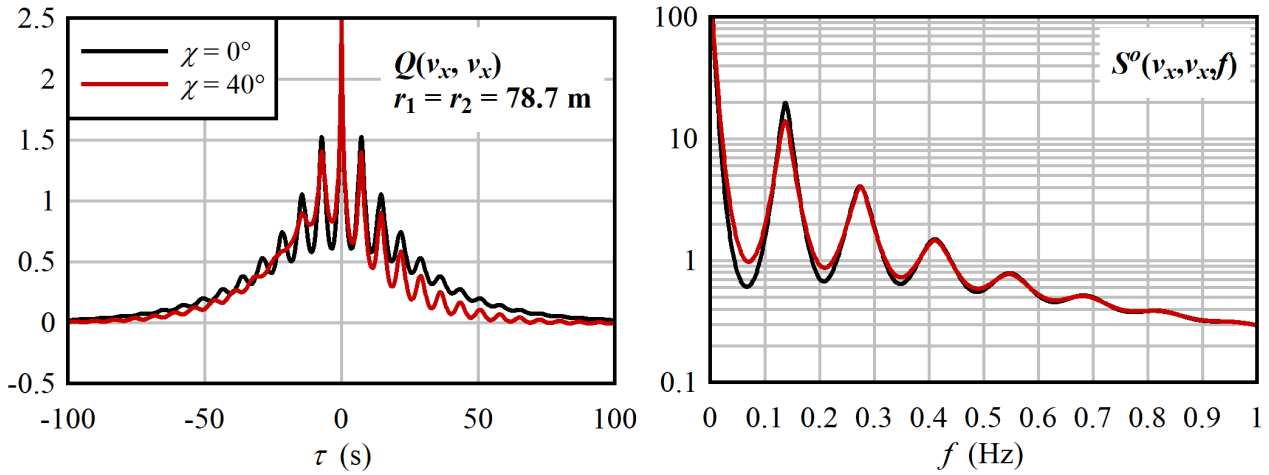
PROJECT
TotalControl

REPORT NUMBER
2020:00257

VERSION
1.0

31 of 78

Figure 9: The covariance (at left) and associated spectra (at right) of the axial component of wind speed under aligned and yawed flow conditions.

ates; or, more precisely, the covariance can be computed for the multi-blade-coordinate transformed velocity, as

$$\mathbf{Q}_{jk}^{\psi} = E\left[\mathbf{T}_B^{\psi}(0)\,\mathbf{v}_{j,b}(0)\,\mathbf{v}_{k,b}^T(\tau)\,\mathbf{T}_B^{\psi T}(\tau)\right] \tag{144}$$

where $\mathbf{v}_b$ is some triplet of velocity components, one for each blade. Illustrative results are shown in Fig. 10. The transformation reduces the covariance – not surprisingly, because the multi-blade coordinate transform in effect averages over the three blades, which are located some distance apart – and redistributes the remaining rotationally-sampled energy to multiples of the *blade passing* frequency, as opposed to the rotor's rotational frequency.

In closing, a note on what is missing from the multi-blade-coordinate transformed wind spectra, as derived in this section and implemented in STAS Wind. The methods include the effects of stochastic turbulence and the asymmetry of wind shear and tower shadow, although these have been simplified by neglecting wake (induction) effects. In addition, implicit in (129) and (130) is the assumption that the turbulence is isotropic. There is no reason that these particular equations must be used; we have adopted them because they provide an analytic description of the correlation functions, which can then be evaluated to high numerical precision.[14] The multi-blade coordinate transform eliminates the first harmonic – that is to say, linear trends in the flow field across the rotor in the fixed frame – from the equations of motion. The way in which wind shear and tower shadow were implemented account for higher harmonics. However, under yawed flow conditions there are also higher harmonics associated with nonlinearities in the aerodynamic forces on the blades, interacting with the misaligned flow field. These higher harmonics are neglected, being accounted for neither in the turbulence spectra, nor in the linearized aeroelastic equations. Floquet theory (Johnson 1994) can be used to generate linear time-invariant dynamic equations for higher harmonics.

2.2 Transfer functions and performance metrics

Aside from basic stability considerations, which can be determined by looking at the damping ratios

$$\zeta_k = \sqrt{\frac{R^2}{1+R^2}}, \qquad R = \frac{\Re\{\lambda_k\}}{\Im\{\lambda_k\}} \tag{145}$$

---

[14]If a more realistic atmospheric turbulence model is desired, then the rotationally-sampled cross-spectra may be generated numerically, by following the path (131) through a number of Monte-Carlo realizations of the turbulence field. It is also possible that other analytical formulations with greater generality exist in the literature.

PROJECT
TotalControl

REPORT NUMBER
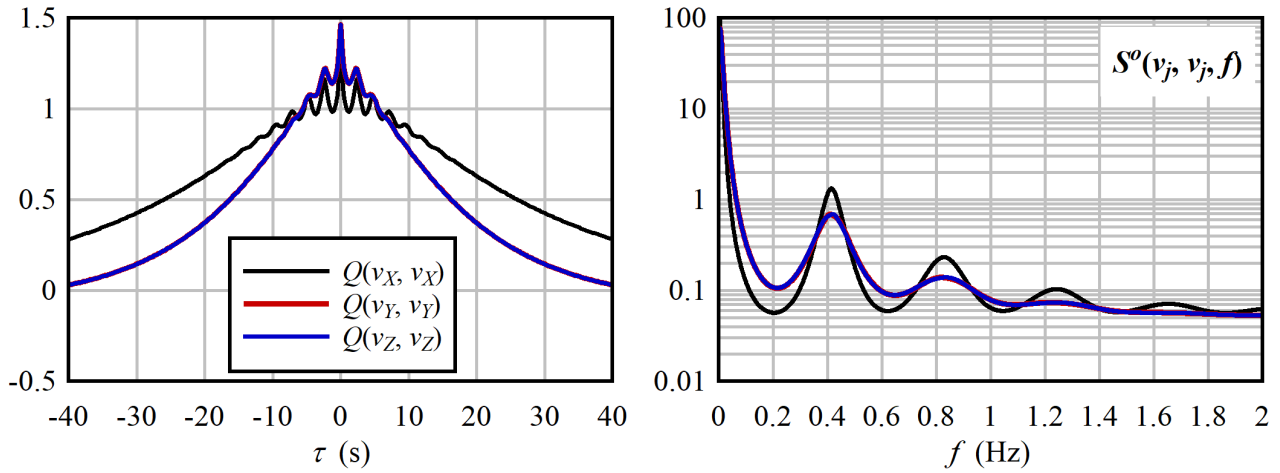2020:00257

VERSION
1.0

32 of 78

Figure 10: At left: the multi-blade-coordinate transformation of the covariance curves in the lower left plot of Fig. 8. At right: the associated spectra.

Table I: Key quantities of interest for load control of an offshore wind turbine foundation.

Disturbances		Controls		Load metrics		Other metrics	
$\mathbf{F}_w^g$	Wave loads	$\widehat{P}_e$	Generator power	$\boldsymbol{\delta}_{n/g}^g$	Nacelle displacements	Ω	Rotor speed
$\mathbf{V}_R^r$	Rotor-avg. wind	$\widehat{\boldsymbol{\beta}}$	Blade pitch	$\mathbf{M}_f^F$	Mud-line moments	P_e	Elec. power
		$\widehat{\chi}$	Nacelle yaw	$\boldsymbol{\delta}_b^p$	Blade tip deflections		
				$\mathbf{M}_b^p$	Blade root moments		

of the eigenvalues, we desire some metrics of performance for the active load control functions. Table I summarizes the key inputs (disturbances) and outputs (control actions and load metrics). The ideal controller would prevent the disturbances from influencing the loads – that is, the disturbance-to-load transfer function should be small – while using minimal control actions: the disturbance-to-control transfer function should also be small. Of course, these objectives are conflicting, and a well-designed controller must strike a compromise between control activity and effectivity.

Also of interest are the sensors available to the control system. Table II lists a selection of standard sensors.

The transfer functions between the assorted combinations of disturbances, sensors, controls, and metrics have the interpretations listed in Table III. Various aspects of system behavior and perform- ance can be visualized and explained by looking at the transfer functions, and relating the features seen in the transfer functions to the modes of the system.

Table II: Key sensors available to the control system.

	Sensors:
$\overline{\Omega}$	Rotor speed
$\overline{\boldsymbol{\beta}}$	Blade pitch $(\beta_1, \beta_2, \beta_3)$
$\overline{\chi}$	Nacelle yaw
$\overline{P}_e$	Electric power
$\overline{\mathbf{a}}^n$	Nacelle acceleration
$\overline{V}_a$	Anemometer wind speed
$\overline{\theta}_a$	Anemometer wind direction

PROJECT
TotalControl

REPORT NUMBER
2020:00257

VERSION
1.0

33 of 78

Table III: Meaning of different types of closed-loop transfer functions.

Disturbance→Control	How active are the controls?
Disturbance→Metric	How effective is the controller?
Disturbance→Sensor	Can disturbances be measured?
Control→Metric	Are the objectives influenced by the controls?
Metric→Control[(a)]	Does the controller respond to deviations in performance?
Metric→Sensor[(a)]	Can the performance be measured?
Sensor→Control	Controller's internal dynamics and response.
Sensor→Metric	How important are various sensors?
(a) Relevant if the loop is closed with output feedback.	

2.3 Normal operation

Consider an offshore wind turbine operating normally in a typical wind climate. Turbulence in the wind, and ocean waves, introduce fluctuating loads that excite structural motions. We are interested to know what modes are excited, and how these each contribute to the internal loads in the support structure.

2.3.1 Control functions

Table IV summarizes the control functions that are active during normal operation. Rotor speed control and nacelle yaw are the most basic and essential control functions, required for the wind turbine to operate and generate power. A typical architecture for the rotor speed control function has separate blade pitch and generator power control loops, each of which saturates when the other becomes active. Large commercial wind turbines have also a suite of control functions that reduce the severity of certain load effects, such as tower vibration and wind shear. To save wear on the actuators, these load-control functions may be activated or deactivated according to some threshold criteria. A supervisory level of control handles such decisions, as well as safety functions, start-up, and shut-down.

A control system design that implements the control functions in Table IV is described by Merz and Pedersen (2018), with an updated rotor speed control function (Merz *et al.* 2019) applied in the present work.

2.3.2 Aligned wind and waves

First we look at the baseline case where the rotor is properly aligned with the incoming wind, and the ocean waves approach from the same direction as the wind. In this case the fluctuating loads are primarily in the fore-aft direction. Inputs are considered to be the $(\mathbf{v}^g)_x$ component of the rotor-average wind, and the $(\mathbf{F}^g)_x$ component of the nodal force at the waterline.

Figure 11 shows the transfer functions from these inputs to the fore-aft and side-to-side mudline bending moments, when the mean wind speed is 10 m/s. A change in the steady (zero-frequency) wind speed results in a change in the steady fore-aft bending moment (a), due to the aerodynamic thrust on the rotor; but also the side-to-side bending moment (b), due to the change in the generator torque. Contrast this with the effect of waterline forces (right-hand plots), where a perturbation in the mean current load does not at all influence the side-to-side bending. The first resonant modes of the tower (c) form the dominant features in the plots. The first fore-aft and side-to-side modes have approximately the same natural frequency, near 0.24 Hz; with the present controller, both of these are actively damped, the fore-aft mode by blade pitch and the side-to-side mode by generator torque. The second tower resonant modes at (d) are also present, but the response is less sensitive to wind fluctuations than at the frequency of the first modes; in addition, wind and wave disturbances at the second resonant frequency are expected to be small. Two particular frequencies are therefore singled

PROJECT
TotalControl

REPORT NUMBER
2020:00257

VERSION
1.0

34 of 78

Table IV: Standard wind turbine control functions.

Function	Objective	Inputs	Outputs
Rotor speed control	Maintain target rotor speed	$\overline{\Omega}, V_\infty^*, \hat{P}_o$	$\hat{\beta}_0, \hat{P}_e$
Blade pitch	(a)	$\overline{\Omega} - \hat{\Omega}$	$\hat{\beta}_0$
Generator power	(b)	$\overline{\Omega}, \hat{P}_o$	$\hat{P}_e$
Nacelle yaw	Keep rotor oriented with wind	$\overline{\theta}_a$	$\hat{\chi}$
Virtual induction generator	Damp driveshaft torsion	$\overline{\Omega}$	$\hat{P}_e$
Tower fore-aft damping	Damp first resonant mode	$(\overline{\mathbf{a}}_n)_x$	$\hat{\beta}_0$
Tower side-to-side damping	Damp first resonant mode	$(\overline{\mathbf{a}}_n)_y$	(c)
Wind shear compensation	Reduce cyclic blade loads	(d)	$\hat{\beta}_s$

(a) Above V_r: pitch to control rotor speed. Below V_r: saturate at zero.

(b) Above V_r: saturate at rated power. Below V_r: track maximum power point.

(c) Either generator torque (via $\hat{P}_e$) or rotor IBP sine component $\hat{\beta}_s$ may be used.

(d) An estimate of asymmetric blade or nacelle loads (deflections): $\overline{\mathbf{a}}^n$ or strain.

$\overline{\mathbf{a}}^n$: measured nacelle acceleration.

$\hat{P}_e$: electric power command.

$\hat{P}_o$: operator power command.

V_r: wind speed at rated or commanded power.

V_∞^*: wind speed, estimated by a state observer.

$\hat{\beta}_0$: collective blade pitch command.

$\hat{\beta}_c$: cosine blade pitch command.

$\hat{\beta}_s$: sine blade pitch command.

$\overline{\theta}_a$: nacelle anemometer wind direction.

$\hat{\chi}$: measured nacelle yaw angle.

$\overline{\Omega}$: measured rotor speed.

$\hat{\Omega}$: Target rotor speed.

PROJECT
TotalControl

REPORT NUMBER
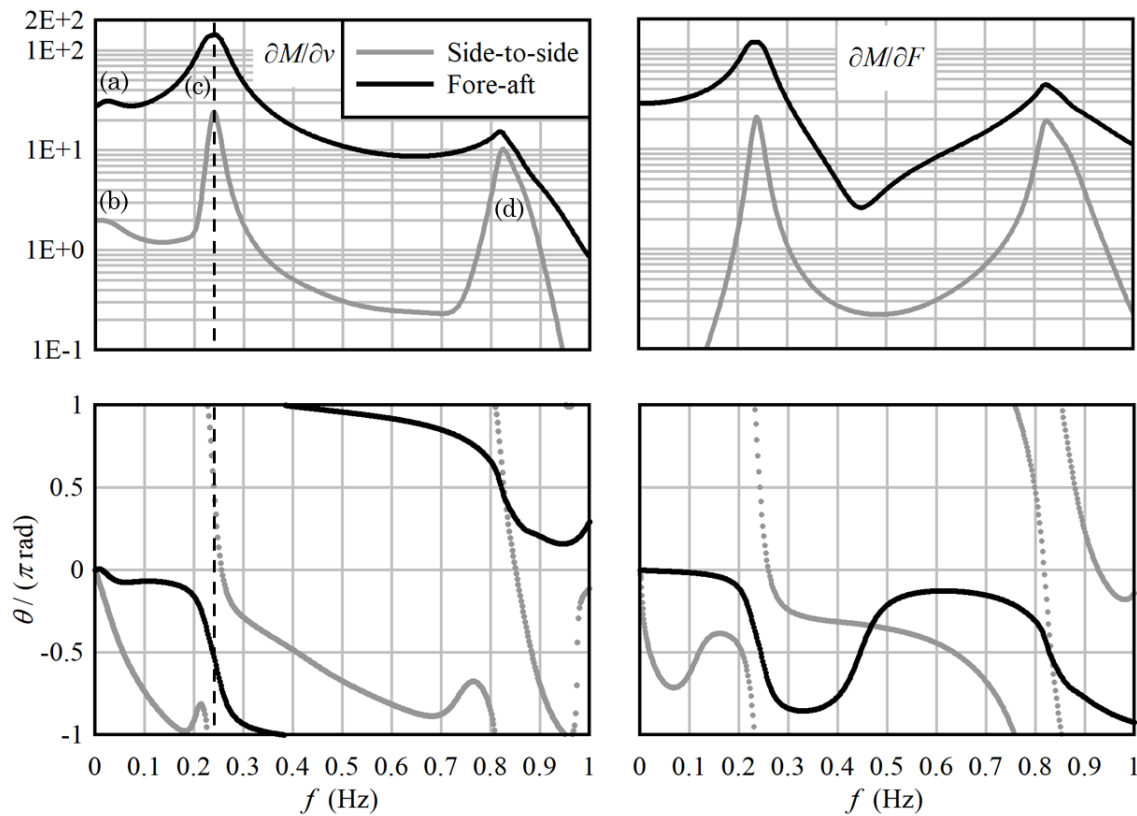2020:00257

VERSION
1.0

35 of 78

Figure 11: Normal operation, $V_\infty = 10$ m/s. Transfer functions from rotor-average wind speed (at left) and waterline wave force (at right) to mudline bending moment. Transfer function units are, for $\partial M/\partial v$, MN·s, and for $\partial M/\partial F$, m.

out for further investigation: the steady state response (a) and (b) near zero frequency, and the first resonant frequency (c).

We focus the present discussion on the resonant response (c). Table V lists the modes that contribute significantly to the value of the transfer function at the resonant frequency. Recall that $\mathcal{P}$, from (17), is the normalized projection of an individual modal transfer function in the direction (phase) of the total transfer function – the total, equal by definition to 1, being the sum of all the modal projections. The modes in Table V were chosen by ranking the projections in decreasing order of magnitude, and truncating the series when the cumulative sum approached unity. There are 386 modes in the present model, yet only two to four contribute meaningfully to the tower loads at the first tower resonant frequency – a considerable simplification!

The fore-aft motion of the tower is governed by two oscillatory modes: one mode associated with the mass of the rotor nacelle assembly, oscillating against the tower which acts as an elastic spring; and another mode associated with the band-pass filter in the active damping control loop. The characteristics of these modes are summarized in Table VI. For each mode, the amplitude and phase angle associated with relevant metrics, control actions, and sensor measurements are listed.

If the active damping control gain were set to zero, the two modes would be independent: the tower mode would contain the tower motions, and the active damping control mode would contain the band-pass filter, with no overlap. As it is, with the active damping control engaged, the modes are mixed: what we call the "first tower" mode contains contributions from both the tower and controller, and likewise for the active damping control mode; which mode is given which name, is a question of degree.

Now let us see how the two fore-aft modes combine to produce the tower resonant response. Figure

PROJECT
TotalControl

REPORT NUMBER
2020:00257

VERSION
1.0

36 of 78

Table V: Normal operation, $V_\infty = 10$ m/s. A list of the modes that contribute to the wind-speed-to-mudline-moment transfer functions at the first tower resonant frequency. The frequency f_1 is 0.238 Hz, approximately the natural frequency of the tower fore-aft and side-to-side modes when there is no active damping.

			Fore-aft moment
f_n	ζ	$\mathcal{P}(f_1)$	Description
0.250	0.085	0.63	First tower fore-aft
0.229	0.095	0.41	Tower fore-aft active damping control
			Side-to-side moment
f_n	ζ	$\mathcal{P}(f_1)$	Description
0.245	0.037	1.51	First tower side-to-side
0.250	0.085	-0.23	First tower fore-aft
0.229	0.095	-0.21	Tower fore-aft active damping control
0.237	0.079	-0.08	Tower side-to-side active damping control

Table VI: Normal operation, $V_\infty = 10$ m/s. Amplitudes and phase angles of selected response variables, for each of the modes that contribute to the wind-speed-to-mudline-moment transfer functions at the first tower resonant frequency. Amplitudes are in the given units, and phase angles $-\pi < \theta \le \pi$ are normalized by π, that is, -1 is a phase angle of $-\pi$ and $+1$ is a phase angle of π. Note that these are quantities derived from the mode shapes, not the transfer functions with respect to an external input like Fig. 11.

		1st fore-aft		FA damping		1st side-to-side		SS damping	
f_n	(Hz)	0.250		0.229		0.245		0.237	
ζ	(-)	0.085		0.095		0.037		0.079	
$(\boldsymbol{\delta}^g_{n/g})_x$	(m)	1.000	0.000	1.000	0.000	0.286	0.561	0.363	0.764
$(\boldsymbol{\delta}^g_{n/g})_y$	(m)	0.067	0.840	0.072	-0.725	1.000	0.000	1.000	0.000
$(\mathbf{M}^F_F)_x$	(MNm)	25.12	-0.151	22.84	0.291	356.2	-0.990	344.9	-0.978
$(\mathbf{M}^F_F)_y$	(MNm)	353.1	0.007	348.8	0.007	101.1	0.565	127.4	0.770
$(\boldsymbol{\delta}^g_\emptyset)_x$	(m)	0.975	-0.080	1.335	-0.058	0.327	0.596	0.480	0.789
$(\boldsymbol{\delta}^g_c)_x$	(m)	0.067	-0.692	0.056	-0.664	0.176	-0.050	0.151	0.160
$(\boldsymbol{\delta}^g_s)_x$	(m)	1.012	-0.062	1.014	-0.056	0.271	0.492	0.353	0.711
$(\mathbf{M}^p_b)_y$	(MNm)	3.825	0.474	5.906	0.792	0.605	-0.434	1.738	-0.316
$(\mathbf{M}^p_b)_z$	(MNm)	0.648	0.907	1.224	0.147	3.690	0.408	8.596	0.609
T_g	(MNm)	1.885	0.937	3.784	0.162	13.90	0.417	32.05	0.620
$\beta_\emptyset$	(deg)	1.070	0.082	2.222	0.928	0.202	0.898	1.270	-0.709
Ω	(rad/s)	0.024	0.999	0.031	0.991	0.065	0.868	0.135	-0.903
$\overline{\Omega}$	(rad/s)	0.021	0.814	0.028	0.817	0.057	0.690	0.121	0.920
$\overline{\beta}_\emptyset$	(deg)	0.991	-0.071	2.096	0.786	0.184	0.751	1.184	-0.855
$\overline{P}_e$	(MW)	1.702	0.882	2.799	0.119	11.06	0.370	25.60	0.574
$(\overline{\mathbf{v}}_n)_x$	(m/s)	1.580	0.527	1.444	0.530	0.441	-0.927	0.543	-0.710
$(\overline{\mathbf{v}}_n)_y$	(m/s)	0.106	-0.632	0.104	-0.194	1.539	0.512	1.493	0.525

f_n: natural frequency.

ζ: damping ratio.

$\boldsymbol{\delta}^g_{n/g}$: nacelle displacement in the global coordinate frame.

$\mathbf{M}^F_F$: foundation mudline internal bending moments in the foundation coordinate frame.

$\boldsymbol{\delta}^g_{\emptyset,c,s}$: blade tip deflection in the MBC frame; collective, cos, sin components.

$\mathbf{M}^p_b$: blade root internal bending moments in the pitch coordinate frame.

T_g: generator torque.

β_0: blade collective pitch.

Ω: rotor speed.

$\overline{\Omega}$: measured rotor speed.

$\overline{\beta}_0$: measured blade pitch.

$\overline{P}_e$: measured electrical power.

$\overline{\mathbf{v}}^n$: measured nacelle velocity.

PROJECT
TotalControl

REPORT NUMBER
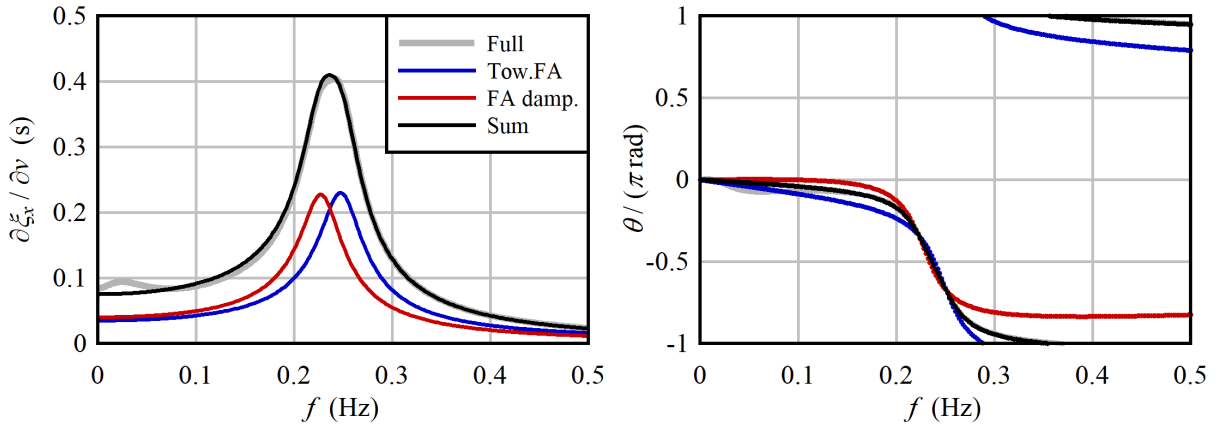2020:00257

VERSION
1.0

37 of 78

Figure 12: Normal operation, $V_\infty = 10$ m/s. The contribution of the 1st tower fore-aft mode and active fore-aft damping mode to the total transfer function of nacelle fore-aft displacement.
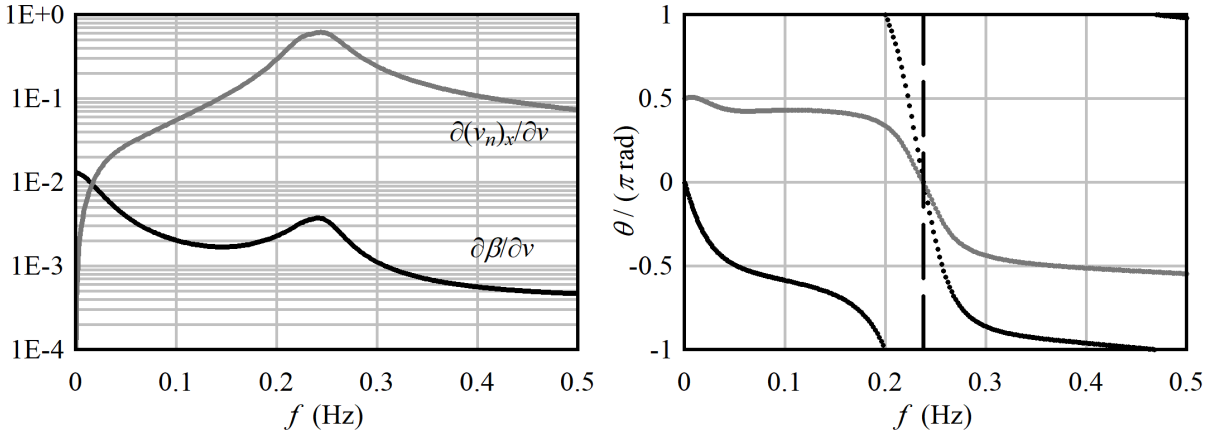

Figure 13: Normal operation, $V_\infty = 10$ m/s. The wind speed to blade pitch and nacelle fore-aft velocity transfer functions, showing in particular the behavior of the relative phase in the vicinity of the tower's natural resonant frequency (dashed line).

12 shows the individual $\partial\zeta_x/\partial v$ (wind speed to tower fore-aft displacement) transfer functions, their sum, and the full transfer function. Consistent with the values in Table V, the transfer function in the vicinity of resonance is dominated by the two modes – also well away from the resonant frequency, between 0.1 and 0.5 Hz.

Referring to the modal properties in Table VI, the reader may notice that the pitch angle β_0 and the nacelle fore-aft velocity $(\mathbf{v}_n)_x$ are not in-phase for either of the fore-aft modes. It is expected that β_0 and $(\mathbf{v}_n)_x$ should be in-phase in order to provide effective damping. In fact, they *are* in-phase at the nominal resonant frequency of the tower; this can be seen in Fig. 13, which compares the transfer functions from the wind speed disturbance to the blade pitch and nacelle velocity. The characteristics of the two resonant modes – the way in which their natural frequencies split away to each side of the nominal tower frequency of ca. 0.24 Hz, with a moderate increase in the damping ratio – result from an interaction of the bandpass filter in the active damping function, the notch filter on the rotor speed control function, and the natural tower resonance.

The side-to-side modes, in contrast with the fore-aft modes, have a straightforward behavior. The frequencies of the tower and active damping modes remain aligned, and the generator torque is in-

PROJECT
TotalControl

REPORT NUMBER
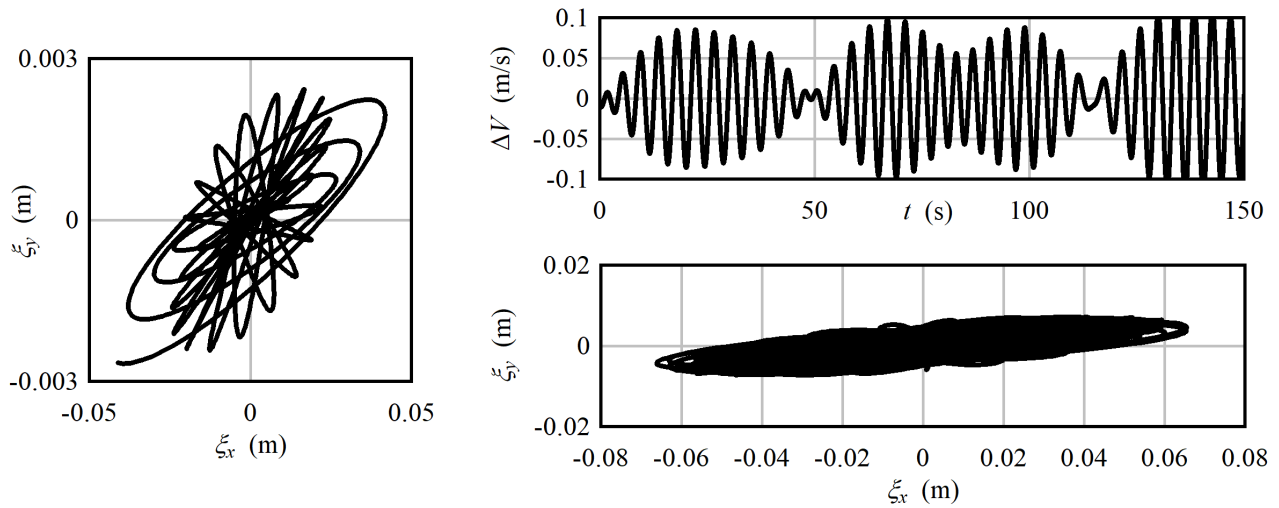2020:00257

VERSION
1.0

38 of 78

Figure 14: Normal operation, $V_\infty = 10$ m/s. A precessing pattern of nacelle displacement is experienced when exciting resonance with a narrow-band stochastic signal near the resonant frequency. Upper right: a sample of the wind speed input. At left: a close-up of the pattern, with different scaling applied to the x and y axes. Lower right: a long-term trace of the nacelle displacement with uniform scaling of the x and y axes.

phase with the velocity at the resonant frequency, as one would expect. This straightforward behavior, in contrast with the fore-aft mode, likely results from the responsiveness of the electric system.

The transfer functions in Fig. 11 indicate that the difference in phase between the fore-aft and side-to-side moments changes abruptly in the vicinity of the resonant frequency. Just below the resonant frequency, the fore-aft response leads the side-to-side by $\pi/2$, this changing to lagging by $\pi/2$ just above the resonant frequency. This pattern indicates a precessional motion, an example of which is illustrated in Fig. 14. Here an artificial wind speed input signal is introduced,[15] consisting of a large number of sinusoids with random phases, and frequencies between 0.22 and 0.26 Hz. As the frequency content of the input signal varies within this range, the phase between the fore-aft and side-to-side motion changes, giving patterns as seen in the plot at left. The amplitude of the fore-aft motion is an order of magnitude greater than that of the side-to-side motion, which is evident when the axes are scaled uniformly, as in the plot at lower right.[16] It is concluded that although the nacelle traces a precessing orbit, the magnitude in the side-to-side direction is small, and the dominant motion, and loading of the foundation, will occur in the fore-aft direction.

Tables VII and VIII list respectively the first-harmonic and dissipative powers passing through the aerodynamic forces and generator air gap, when the turbine is oscillating freely in each mode. Evidently, the use of the generator to damp tower side-to-side motion is quite ineffective, in the sense that the power fluctuations in the grid are much larger than the rate of dissipation of energy from the structure into the grid. This is a consequence of the fact that the angular speed of the rotor is much larger than that of the tower motion that the generator is attempting to damp: the $\Omega_0 \Delta T_g$ term is responsible for the majority of the power oscillations.

In summary: although this section is still far from having provided a complete picture of the turbine dynamics, we have gone into quite some detail on the modes that contribute to the tower mudline bending moment, in the vicinity of the first tower resonant frequency, under normal operation. Each mode was described in terms of its natural frequency and damping ratio; and three sets of response variables, representing key metrics of structural loading, control actions, and sensor measurements.

---

[15]The input is artificial in the sense of omitting the low frequencies. But the signal is indeed sufficient to excite the resonant dynamics across the desired frequency band.

[16]These results are comparable with those of Hansen *et al.* (2006).

PROJECT
TotalControl

REPORT NUMBER
2020:00257

VERSION
1.0

39 of 78

Table VII: Normal operation, $V_\infty = 10$ m/s. First-harmonic oscillatory power in MW per unit modal displacement of the mode shapes from Table VI.

	1st fore-aft		FA damping		1st side-to-side		SS damping	
Aerodynamic	1.895	0.480	2.111	0.495	0.665	−0.855	0.976	−0.686
Generator	4.598	−0.511	5.897	−0.433	11.83	−0.540	26.41	−0.334

Table VIII: Normal operation, $V_\infty = 10$ m/s. Dissipative power in MW per unit modal displacement of the mode shapes from Table VI.

	1st fore-aft	FA damping	1st side-to-side	SS damping
Aerodynamic	−1.234	−1.205	−0.092	−0.394
Generator	0.008	−0.098	−0.504	−1.753

We have looked at how power is transferred across important system boundaries – aerodynamic forces, the electric grid, and seabed – with a particular focus on the dissipation of oscillations. With this understanding of the basic modes and transfer functions, we are in a position to develop alternate control strategies in Sections 4 and 5.

2.3.3 Misaligned waves

When the ocean waves approach from a direction that is misaligned with respect to the prevailing wind, there is a greater component of excitation in the side-to-side direction. The waves can be considered as purely alternating, so the mode shapes from Section 2.3.2, obtained at the steady-state operating point, are unchanged. It is the $\boldsymbol{\psi b}$ terms from (15) that change.

To put things in the proper perspective, we need to introduce the wind and wave spectra to the analysis, which gives us quantitative, stochastic estimates of the tower motions and internal bending moments. This introduces a considerable complication, as particular combinations of wind and wave climates need to be specified.

Data for the North Sea area, hindcast over a period of 50 years in three-hour increments, are available from the Norwegian Meteorological Institute (Reistad *et al.* 2009). A location in the vicinity of the Dogger Bank was extracted in order to provide a basis for analysis. Table IX lists the bins used for categorizing the combined wind and wave states. Here the θ^E coordinate system, which is convenient to use as a global coordinate system for the analyses, has its X^E axis pointing East, the Z^E axis pointing skywards, and a positive angle counterclockwise, in the standard right-handed convention. Angles are measured from $-\pi$ to π ($-180°$ to $180°$). Note that this is different from the compass coordinate system, which has its X^c axis pointing North, clockwise as a positive angle, and a range of angles from $0°$ to $360°$.

The binning is done according to a linear weighting. For instance, a wind speed of 11 m/s would be counted as 0.75 of an occurrence in the 10 m/s bin, and 0.25 in the 14 m/s bin. This procedure diffuses and smooths the probability distribution throughout the bin-space. It has the advantage of

Table IX: Bin centers and widths (increments) used for categorizing the environmental conditions.

Value	Units	min	max	width
V_∞	m/s	2	22	4
θ_V^E	deg	-165	165	30
H_s	m	1	10	1
T_p	s	3	18	1
θ_w^E	deg	-165	165	30

PROJECT
TotalControl

REPORT NUMBER
2020:00257

VERSION
1.0

40 of 78

Table X: The ten most likely environmental conditions.

p	V_∞	θ_V^E	H_s	T_p	θ_w^E	θ_V^E - θ_w^E
0.00352	14	-135	2	6	-135	0
0.00343	10	-105	1	5	-105	0
0.00313	14	-105	2	6	-105	0
0.00273	14	-135	2	6	-105	-30
0.00272	10	-75	1	5	-75	0
0.00272	14	-165	2	6	165	30
0.00271	10	-135	1	5	-105	-30
0.00256	10	-105	1	4	-105	0
0.00249	10	-105	1	5	-75	-30
0.00244	10	-135	1	5	-135	0

avoiding the case where two nearly identical cases are assigned to different bins; to give an example, a wave direction of 119° assigned to the 105° bin and a direction of 121° assigned to the 135° bin.

When the data are sorted according to the most likely conditions, the top ten are listed in Table X. From this it can be stated that the most likely conditions are winds near the rated wind speed, combined with wind-driven waves aligned within ±30° of the wind direction. The wind-driven waves are of small amplitude but short period, where they will tend to excite tower resonance.

Large misalignments of wind and waves are common. The misalignment is 60° or more (bin-wise) 36% of the time; however such misalignment is rare during storm conditions. This is to be expected, since storm waves will tend to align with the wind and dominate swell from other directions. The breakdown of wave misalignment, with values representing bin centers, is:

- 22% of the time misalignment is $\geq 60°$ when the wind is 2 or 6 m/s.

- 10% of the time misalignment is $\geq 60°$ when the wind is 10 m/s.

- 4% of the time misalignment is $\geq 60°$ when the wind is ≥ 14 m/s.

Table XI lists the selected wind-wave conditions, for use in designing and evaluating load-reducing controls. The first eight cases cover normal operation below and above the rated wind speed, with relatively short-period waves approaching from different directions relative to the wind. Due to the short period it is expected that these waves will excite tower resonance and, without the help of special control functions, contribute a disproportionate amount of the accumulated fatigue. The cases below the line are rare, yet observed, conditions. The first case is a large swell, when there is no wind locally and the turbine will be idling; in the second case large, short-period waves approach at an angle; and in the third case short-period waves approach from a direction orthogonal to the wind.

During Cases 10-2-0, -30, -60, and -90 the auto-spectra of nacelle fore-aft and side-to-side displacement are as shown in Fig. 15. These spectra are, in essence, a combination of the transfer functions of Fig. 11 and the spectra of Fig. 10. There are four features of particular note, in the frequency band below 0.5 Hz. The low-frequency peak is the quasi-static response of the tower to atmospheric turbulence. The peak at (b) is associated with the response to ocean wave loads on the tower. The neighboring peak at (c) is the first tower resonant mode, excited primarily by the relatively short-period waves. The spike at (d), the 3P blade-passing frequency, is due to periodic loads on the rotor, namely wind shear and tower shadow, whereas the lower and more rounded hump at the same frequency is due to rotational sampling of turbulence.

There is less damping in the side-to-side than the fore-aft direction (Table V). As a consequence, the resonant response in the side-to-side direction to ocean waves is more severe than that in the fore-aft direction.[17] The resonant response is significant already at 30° misalignment.

---

[17] It would be even more severe, but the response is reduced by active damping control using the generator.

PROJECT
TotalControl

REPORT NUMBER
2020:00257

VERSION
1.0

41 of 78

Table XI: Selected wind-wave environmental conditions.

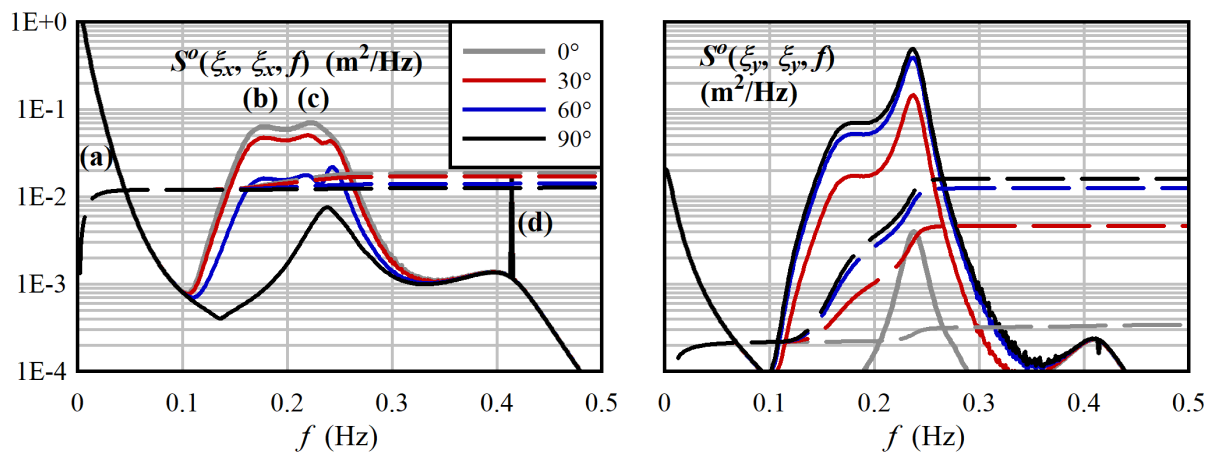| Case	p	V_∞ (m/s)	H_s (m)	T_p (s)	$\lvert\theta_V - \theta_w\rvert$
10-2-0	0.03260	10	2	6	0
10-2-30	0.01214	10	2	6	30
10-2-60	0.00312	10	2	6	60
10-2-90	0.00109	10	2	6	90
14-2-0	0.02199	14	2	6	0
14-2-30	0.01820	14	2	6	30
14-2-60	0.00211	14	2	6	60
14-2-90	0.00053	14	2	6	90
2-3-x	0.00010	2	3	12	(-)
14-4-30	0.00059	14	4	8	30
14-3-90	0.00014	14	3	6	90

Figure 15: Case 10-2-0: One-sided spectra of nacelle fore-aft (at left) and side-to-side (at right) displacement. The dashed lines are the integrals of the spectra; the cumulative integral of each spectral curve is the variance.

PROJECT
TotalControl

REPORT NUMBER
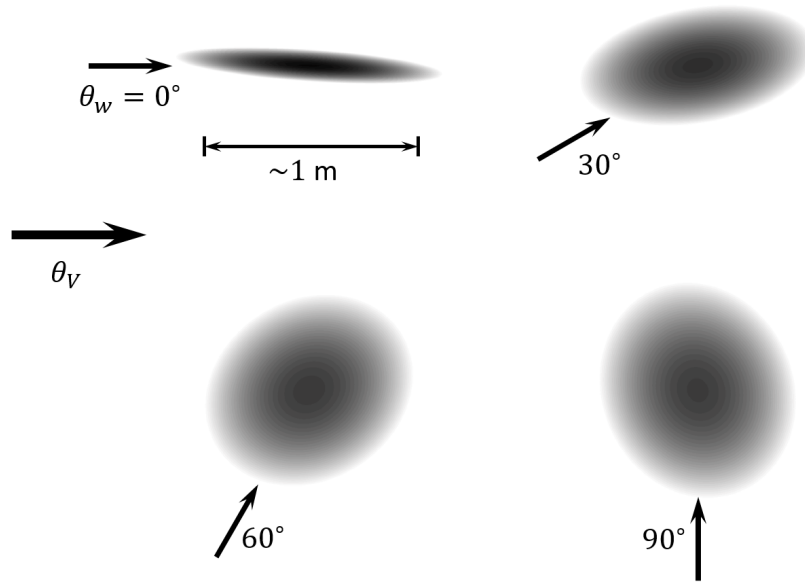2020:00257

VERSION
1.0

42 of 78

Figure 16: Cases 10-2-x: Joint probability density functions, shaded according to a logarithmic scale ($-2 \leq \log_{10} p \leq 2$), showing wind-direction and transverse nacelle displacements under different wave directions.

The joint probability density function, which we assume to be Gaussian, can be computed from the spectra in Fig. 15, together with the cross-spectra $S^o(\xi_x, \xi_y, f)$ and $S^o(\xi_y, \xi_x, f)$. The probability densities of nacelle displacement for various degrees of wave misalignment are plotted in Fig. 16. The shading is done on a logarithmic scale, proportional to $\log_{10} p$, such that the edge of the visible region is quite unlikely, roughly 10^{-4} the density of the center. In other words, the nacelle will rarely displace 0.5 m from its static position – though this is possible. What we see in the probabilities, as well as the spectra of Fig. 15 is encouraging: the degree of coupling between the fore-aft and side-to-side directions is small, although evident, and the trends follow what could be guessed about the solution using common sense.

3 Control design

Figure 17 shows the system architecture and terminology that we will use in designing the active load control functions. The plant consists of the open-loop wind turbine and sensor dynamics, as shown in the cascade at the right-hand side of the figure. The disturbances acting on the wind turbine are the wind and waves $\mathbf{w}$, and sensor noise $\mathbf{n}$. Control inputs $\mathbf{u}$ are a blade pitch command for each blade $\hat{\boldsymbol{\beta}}$, a commanded electrical power $\hat{P}_e$, and a yaw angle command $\hat{\chi}$. The wind turbine outputs raw measurement quantities $\mathbf{y}_T$, which are measured with some sensor dynamics, consisting of states $\mathbf{x}_s$. The filtered sensor outputs fed to the controller are $\overline{\mathbf{y}}_T$. The linearized model of the plant is reduced to the relevant modes, that contribute to the input-to-sensor and disturbance-to-sensor dynamics; this combines the turbine and sensor dynamics into a single set of equations, with modal states $\boldsymbol{\xi}$.

It is assumed that the sensor system reports the nacelle displacement, which has been integrated based on a measurement of the nacelle acceleration. Similarly, where relevant it is assumed that the velocity of nacelle motion is also known.

The controller consists of two modules, a state observer and a control law. The state observer consists of a (typically low-order) model of the plant, which may be augmented with states representing disturbances. The purpose is to estimate a selection of the states $\boldsymbol{\xi}$ and disturbances $\mathbf{w}$, for use in the control law.

PROJECT
TotalControl

REPORT NUMBER
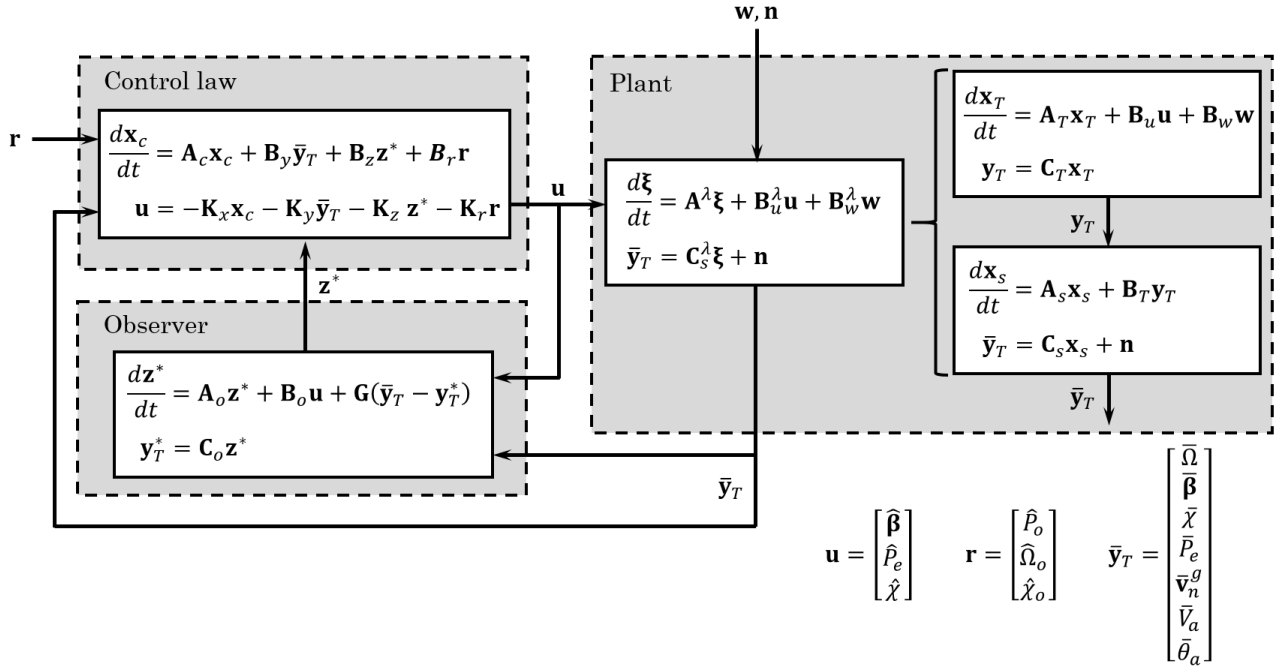2020:00257

VERSION
1.0

43 of 78

Figure 17: The system architecture and terminology used for designing the wind turbine controller.

Table XII: Examples of how some common types of controllers fit into the general architecture of Fig. 17.

Control paradigm	Observer	Control law
PI	(none)	$u = K_P(r - \overline{y}) + K_I x_c$
Output-feedback	(none)	$\mathbf{u} = \mathbf{K}\overline{\mathbf{y}}_T$
LQR, LQG	$\mathbf{z}^*$ observes $\boldsymbol{\xi}$	$\mathbf{u} = \mathbf{K}_z\mathbf{z}^*$
LQR tracking	$\mathbf{z}^*$ observes $\boldsymbol{\xi}$	$\mathbf{u} = \mathbf{K}_z\mathbf{z}^* + \mathbf{K}_x\mathbf{x}_c + \mathbf{K}_r\mathbf{r}$

The control law sets commands

$$\mathbf{u} = \begin{bmatrix}\hat{\boldsymbol{\beta}}\\\hat{P}_e\\\hat{\chi}\end{bmatrix}$$

for respectively the pitch angle of each of the three blades, the electrical power, and the nacelle yaw angle, taking as inputs the sensor measurements $\overline{\mathbf{y}}_T$, observed states $\mathbf{z}^*$, and set-points $\mathbf{r}$. The control law may be dynamic, containing its own states. The control states $\mathbf{x}_c$ often represent integrators for reference tracking, and filters designed to isolate particular frequency bands.

The general linear architecture of Fig. 17 accommodates common control design paradigms, such as those listed in Table XII. In all cases the goal is to arrive at a set of gains $(\mathbf{K}_x, \mathbf{K}_y, \mathbf{K}_z, \mathbf{K}_r)$ that give a desireable level of performance; at least, within the artificial, yet useful, linear world in the immediate vicinity of a selected operating point.

3.1 Optimal control gains

The derivations in this section and the next are adapted from a variety of developments in linear-quadratic control theory: Athans and Falb (1966), Schultz and Melsa (1967), Friedland (1986), Stengel (1994), and Stevens and Lewis (2003). We are wholly in the "linear world" now, and so to be concise we drop the Δ symbols from all the linearized variables.

PROJECT
TotalControl

REPORT NUMBER
2020:00257

VERSION
1.0

44 of 78

Linear-quadratic regulator (LQR) design is a time-domain method, whereby the performance of the system is evaluated in terms of its response to a set of prescribed initial conditions or step functions. Within these confines – linear system, quadradic performance index – there is quite a lot of freedom in terms of how to structure the controller and tune the system behavior. Regardless, the resulting system can, with perhaps some manipulation, be put into the form employed here.

For purposes of the present abbreviated derivation, let us first neglect the disturbances $(\mathbf{w}, \mathbf{n})$, and then write the system of Fig. 17 concisely as

$$\frac{d\mathbf{x}}{dt} = \mathbf{A}\mathbf{x} + \mathbf{B}'\mathbf{u} = \mathbf{A}\mathbf{x} - \mathbf{B}\mathbf{K}\mathbf{x} - \mathbf{B}_r\mathbf{K}_r\mathbf{r}. \tag{146}$$

If we like, we may apply the separation principle, and assume that the states $\boldsymbol{\xi}$ are available directly from the plant; in any case, the system takes the form (146). We now define a quadratic performance index

$$\Pi(\mathbf{x}(t), \mathbf{r}(t)) = \int_t^\infty \mathbf{p}^T\mathbf{W}\mathbf{p}\, d\tau + \boldsymbol{\varepsilon}^T\mathbf{W}_\varepsilon\boldsymbol{\varepsilon}, \quad \mathbf{p} = \mathbf{C}_p\mathbf{x}(\tau) + \mathbf{D}_p\mathbf{u}(\tau), \quad \boldsymbol{\varepsilon} = \mathbf{H}\overline{\mathbf{x}} - \overline{\mathbf{r}}. \tag{147}$$

Here $\overline{\mathbf{x}}$ and $\overline{\mathbf{r}}$ are values attained at the steady state of (146), namely

$$\overline{\mathbf{x}} = (\mathbf{A} - \mathbf{B}\mathbf{K})^{-1}\mathbf{B}_r\mathbf{K}_r\overline{\mathbf{r}}, \tag{148}$$

for some specified $\overline{\mathbf{r}}$. In solving for the optimal gains we assume that the system is initially at rest at $\overline{\mathbf{x}}$, subject to a steady $\overline{\mathbf{r}}$; then, at the initial time t, $\mathbf{r}$ is reduced to zero in a step function. The system then evolves according to

$$\frac{d\mathbf{x}}{dt} = (\mathbf{A} - \mathbf{B}\mathbf{K})\mathbf{x}, \tag{149}$$

and the cost function

$$\Pi = \int_t^\infty \mathbf{p}^T\mathbf{W}\mathbf{p}\, d\tau. \tag{150}$$

Now, the time derivative of (150) is

$$\frac{d\Pi}{dt} = \frac{\partial\Pi}{\partial\mathbf{x}}\frac{d\mathbf{x}}{dt} = -\mathbf{p}^T\mathbf{W}\mathbf{p}, \tag{151}$$

since $d\mathbf{r}/dt = \mathbf{0}$ over the relevant time period, and Π is not a direct function of time. Write (151) as

$$\mathcal{H} = \boldsymbol{\lambda}^T(\mathbf{A}\mathbf{x} + \mathbf{B}'\mathbf{u}) + (\mathbf{x}^T\mathbf{C}_p^T + \mathbf{u}^T\mathbf{D}_p^T)\mathbf{W}(\mathbf{C}_p\mathbf{x} + \mathbf{D}_p\mathbf{u}) = \mathbf{0}. \tag{152}$$

The optimal control is obtained when $\partial\mathcal{H}/\partial\mathbf{u} = \mathbf{0}$, such that

$$\mathbf{B}'^T\boldsymbol{\lambda} + 2\mathbf{D}_p^T\mathbf{W}^T(\mathbf{C}_p\mathbf{x} + \mathbf{D}_p\mathbf{u}^*) = \mathbf{0}, \tag{153}$$

or

$$\mathbf{u}^* = -\frac{1}{2}\mathbf{R}^{-1}\mathbf{B}'^T\boldsymbol{\lambda} - \mathbf{R}^{-1}\mathbf{S}\mathbf{x}, \quad \mathbf{R} = \mathbf{D}_p^T\mathbf{W}\mathbf{D}_p, \quad \mathbf{S} = \mathbf{D}_p^T\mathbf{W}\mathbf{C}_p. \tag{154}$$

Assume that

$$\boldsymbol{\lambda} = 2\mathbf{L}\mathbf{x}, \tag{155}$$

where $\mathbf{L}$ is symmetric. Then

$$\mathbf{u}^* = -\mathbf{K}^*\mathbf{x}, \quad \mathbf{K}^* = \mathbf{R}^{-1}\mathbf{B}'^T\mathbf{L} + \mathbf{R}^{-1}\mathbf{S}. \tag{156}$$

Substituting (155) and (156) into (152) gives a matrix equation

$$\mathbf{L}\mathbf{A} + \mathbf{A}^T\mathbf{L} - 2\mathbf{L}\mathbf{B}'\mathbf{K}^* + \mathbf{Q} - (\mathbf{K}^*)^T\mathbf{S} - \mathbf{S}^T\mathbf{K}^* + (\mathbf{K}^*)^T\mathbf{R}\mathbf{K}^*, \tag{157}$$

where $\mathbf{Q} = \mathbf{C}_p^T\mathbf{W}\mathbf{C}_p$. This can be written

$$\mathbf{L}(\mathbf{A} - \mathbf{B}'\mathbf{R}^{-1}\mathbf{S}) + (\mathbf{A}^T - \mathbf{S}^T\mathbf{R}^{-1}\mathbf{B}'^T)\mathbf{L} - \mathbf{L}\mathbf{B}'\mathbf{R}^{-1}\mathbf{B}'^T\mathbf{L} + \mathbf{Q} - \mathbf{S}^T\mathbf{R}^{-1}\mathbf{S} = \mathbf{0}, \tag{158}$$

to be solved for $\mathbf{L}$, followed by $\mathbf{K}^*$.

PROJECT
TotalControl

REPORT NUMBER
2020:00257

VERSION
1.0

45 of 78

3.2 Optimal observer gains

The computation of a well-performing set of gains for the observer parallels the procedure of Section 3.1 for the controller gains. The approach is to assume that some noise $\mathbf{w}$ is applied to the disturbance (wind and wave input) channels, and $\mathbf{n}$ to the measurement channels, and to tune the noise levels until a desired performance is obtained. The formal derivation (Athans and Tse 1967) involves the complication of continuous-time white noise; yet this formalism is not helpful in our case, where we have no way to characterize the "real" measurement noise $\mathbf{n}$. It is simpler to take a step-function approach to the performance criteria, similar to the one in Section 3.1.

Consider the generic observer structure

$$\frac{d\mathbf{x}^*}{dt} = \mathbf{A}\mathbf{x}^* + \mathbf{B}\mathbf{u} + \mathbf{G}(\overline{\mathbf{y}} - \mathbf{y}^*), \qquad \mathbf{y}^* = \mathbf{C}\mathbf{x}^* + \mathbf{D}\mathbf{u}. \tag{159}$$

Now, we can if desired assume something about the control signal $\mathbf{u}$, whether a profile in time or a control law. If we assume a control law like $\mathbf{K}\mathbf{x}^*$, or if we assume $\mathbf{u} = \mathbf{0}$, the form of the equations is the same. Let us take advantage of the separation principle and tune the observer in the absence of a control signal. Then

$$\frac{d\mathbf{x}^*}{dt} = \mathbf{A}\mathbf{x}^* + \mathbf{G}\boldsymbol{\varepsilon}, \qquad \boldsymbol{\varepsilon} = \overline{\mathbf{y}} - \mathbf{y}^*, \qquad \mathbf{y}^* = \mathbf{C}\mathbf{x}^*. \tag{160}$$

We now consider the following scenario. The observer (160) is at equilibrium, with the measurement taking some value $\overline{\mathbf{y}}$. At time t, the measurement drops to zero. This perturbation could be the result of an actual change in the state of the plant, in which case we would like the observed state $\mathbf{x}^*$ to respond as quickly as possible; or it might be due to noise in the measurement signal, in which case we do not want $\mathbf{x}^*$ to respond. We have, in a sense, a belief state about the signal and noise probabilities. If the measurement signal is noise, then we want to penalize $\boldsymbol{\varepsilon}$; if the measurement signal is real, then we want to penalize $\mathbf{x}^*$. A quadratic cost function could then look like

$$\Pi = \int_t^\infty \mathbf{p}^T \mathbf{W} \mathbf{p} \, d\tau = \int_t^\infty \mathbf{w}^T (\mathbf{p}\mathbf{p}^T) \mathbf{w} \, d\tau, \qquad \mathbf{p} = \mathbf{C_p}\mathbf{x}(\tau) + \mathbf{D}_p \boldsymbol{\varepsilon}(\tau). \tag{161}$$

Clearly (160) and (161) are akin to (149) and (150). The solution, electing to have no cross-terms like $x_i \varepsilon_j$ in the performance index, is

$$(\mathbf{G}^*)^T = \mathbf{R}^{-1}\mathbf{C}\mathbf{L}, \tag{162}$$

$$\mathbf{L}\mathbf{A}^T + \mathbf{A}\mathbf{L} - \mathbf{L}\mathbf{C}^T\mathbf{R}^{-1}\mathbf{C}\mathbf{L} + \mathbf{Q} = \mathbf{0}. \tag{163}$$

3.3 Models of wind and wave processes

Simple models of environmental processes enable the controller to estimate and react to wind and wave disturbances. The effective wind speed and integrated wave forces are each represented with a magnitude and a direction. The wind tends to vary slowly, and is represented by a low-pass filter. But there is also a significant component to the wind loads at the blade passing frequency $3P$, and the controller may benefit from knowing something about this effect; see Smilden *et al.* (2019), for instance. The effective wind component at the blade passing frequency is represented as a band pass filter. The wind model is then

$$\frac{d}{dt}\begin{bmatrix} V_\infty \\ \theta_V \\ \Psi_V \\ V_{3P} \end{bmatrix} = \begin{bmatrix} -\alpha_V & 0 & 0 & 0 \\ 0 & -\alpha_V & 0 & 0 \\ 0 & 0 & 0 & 1 \\ 0 & 0 & -\alpha_{3P}^2 & -2\zeta_{3P}\alpha_{3P} \end{bmatrix}\begin{bmatrix} V_\infty \\ \theta_V \\ \Psi_V \\ V_{3P} \end{bmatrix} + \begin{bmatrix} \alpha_V & 0 \\ 0 & \alpha_V \\ 0 & 0 \\ 2\zeta_{3P}\alpha_{3P} & 0 \end{bmatrix}\begin{bmatrix} V_\infty^e \\ \theta_V^e \end{bmatrix}, \tag{164}$$

where the "e" superscript indicates an external input signal.

The wave forces tend to be sinusoidal, with one or two dominant frequency bands. The dominant frequencies change slowly, and can be reliably measured and forecast, so it is assumed that these are

PROJECT
TotalControl

REPORT NUMBER
2020:00257

VERSION
1.0

46 of 78

known; and for the present purposes it is sufficient to consider one dominant frequency. The amplitude is therefore represented by a second-order band-pass filter, while the direction is considered constant, giving a three-state model,

$$\frac{d}{dt}\begin{bmatrix}\Psi_w \\ F_w \\ \theta_w^g\end{bmatrix} = \begin{bmatrix}0 & 1 & 0 \\ -\omega_w^2 & -2\zeta_w\omega_w & 0 \\ 0 & 0 & 0\end{bmatrix}\begin{bmatrix}\Psi_w \\ F_w \\ \theta_w^g\end{bmatrix}. \tag{165}$$

Following Fossen (1994), also Smilden (2019) we select $\zeta_w = 0.1$, and $\omega_w = 2\pi/T_p$.

The amplitude and direction of the wind are linearized, in terms of available input variables, as

$$\Delta V_\infty = \frac{V_{0,x}}{\sqrt{V_{0,x}^2 + V_{0,x}^2}}\Delta V_x + \frac{V_{0,y}}{\sqrt{V_{0,x}^2 + V_{0,y}^2}}\Delta V_y \tag{166}$$

and

$$\Delta\theta_V = \frac{-V_{0,y}}{V_{0,x}^2 + V_{0,y}^2}\Delta V_x + \frac{V_{0,x}}{V_{0,x}^2 + V_{0,y}^2}\Delta V_y. \tag{167}$$

If we take things literally, these formulas do not apply for the waves, since the mean wave forces are zero. Being practical, we assume that the direction is defined by a characteristic wave force amplitude vector $\mathbf{F}_0$, such that

$$\Delta F_w = \frac{F_{0,x}}{\sqrt{F_{0,x}^2 + F_{0,y}^2}}\Delta F_x + \frac{F_{0,y}}{\sqrt{F_{0,x}^2 + F_{0,y}^2}}\Delta F_y \tag{168}$$

and

$$\Delta\theta_w = \frac{-F_{0,y}}{F_{0,x}^2 + F_{0,y}^2}\Delta F_x + \frac{F_{0,x}}{F_{0,x}^2 + F_{0,y}^2}\Delta F_y. \tag{169}$$

4   Active control of the directional response of a monopile foundation

We have seen in Section 2.3.3 that when the ocean waves and wind are not aligned, the nacelle travels in a pattern that fatigues the foundation around its circumference. It is of interest to know to what extent the pattern of motion can be controlled, and how much actuator effort is needed to do so.

As a case for study, consider the following scenario. The nucleus of a crack has been discovered in a monopile foundation – say, at a weld-line defect in a support fitting for the J tube through which the electrical cable passes. The crack is not critical, but it is desired to prevent its growth. A proposal is made to adjust the control of the wind turbine so as to limit the fluctuating stresses in the critical location. The task is to design a control system that fulfills this objective. Is it practical? Can stresses be reduced by a meaningful amount without unduly worsening the loading on other components?

The possible control actions and available sensors are given respectively in Tables I and II. This is a multiple-input multiple-output control problem. It is complicated by the need to maintain maximum power-point tracking (MPPT) control of the rotor speed. By setting up an appropriate performance index, it is possible to achieve good performance, both in terms of MPPT and load rejection, from the LQR framework.

4.1   Control objectives, performance metrics, and structure

The rotor speed control function of a typical wind turbine controller has two fundamentally different control structures: one when operating so as to maximize the aerodynamic efficiency, and the other in the presence of a command or constraint on the electric power. Under normal operation, the former case occurs below the rated wind speed, and the latter above the rated wind speed. On occasion, a lower (curtailed) power command is set by the plant operator, and in this case the transition between
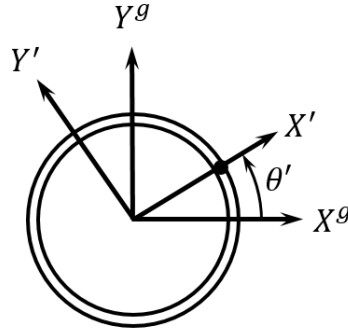
PROJECT
TotalControl

REPORT NUMBER
2020:00257

VERSION
1.0

47 of 78

Figure 18: The definition of a local coordinate system in the foundation, with the X' axis passing through a spot at which a crack or other damage has been detected.

control modes happens at a lower wind speed. In any case, the control-mode transition involves inherently nonlinear saturation of control signals that cannot be handled by linear theory. To limit the scope, we focus on variable-speed operation, below the transition wind speed; this regime is especially interesting, because the tradeoff between energy production and loads is in the forefront.

Below the transition wind speed, the primary goal is to hold the tip-speed ratio at the aerodynamic optimum λ^*, at which the power coefficient obtains its maximum value C_P^*. This is accomplished by a simple quadratic relationship between the generator torque and rotor speed, which is implemented in an open-loop fashion, $T_g = K_\Omega \overline{\Omega}^2$, where $\overline{\Omega}$ is a filtered measurement of the rotor speed. Experience shows that it is difficult to improve on this control strategy, when it comes to maximum power-point tracking (MPPT). (Burton *et al.* 2001)

Since the rotor speed and electrical power must fluctuate with the wind, in order to track the maximum power coefficient C_P^*, it is not desirable to penalize $\Delta\overline{\Omega}$ and $\Delta\hat{P}_e$ independently in the performance metric. Nor is it possible to determine the error with respect to the optimal tip-speed ratio, since this requires knowledge of the effective wind speed. The best estimate of the effective wind speed is obtained through measurement of the rotor speed, which means that the wind speed estimate lags the rotor speed. In other words, the simple open-loop control $K_\Omega \overline{\Omega}^2$ is expected to respond more quickly and effectively than any strategy based on estimating the wind speed, tip-speed ratio, and optimal rotor speed.

Given the primacy of energy production in the economics of wind energy, we propose to design a controller that does not disturb the $K_\Omega \overline{\Omega}^2$ control law, over its effective bandwidth. The requirement that ΔP_e tracks $(3K_\Omega \overline{\Omega}^2)\Delta\overline{\Omega}$, in the framework of LQR control with load-reducing functions, leads to a control architecture as shown in Fig. 19. The observer consists of the nominal open-loop wind turbine model, with states $\boldsymbol{\xi}^*$, as well as observations of the wind speed V_∞, wind direction θ_V, instantaneous wave load amplitude F_w, and wave direction θ_w. The observer is augmented with five integrators: three on the measured blade pitch, one on the power-tracking error, and one on the yaw-tracking error. The integrals of the tracking errors are necessary to ensure reliable tracking when there is uncertainty in the system parameters; while the integrals of blade pitch (collective, cosine, and sine MBC components) serve to drive these to zero at low frequencies, such that they do not interfere with the rotor speed and MPPT control.

Using LQR synthesis, the control law is an outcome of the performance index; that is, the weights in the performance index provide the "knobs" that can be used to tune the system behavior. Stated even more strongly: the weights in the performance index dictate the *structure* of the resulting controller. As such, the formulation of the performance index and its weights are central to the design; in particular, the formulation must penalize any undesired behavior that may be influenced by the control actions,

PROJECT
TotalControl

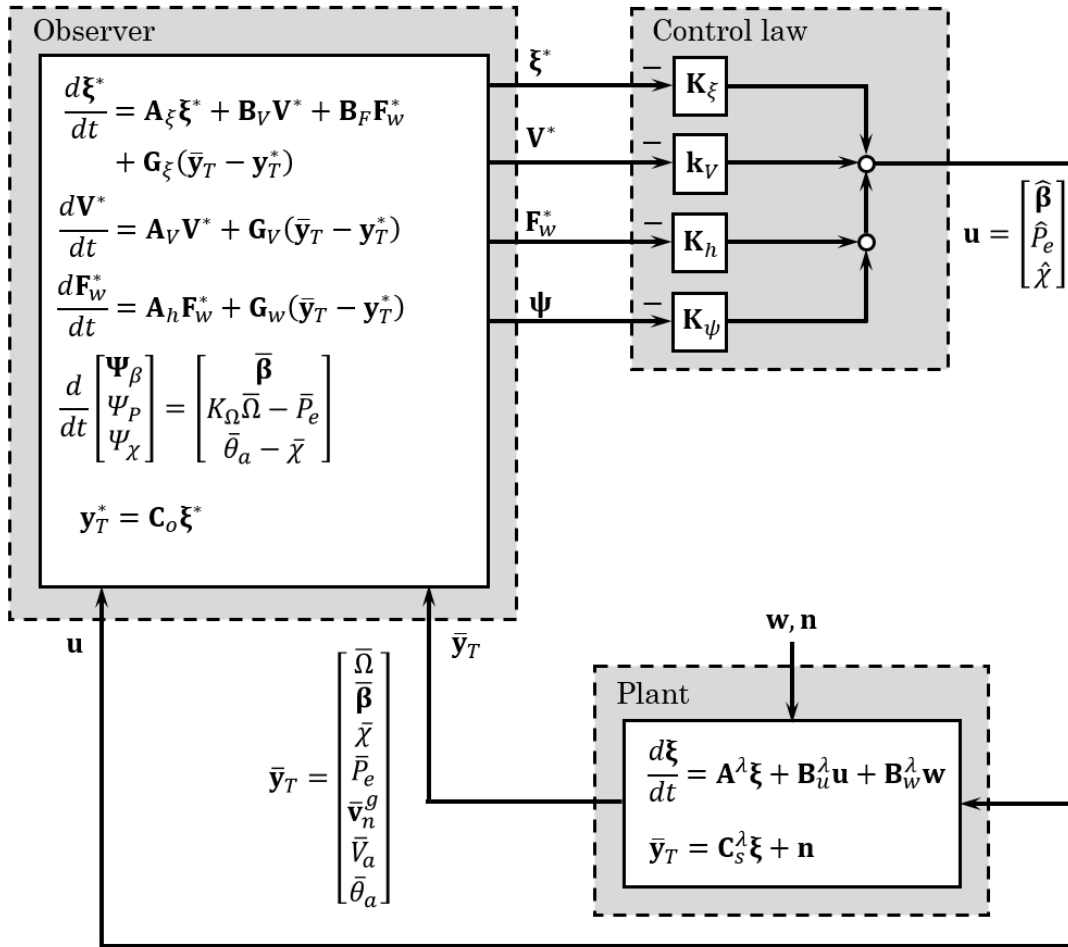REPORT NUMBER
2020:00257

VERSION
1.0

48 of 78

Figure 19: A block diagram of a wind turbine controller based around a state observer. The observer is augmented with observations of bulk environmental effects, and several integral states.

PROJECT
TotalControl

REPORT NUMBER
2020:00257

VERSION
1.0

49 of 78

or result from the control actions. We elect to define the performance index as

$$\Pi = \int_t^T \mathbf{p}^T \mathbf{W} \mathbf{p}\, d\tau, \quad \mathbf{W} = \mathrm{diag}\{\mathbf{w}\} \quad \mathbf{p} = \begin{bmatrix} \Delta\varepsilon_P \\ \Delta\dot{\varepsilon}_P \\ \Delta\Psi_P \\ \Delta\dot{\overline{P}}_e \\ \Delta\dot{\overline{\Omega}} \\ \Delta(\mathbf{v}'_n)_X \\ \Delta(\mathbf{v}'_n)_Y \\ \Delta\dot{\boldsymbol{\beta}} \\ \Delta\boldsymbol{\Psi}_\beta \\ \Delta\varepsilon_\chi \\ \Delta\dot{\varepsilon}_\chi \\ \Delta\Psi_\chi \\ \Delta\hat{\boldsymbol{\beta}} \\ \Delta\hat{P}_e \\ \Delta\hat{\chi} \end{bmatrix}. \tag{170}$$

The performance index contains the following penalties:

1. Proportional, derivative, and integral penalties on $\varepsilon_P = (3\mathbf{K}_\Omega \overline{\Omega}^2)\Delta\overline{\Omega} - \Delta\overline{P}_e$. The integral term provides tracking at low frequencies, while the other terms are used to tweak the response in respectively the mid- and high-frequency bands.

2. A penalty on the rate-of-change of power, $\dot{\overline{P}}_e$, can be used to deaden the response of electrical power to high-frequency drivetrain vibrations.

3. A penalty on the rate-of-change of rotor speed, $\dot{\overline{\Omega}}$, has the opposite effect, causing generator power to be used actively to counter high-frequency drivetrain vibrations.

4. A penalty on the nacelle velocity, as measured by an inertial measurement unit, tends to cause the controller to use pitch, yaw, and electrical power commands to counteract the nacelle motion. Over the frequency band of interest, the nacelle displacement is closely proportional to the internal moments and stress in the foundation. The velocity provides a measure of the fluctuations in displacement, which may be counteracted by the controller without penalizing steady rotor thrust and energy production. The velocity is expressed in the "primed" coordinate system (Fig. 18), where the X' weighting is more severe than the Y' weighting.

5. A penalty on the blade pitch rate discourages the controller from calling for rapid pitch actions that would be damaging to the actuators.

6. A penalty on the integral of blade pitch can be used to drive the pitch to zero at low frequencies, such that it does not interfere with rotor speed and MPPT control.

7. Proportional, derivative, and integral penalties on the yaw error $\varepsilon_\chi = \theta_V^* - \overline{\chi}$ provide yaw control.

8. A penalty on the blade pitch command is required in order to solve for the optimal gains, acting to limit the maximal control input. Penalties are defined in the multi-blade coordinate frame: collective, cosine and sine components. Note that constant values of the cosine and sine components imply sinusoidal pitch inputs at the 1P frequency.

9. Penalizing the electrical power command is required in order to solve for the optimal gains.

10. A penalty on the rotor yaw command is required in order to solve for the optimal gains.

The solution for the optimal gains proceeds by (158).

PROJECT
TotalControl

REPORT NUMBER
2020:00257

VERSION
1.0

50 of 78

4.2 Design and tuning of the observer

The observer consists of a model of the plant, augmented with a highly simplified model of wind and wave processes. It also has five additional states, three being the integrals of the collective, cosine, and sine components of blade pitch; another the integral of the error in power with respect to the maximum power-point tracking algorithm, and the fifth the integral of the yaw offset with respect to the anemometer measurement. These integral states are used to obtain a control law with the appropriate frequency weighting and tracking capability.

The state equations for the observer are

$$\frac{d}{dt}\begin{bmatrix}\boldsymbol{\xi}^* \\ \mathbf{V}^* \\ \mathbf{F}_w^* \\ \boldsymbol{\psi}\end{bmatrix} = \begin{bmatrix}\mathbf{A}_\xi & \mathbf{B}_V & \mathbf{B}_F & \mathbf{0} \\ \mathbf{0} & \mathbf{0} & \mathbf{0} & \mathbf{0} \\ \mathbf{0} & \mathbf{0} & \mathbf{A}_F & \mathbf{0} \\ \mathbf{A}_\psi & \mathbf{0} & \mathbf{0} & \mathbf{0}\end{bmatrix}\begin{bmatrix}\boldsymbol{\xi}^* \\ \mathbf{V}^* \\ \mathbf{F}_w^* \\ \boldsymbol{\psi}\end{bmatrix} + \begin{bmatrix}\mathbf{B}_u \\ \mathbf{0} \\ \mathbf{0} \\ \mathbf{0}\end{bmatrix}\mathbf{u} + \begin{bmatrix}\mathbf{G}_\xi \\ \mathbf{G}_V \\ \mathbf{G}_F \\ \mathbf{0}\end{bmatrix}(\overline{\mathbf{y}} - \mathbf{y}^*) \tag{171}$$

$$\mathbf{y}^* = \begin{bmatrix}\mathbf{C}_\xi & \mathbf{0} & \mathbf{0} & \mathbf{0}\end{bmatrix}\begin{bmatrix}\boldsymbol{\xi}^* \\ \mathbf{V}^* \\ \mathbf{F}_w^* \\ \boldsymbol{\psi}\end{bmatrix} \tag{172}$$

with

$$\mathbf{V}^* = \begin{bmatrix}V_\infty^* \\ \theta_V^*\end{bmatrix}, \quad \mathbf{F}_w^* = \begin{bmatrix}\Psi_w \\ F_w^* \\ \theta_w^*\end{bmatrix}, \quad \boldsymbol{\psi} = \begin{bmatrix}\Psi_\beta \\ \Psi_P \\ \Psi_\chi\end{bmatrix}, \tag{173}$$

and

$$\mathbf{A}_F = \begin{bmatrix}0 & -1 & 0 \\ -\alpha_w^2 & -2\zeta_w\alpha_w & 0 \\ 0 & 0 & 0\end{bmatrix}, \quad \mathbf{A}_\psi = \begin{bmatrix}\mathbf{c}_\beta \\ K_\Omega\mathbf{c}_\Omega - \mathbf{c}_P \\ \mathbf{c}_\theta - \mathbf{c}_\chi\end{bmatrix}. \tag{174}$$

The questions to be answered are (1), which modes should be included in $\boldsymbol{\xi}^*$? And (2), how should we set the weights of the $\mathbf{Q}$ and $\mathbf{R}$ matrices from (163)? There is quite some freedom in how we could approach the design of the observer, and to some extent the choice is philosophical. For instance, do we want a minimum-state observer, or a minimum-effort observer (one that minimizes the designer's effort)? Do we insist that the observer states should be interpretable by a human, or may we use system identification methods to generate matrices that to our unaided eye are just a collection of numbers?

Let us take the tactic of designing a low-design-effort observer; in doing so, we should be prepared that the observer will have more states than necessary. There are three arguments for doing things in this way, none of which are absolutely compelling – other approaches could be just as effective; see, for instance, Smilden (2019). In any case, the first argument is that the control architecture of Fig. 19 is quite general; developing a minimum-effort observer around this architecture will allow us to efficiently study different control objectives. The second argument is that, in evaluating the potential for load-reducing control functions, we do not want the observer to be the primary limitation on the performance; retaining more than the minimum system dynamics provides some margin of error here. The third argument is that it is easier to come back later and reduce the number of states in a high-order observer, than to try to add states to improve the performance of a minimal observer. When it comes to human-interpretability, we shall start with a modal observer, whose states – in principle, at least – can be understood; then, system identification and reduction can be done in a following step.[18]

The observer was generated by the following procedure:

---

[18]As recommended by Zhou *et al.* (1996) we delay reduction of the embedded model until the controller gains are completely specified – and then apply model-reduction procedures on the complete controller.

PROJECT
TotalControl

REPORT NUMBER
2020:00257

VERSION
1.0

51 of 78

1. The steady-state operating point of the wind turbine was computed by solving the nonlinear equations, using a default nonlinear controller (Merz *et al.* 2019).

2. Using the state vector at the operating point, an open-loop model of the wind turbine was generated. This included sensor dynamics (a bank of low-pass filters) and a lower-level generator power tracking controller. The open-loop model had 296 states.

3. The eigenmodes of the open-loop model were computed.

4. Every control-to-sensor and disturbance-to-sensor transfer function was computed, with the magnitudes listed in Table XIII. Significant transfer functions were flagged for further analysis, while those near zero were neglected, such that they did not influence the choice of modes to retain.

5. For every significant transfer function in Table XIII, the projections (17) were computed, giving the contribution from each mode.[19] These modal contributions were ranked in descending order, and a sufficient number of modes retained such that the transfer functions were reproduced within an accuracy of 5%.

6. (Optional): Modes with a natural frequency above 4 Hz were considered to be quasi-steady; the modal matrices were partitioned into

$$\begin{bmatrix} \mathbf{A}_{dd} & \mathbf{A}_{ds} \\ \mathbf{A}_{sd} & \mathbf{A}_{ss} \end{bmatrix}, \quad \begin{bmatrix} \mathbf{B}_{d} \\ \mathbf{B}_{s} \end{bmatrix}, \quad \begin{bmatrix} \mathbf{C}_{d} & \mathbf{C}_{s} \end{bmatrix};$$

then, solving for the quasi-steady states,

$$\frac{d\mathbf{x}_d}{dt} = (\mathbf{A}_{dd} - \mathbf{A}_{ds}\mathbf{A}_{ss}^{-1}\mathbf{A}_{sd})\mathbf{x}_d + (\mathbf{B}_d - \mathbf{A}_{ds}\mathbf{A}_{ss}^{-1}\mathbf{B}_s)\mathbf{u}, \tag{175}$$

$$\mathbf{y} = (\mathbf{C}_d - \mathbf{C}_s\mathbf{A}_{ss}^{-1}\mathbf{A}_{sd})\mathbf{x}_d - \mathbf{C}_s\mathbf{A}_{ss}^{-1}\mathbf{B}_s\mathbf{u}. \tag{176}$$

7. The observer was augmented with states representing the environmental disturbances: $\mathbf{V}^*$ and $\mathbf{F}_w^*$ in (171). (The integrators $\boldsymbol{\psi}$ in Fig. 19 are relevant only for the control law, not the tuning of the observer, and so these are neglected in the present development.)

Skipping Step (6), retaining the full set of dynamic modes, the resulting observer has 251 states: 244 open-loop modes and 7 environmental states.[20]

We turn now to the second major question, how to set the weights in the $\mathbf{Q}$ and $\mathbf{R}$ matrices. Since "optimal" gains are obtained when $\mathbf{Q}$ represents the covariance of the state variables, it is expected that a good tuning will result if we can approximate this covariance. For this purpose we pick one or several frequencies that are expected to be in the range of the significant environmental effects $\mathbf{w}$, and then compute the matrix of transfer functions $\mathbf{H} = \partial \mathbf{x}/\partial \mathbf{w}$ at these frequencies. Here the chosen frequencies were 0.02 Hz, for low-frequency wind; 0.17 Hz, for ocean waves; 0.24 Hz, for tower resonance; and 0.40 Hz, for the $3P$ blade passing frequency. Disturbances $\mathbf{w}$ were taken to be the rotor-average wind speed, wind direction, rotor-wide cosine and sine (multi-blade coordinate) wind components, waterline wave force, and wave direction: quantities that represent, in bulk, the primary environmental loads during operation. The $\mathbf{Q}$ matrix was then chosen as

$$\mathbf{Q} = \Re\{\mathbf{H}\,\mathrm{diag}[\boldsymbol{\gamma}\circ\boldsymbol{\gamma}]\,\mathbf{H}^{*T}\}, \tag{177}$$

with $\boldsymbol{\gamma}$ a vector of weights, containing the estimated variance of each component of $\mathbf{w}$. After $\mathbf{Q}$ was determined, the weights along the diagonal of the $\mathbf{R}$ matrix were tuned to give good performance;

---

[19]The imaginary component of (17) was also checked, to make sure that there was not a significant bias orthogonal to the direction of the projection.

[20]The number of states can be reduced by an order of magnitude by applying model-reduction techniques.

PROJECT
TotalControl

REPORT NUMBER
2020:00257

VERSION
1.0

52 of 78

Table XIII: Case 10-2-x: The magnitudes of control-to-sensor and disturbance-to-sensor transfer functions at representative frequencies, these being the steady state (upper block), at 0.17 Hz (second block) at the peak ocean wave frequency, at 0.24 Hz (third block) at the first tower resonant frequency, and at 0.40 Hz (lower block) near the blade passing frequency.

	$\overline{\Omega}$	$\overline{\beta}_\emptyset$	$\overline{\beta}_c$	$\overline{\beta}_s$	$\overline{\chi}$	$\overline{P}_e$	$(\overline{v}_n^g)_x$	$(\overline{v}_n^g)_y$	$\overline{V}$	$\overline{\theta}_V$
$\hat{\beta}_\emptyset$	13.835	1.0094	0.0300	0.0090	0.0879	1.1707	0.5882	0.0498	0.0000	0.0000
$\hat{\beta}_c$	0.7833	0.0026	0.9646	0.2904	0.4146	0.0663	0.0314	0.0182	0.0000	0.0000
$\hat{\beta}_s$	0.1508	0.0004	0.2891	0.9862	0.1438	0.0128	0.0703	0.0136	0.0000	0.0000
$\hat{P}_e$	0.2510	0.0007	0.0005	0.0001	0.0015	0.9787	0.0098	0.0010	0.0000	0.0000
$\hat{\chi}$	0.3502	0.0137	0.0208	0.0088	0.9688	0.0296	0.0128	0.0422	0.0000	0.0000
V_∞	0.6122	0.0017	0.0012	0.0004	0.0037	0.0518	0.0246	0.0022	0.9950	0.0000
θ_V	0.0508	0.0001	0.0001	0.0001	0.0010	0.0043	0.0035	0.0002	0.0000	0.9950
V_c	0.0076	0.0000	0.0001	0.0000	0.0089	0.0006	0.0004	0.0002	0.0000	0.0000
V_s	0.0060	0.0000	0.0000	0.0005	0.0014	0.0005	0.0015	0.0010	0.0000	0.0000
F_w	0.0020	0.0000	0.0000	0.0000	0.0000	0.0002	0.0029	0.0017	0.0000	0.0000
θ_w	0.0015	0.0000	0.0000	0.0000	0.0000	0.0001	0.0017	0.0030	0.0000	0.0000
$\hat{\beta}_\emptyset$	2.3065	1.0142	0.0135	0.0062	0.0296	0.9896	1.1521	0.0407	0.0000	0.0000
$\hat{\beta}_c$	0.0579	0.0008	0.9640	0.2912	0.4069	0.0248	0.1215	0.0603	0.0000	0.0000
$\hat{\beta}_s$	0.0242	0.0002	0.2893	0.9858	0.1410	0.0104	0.3521	0.0810	0.0000	0.0000
$\hat{P}_e$	0.0306	0.0001	0.0001	0.0001	0.0003	0.9859	0.0074	0.0021	0.0000	0.0000
$\hat{\chi}$	0.0892	0.0140	0.0220	0.0089	0.9918	0.0383	0.0320	0.1684	0.0000	0.0000
V_∞	0.0802	0.0004	0.0004	0.0002	0.0005	0.0344	0.0309	0.0014	0.8944	0.0000
θ_V	0.0043	0.0000	0.0001	0.0001	0.0007	0.0019	0.0158	0.0009	0.0000	0.8944
V_c	0.0003	0.0000	0.0001	0.0000	0.0088	0.0001	0.0013	0.0007	0.0000	0.0000
V_s	0.0011	0.0000	0.0000	0.0005	0.0014	0.0005	0.0077	0.0050	0.0000	0.0000
F_w	0.0013	0.0000	0.0000	0.0000	0.0000	0.0006	0.0151	0.0089	0.0000	0.0000
θ_w	0.0008	0.0000	0.0000	0.0000	0.0000	0.0003	0.0088	0.0155	0.0000	0.0000
$\hat{\beta}_\emptyset$	0.0979	0.9961	0.0020	0.0104	0.0394	0.2546	32.294	9.6609	0.0000	0.0000
$\hat{\beta}_c$	0.2344	0.0219	0.9761	0.3018	0.1056	0.6097	6.7308	27.967	0.0000	0.0000
$\hat{\beta}_s$	0.3016	0.0163	0.3029	0.9797	0.0802	0.7845	9.7721	15.906	0.0000	0.0000
$\hat{P}_e$	0.0060	0.0001	0.0001	0.0000	0.0012	0.9679	0.0431	0.1131	0.0000	0.0000
$\hat{\chi}$	1.6404	0.1642	0.0412	0.0182	0.4868	4.2670	7.5112	161.67	0.0000	0.0000
V_∞	0.0028	0.0001	0.0001	0.0003	0.0010	0.0072	0.7413	0.1240	0.3846	0.0000
θ_V	0.0079	0.0003	0.0003	0.0002	0.0018	0.0204	0.4283	0.3266	0.0000	0.3846
V_c	0.0054	0.0005	0.0004	0.0000	0.0025	0.0140	0.0657	0.6057	0.0000	0.0000
V_s	0.0062	0.0004	0.0002	0.0004	0.0032	0.0161	0.2152	0.3784	0.0000	0.0000
F_w	0.0101	0.0005	0.0004	0.0000	0.0069	0.0263	0.4599	0.6738	0.0000	0.0000
θ_w	0.0130	0.0009	0.0005	0.0001	0.0104	0.0337	0.3110	1.0226	0.0000	0.0000
$\hat{\beta}_\emptyset$	0.3413	1.0036	0.0185	0.0065	0.0508	1.8597	4.9712	1.1017	0.0000	0.0000
$\hat{\beta}_c$	0.0932	0.0044	0.9536	0.3222	0.2144	0.5078	1.1055	4.6642	0.0000	0.0000
$\hat{\beta}_s$	0.0464	0.0016	0.3161	0.9675	0.0858	0.2527	1.3333	2.0431	0.0000	0.0000
$\hat{P}_e$	0.0030	0.0000	0.0000	0.0001	0.0002	0.9341	0.0038	0.0068	0.0000	0.0000
$\hat{\chi}$	0.1383	0.0090	0.0199	0.0019	0.2797	0.7537	0.0818	5.9524	0.0000	0.0000
V_∞	0.0094	0.0003	0.0004	0.0002	0.0002	0.0510	0.1105	0.0027	0.2425	0.0000
θ_V	0.0003	0.0000	0.0001	0.0002	0.0013	0.0019	0.0603	0.0274	0.0000	0.2425
V_c	0.0018	0.0001	0.0002	0.0001	0.0041	0.0100	0.0100	0.0885	0.0000	0.0000
V_s	0.0005	0.0000	0.0001	0.0005	0.0007	0.0025	0.0281	0.0278	0.0000	0.0000
F_w	0.0015	0.0001	0.0001	0.0000	0.0006	0.0084	0.0892	0.0554	0.0000	0.0000
θ_w	0.0017	0.0001	0.0001	0.0000	0.0010	0.0091	0.0512	0.0895	0.0000	0.0000

PROJECT
TotalControl

REPORT NUMBER
2020:00257

VERSION
1.0

53 of 78

Table XIV: Case 10-2-x: Final tuning of the state observer, in units of (rad, m, s, Mkg).

$\boldsymbol{\gamma}$, disturbances		$\mathbf{R}$, sensors	
V_∞	1.00	$\overline{\Omega}$	0.0250
θ_V	0.10	$\overline{\beta}_\emptyset$	0.0013
V_c	1.00	$\overline{\beta}_c$	0.0013
V_s	1.00	$\overline{\beta}_s$	0.0013
V_{3P}	1.00	$\overline{\chi}$	0.0013
F_w	1.00	$\overline{P}_e$	0.0050
θ_w	0.10	$(\overline{v}_n')_X$	0.0130
		$(\overline{v}_n')_Y$	0.0130
		$\overline{V}_a$	0.5000
		$\overline{\theta}_a$	0.0500

Table XIV lists the observer weights. We judge the quality of an observer initially according to whether the observer can drive the error $\overline{\mathbf{y}} - \mathbf{y}^*$ to steady state faster than 0.5 s (bandwidth > 2 Hz), which is several times faster than the expected control actions. Then the performance of the observer must be verified in closed-loop operation.

The dynamics of the isolated observer are shown in Figs. 20 and 21. Figure 20 shows all 100 components of the $\partial\mathbf{y}^*/\partial\overline{\mathbf{y}}$ transfer function. The sensor input $\overline{\mathbf{y}}$ is that labeled by text on the plot, while the output $\mathbf{y}^*$ is coded by color. A striking feature of the observer is that it does not reproduce the sensor signals in the steady state; that is, the error $\boldsymbol{\varepsilon}_y = \overline{\mathbf{y}} - \mathbf{y}^*$ does not go to zero, especially in the case of the three blade pitch signals. To explain this fact, let us look at the error dynamics, which are

$$\frac{\partial\boldsymbol{\varepsilon}_y}{\partial\overline{\mathbf{y}}} = \frac{\partial\overline{\mathbf{y}}}{\partial\overline{\mathbf{y}}} - \frac{\partial\mathbf{y}^*}{\partial\overline{\mathbf{y}}} = \mathbf{I}_y - \mathbf{C}\frac{\partial\mathbf{x}^*}{\partial\overline{\mathbf{y}}}. \tag{178}$$

Now,

$$\frac{\partial\mathbf{x}^*}{\partial\overline{\mathbf{y}}} = [i\omega\mathbf{I}_x - (\mathbf{A} - \mathbf{GC})]^{-1}\mathbf{G}, \tag{179}$$

so

$$\frac{\partial\boldsymbol{\varepsilon}_y}{\partial\overline{\mathbf{y}}} = \mathbf{I}_y - \mathbf{C}[i\omega\mathbf{I}_x - (\mathbf{A} - \mathbf{GC})]^{-1}\mathbf{G}, \tag{180}$$

or at steady state,

$$\frac{\partial\boldsymbol{\varepsilon}_y}{\partial\overline{\mathbf{y}}} = \mathbf{I}_y + \mathbf{C}(\mathbf{A} - \mathbf{GC})^{-1}\mathbf{G}. \tag{181}$$

This does in fact go to zero if the gain $\mathbf{G}$ is large enough; but a large gain would imply perfect certainty and high bandwidth for the sensor measurements. In fact, what Fig. 20 tells us is that, in the absence of control commands, very little information is contained in the blade pitch measurements. These could just as well be eliminated from the list of sensor inputs to the observer. The useful blade pitch information comes from the pitch command itself, as is seen in Fig. 21, which shows the 50 $\partial\mathbf{y}^*/\partial\mathbf{u}$ transfer functions.

4.3 Control actions and closed-loop dynamics

We select Case 10-2-30 from Table XI to investigate in some depth, before proceeding to a broader survey of results in Section 4.4. Let the wind be aligned with the X^g direction, and, following the load case definition, the waves are then at $\theta_w = 30°$. Let the crack in the foundation, the location we are trying to protect, be located at $\theta' = 60°$, between the X^g and Y^g axes (Fig. 18). At this point the goal is to study the *possibilities* of directional load control, rather than a final tuning; so let us emphasize the directionality by penalizing only nacelle motions in the X' direction (alternating stresses on the crack), with no penalty at all in the Y' direction.
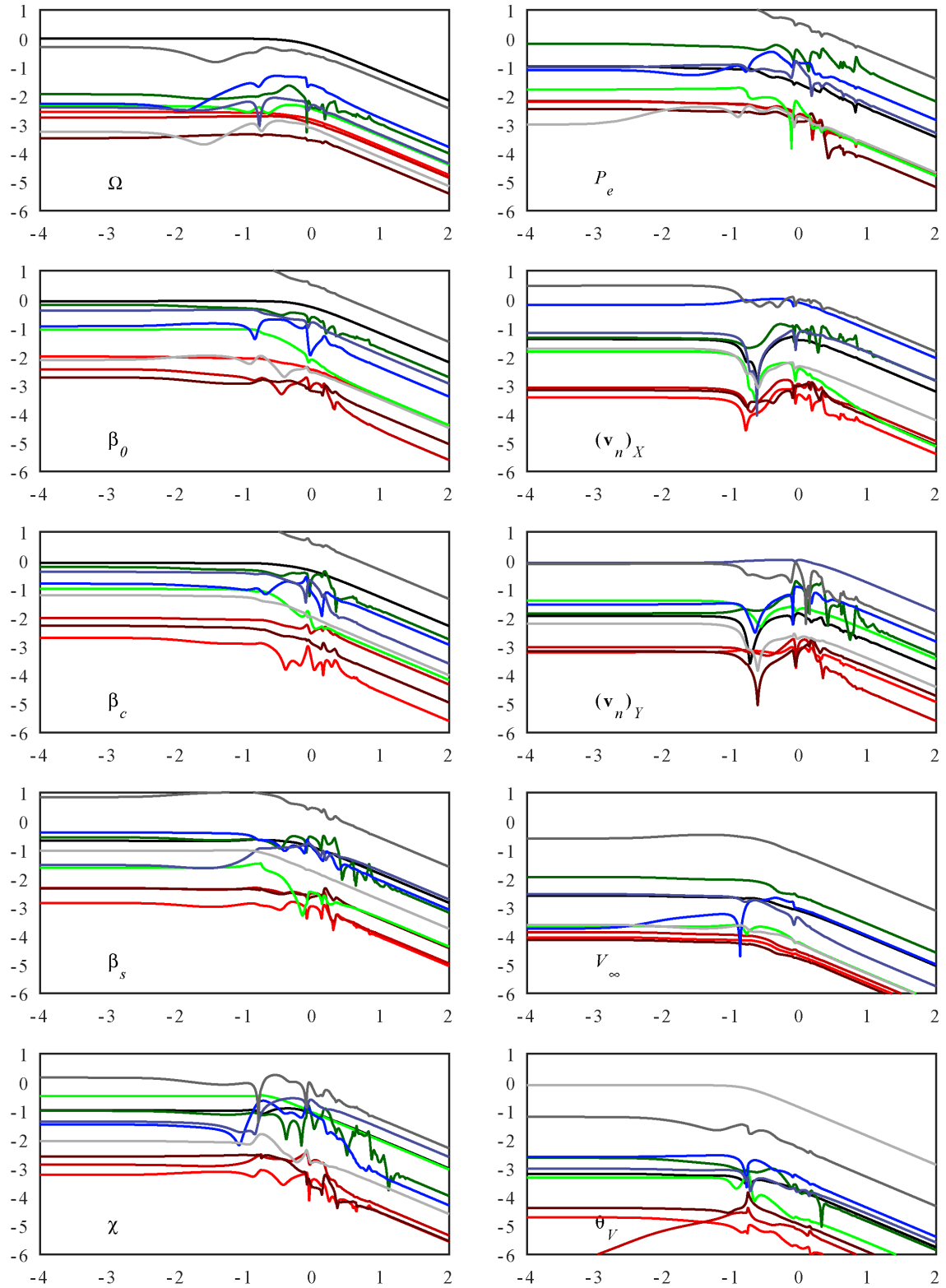
Figure 20: Case 10-2-x: Transfer functions from $\overline{\mathbf{y}}$ to $\mathbf{y}^*$ for the observer of Table XIV. The X and Y axes are logarithmically scaled, the X axis units are $log_{10}(\text{Hz})$, and each plot is annotated with the input $\overline{\mathbf{y}}$ variable. Curves are color-coded according to the $\mathbf{y}^*$ variable: Ω (black), $\beta_\emptyset$ (light red), β_c (red), β_s (dark red), χ (light green), P_e (dark green), $(\mathbf{v}_n)_X$ (light blue), $(\mathbf{v}_n)_Y$ (dark blue), V_∞ (dark gray), and θ_V (light gray).

PROJECT
TotalControl

REPORT NUMBER
2020:00257

VERSION
1.0

55 of 78
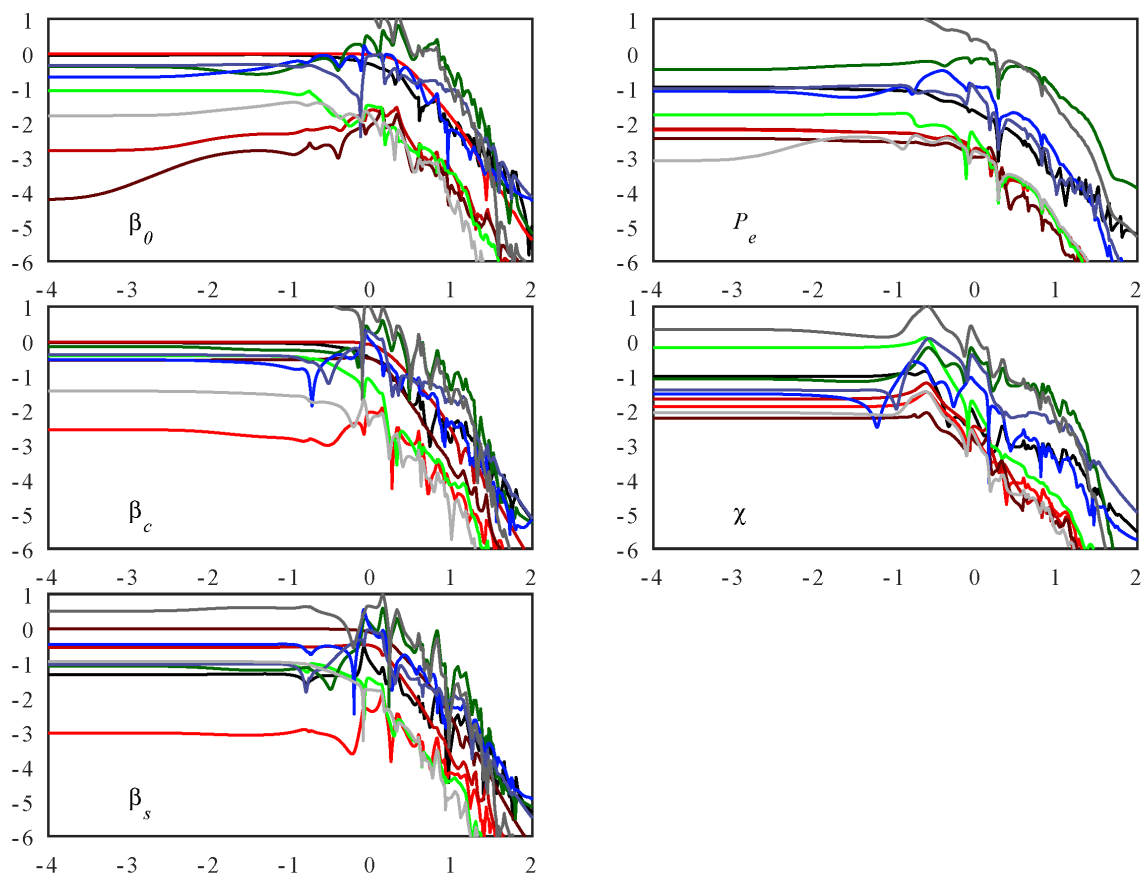
Figure 21: Case 10-2-x: Transfer functions from **u** to **y*** for the observer of Table XIV. See Fig. 20 for the legend.

PROJECT
TotalControl

REPORT NUMBER
2020:00257

VERSION
1.0

56 of 78

Table XV: Case 10-2-30: Progressive tuning of the controller. RSC: baseline rotor speed/MPPT control, AD: active tower damping with collective pitch, IBP: individual blade pitch

	RSC	AD	IBP	AD2	IBP2
ε_P	2	2	2	2	2
$\dot{\varepsilon}_P$	0	0	0	0	0
Ψ_P	10	10	10	10	10
$\dot{P}_e$	0.5	0.5	0.5	0.5	0.5
$\dot{\Omega}$	0	0	0	0	0
$(\mathbf{v}'_n)_X$	0	**15**	15	15	15
$(\mathbf{v}'_n)_Y$	0	0	0	**15**	**15**
$\dot{\beta}_\emptyset$	0	**10**	10	10	10
$\dot{\beta}_c$	0	0	**10**	0	10
$\dot{\beta}_s$	0	0	**10**	0	10
$\Psi_{\beta\emptyset}$	1	**20**	20	20	20
$\Psi_{\beta c}$	0	0	**1**	0	1
$\Psi_{\beta s}$	0	0	**1**	0	1
ε_χ	0	0	0	0	0
$\dot{\varepsilon}_\chi$	0	0	0	0	0
Ψ_χ	0	0	0	0	0
$\hat{\beta}_\emptyset$	(big)	**50**	50	50	50
$\hat{\beta}_c$	(big)	(big)	**20**	(big)	20
$\hat{\beta}_s$	(big)	(big)	**20**	(big)	20
$\hat{P}_e$	1	1	1	1	1
$\hat{\chi}$	(big)	(big)	(big)	(big)	(big)

The starting point is a basic rotor speed controller, Controller RSC, where the power command tracks the $K_\Omega \Omega^3$ profile. This controller is obtained using the weights in the first column of Table XV. Figures 22 and 23 summarize the dynamic response, showing the transfer functions from the rotor-average wind speed and waterline wave force to the blade pitch, electric power, rotor speed, and nacelle motion. Controller RSC has no blade pitch: the plot is scaled logarithmically, so the residual values of pitch are small. The electrical power tracks the rotor speed according to the desired law, with a roll-off frequency around 0.05 Hz consistent with the natural timescale of the rotor inertia at this wind speed. No effort is made to damp the tower motions, so a severe resonant response is evident. We are most concerned with the response in the X' direction, which stresses the critical location on the foundation; this is the set of bright blue curves. The peak at 0.24 Hz is associated with the tower resonant frequency, and since the defect is located at 60°, the X' direction receives contributions from both the fore-aft and side-to-side motion.

Having established the baseline performance, we now introduce control actions that are designed to protect the critical location on the foundation. First, we allow use of the generator and collective blade pitch. These actions interfere with the control of the rotor speed, and their use must be limited to a frequency band not much below the first tower resonant frequency. A reasonable tuning is that of Controller AD, in Table XV. A significant penalty is placed on on motion in the X' direction. At the same time, the penalty on the collective blade pitch command is reduced such that this can become active. Additional penalties are then placed on the collective pitch rate and pitch integral: the former, to limit high-frequency actuation, and the latter, to avoid interfering with MPPT at low frequencies.

As seen in Fig. 22, Controller AD actively pitches the blades, with somewhat over 1° pitch amplitude per unit wind speed (m/s) or wave force (MN) amplitude, over a frequency band from the wave frequency (0.17 Hz) to the $3P$ frequency (0.4 Hz). The result, referring to Fig. 23, is a reduction in the tower motion over this frequency band; in particular, the resonant peak in the critical direction is all but eliminated. An added benefit is the reduction of fluctuations in the rotor speed and electric power. It is evident that the control of rotor speed and MPPT is not significantly degraded.

Controller IBP in Table XV represents a tuning that allows active use of individual blade pitch,

PROJECT
TotalControl

REPORT NUMBER
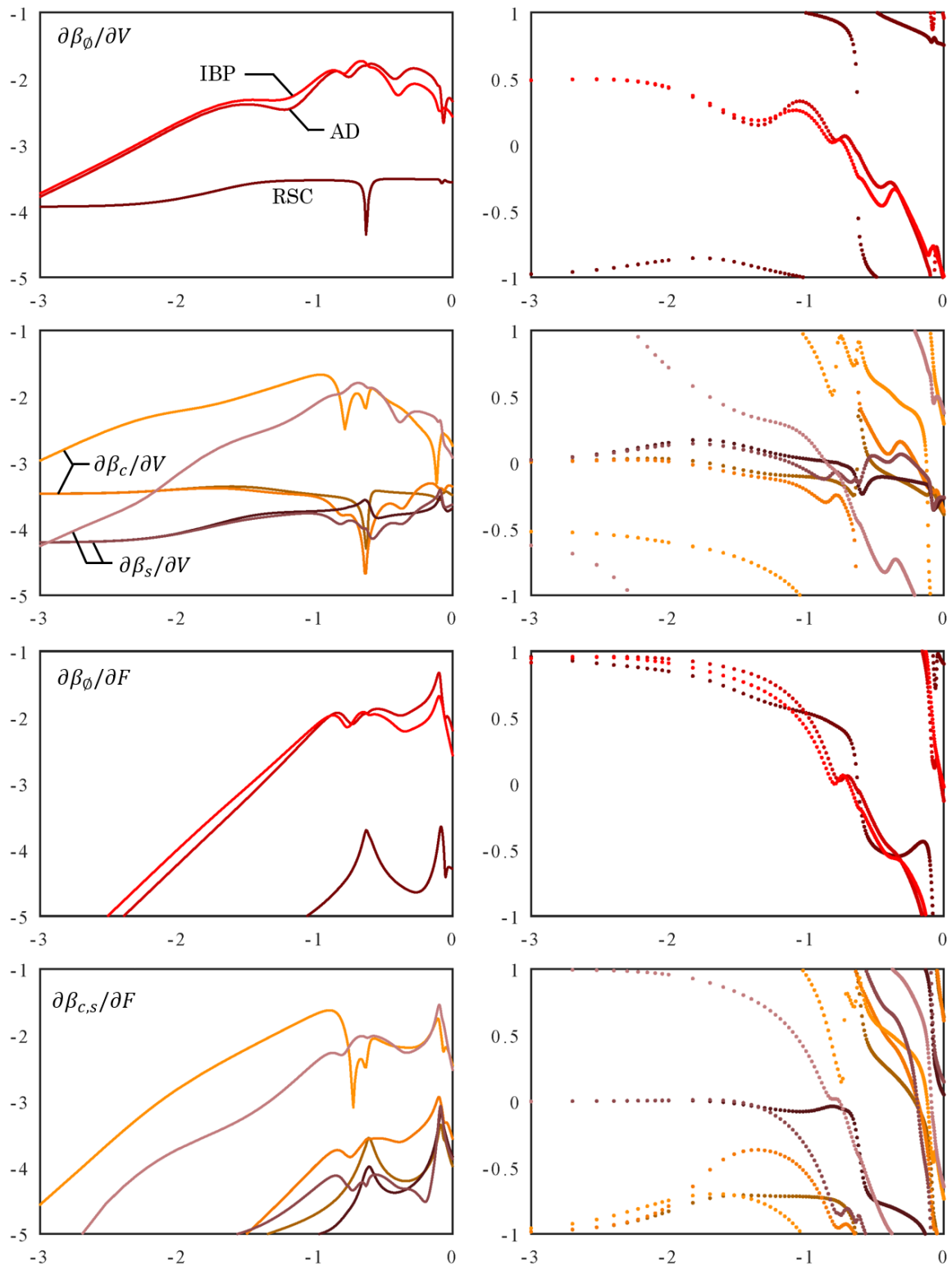2020:00257

VERSION
1.0

57 of 78

Figure 22: Case 10-2-30, critical spot 60°: Transfer functions from wind speed and wave load to blade pitch, for Controllers RSC, AD, and IBP. The column at left shows magnitudes, and at right the phase angles, normalized by π. Red: collective pitch; dark red: cosine pitch; orange: sine pitch. The X axis scale is $log_{10}(Hz)$. The curves for the RSC controller are drawn in a darker shade; AD medium; and IBP lighter.
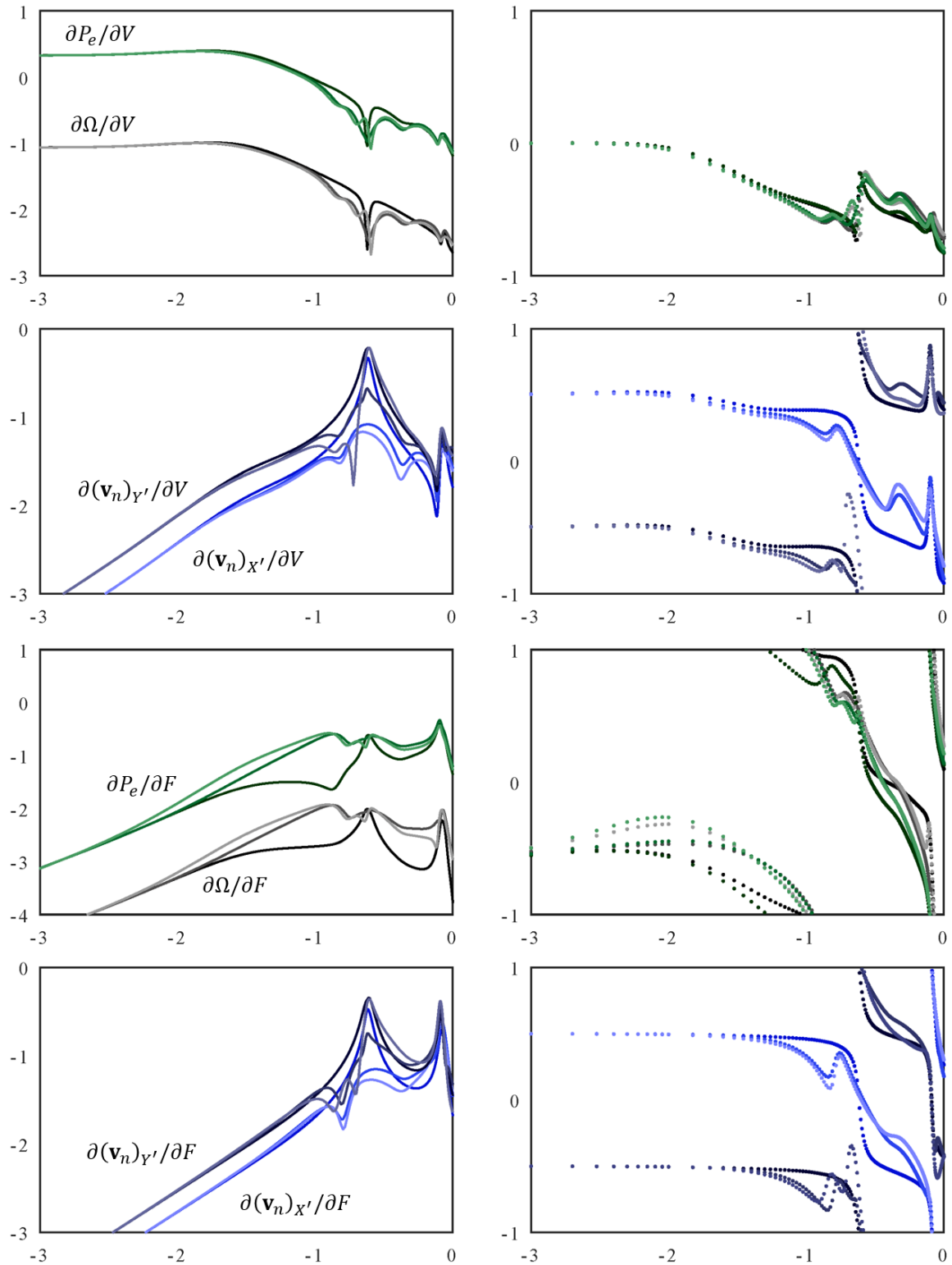
PROJECT
TotalControl

REPORT NUMBER
2020:00257

VERSION
1.0

58 of 78

Figure 23: Case 10-2-30, critical spot 60°: Transfer functions from wind speed and wave load to electric power, rotor speed, and nacelle velocity, for Controllers RSC, AD, and IBP. The column at left shows magnitudes, and at right the phase angles, normalized by π. The curves for the RSC controller are drawn in a darker shade; AD medium; and IBP lighter.
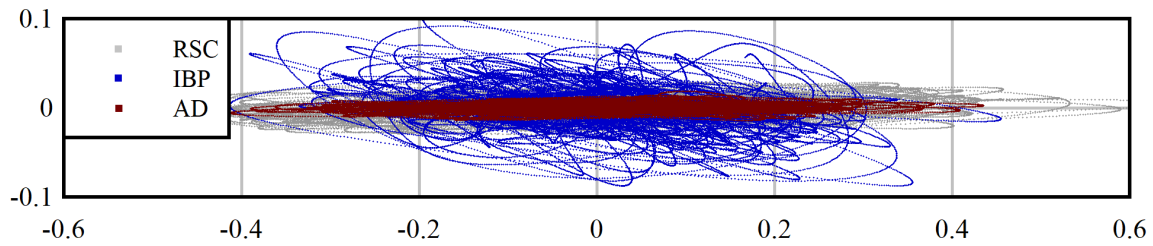
Figure 24: Case 10-2-30, critical spot 60°: Time series of normalized nacelle displacements under stochastic V and F_w inputs, with energy uniformly distributed over frequencies between 0.05 and 0.50 Hz.

in addition to collective pitch. Note that the signals seen in Fig. 22 are *modulations* of individual blade pitch at the given frequency – even constant IBP, at zero frequency, involves active pitching as the blades rotate about the azimuth. It is interesting what the optimal control does: it modulates the cosine and sine components at a relative phase offset of around π. This implies a sort of diagonal motion of the rotor. Unfortunately, constraints on the time and scope of this report prevent a deep investigation into the dynamics; this is flagged as a topic for future study. Suffice it to say that the result of the individual blade pitch action is to squeeze a bit further reduction of motion in the X' direction, at the cost of worsened resonance in the Y' direction: indeed, the controller is "steering" the tower motions away from the critical location, which is the effect we wanted to achieve. That said, in a practical sense, the minor gains (remember, this is a log scale) are sure to be more than offset by the increase in the overall level of vibration. Indeed, time-domain plots of the nacelle response under random V and F_w inputs, Fig. 24, bear this out.

It is emphasized that the poor performance of individual blade pitch control in Fig. 24 is an artifact of the asymmetric penalties placed on the tower motion. When the tower motion is penalized evenly, individual blade pitch control can help in rejecting tower side-to-side motions. Figure 25 shows the response spectra of the controls and nacelle motion, using the turbulence model of Section 2.1.11, when the tower motion is penalized evenly. Under this particular setting of weights in the performance index, the controller prefers to use modulation of individual blade pitch, rather than generator torque, to reject tower side-to-side motions. Controller IBP2 is highly effective, virtually cancelling tower motion (again, the scale in the plot is logarithmic) due to ocean waves and resonant vibrations, and reducing to some extent the response to $3P$ thrust fluctuations.

4.4 Performance as a function of wave direction

Figures 26 through 29 show the performance of Controller IBP as a function of the wave direction. It can be discerned from these plots that the ocean waves are responsible for the majority of the tower resonant oscillations; for instance, observe in Fig. 29, the light gray curves, that little blade pitch action is needed to counter the resonant-frequency motion in the direction of the wind. In this case the principle effect of the controller is to reject the $3P$ blade-passing frequency component of the rotor thrust. Overall, there is indeed the obvious tradeoff between load reduction and pitch actuator usage, and it could be beneficial, in the context of reducing actuator wear, to "de-tune" the degree of load rejection away from the critical location. For comparison, Figure 30 shows the response spectra of Controller IBP2, which attempts to reject all tower motions.

To summarize: it is indeed possible to design a controller that "steers" the motion of the nacelle into one direction, and away from another. There may be a practical benefit in doing so, in terms of reducing actuator wear. However, the potential benefit is most pronounced when the wind and waves are orthogonal, which is not a common event. In the event that the difference in X' and Y' motions is extreme, the expected load reduction in the X' direction might not be realizable. A more robust

PROJECT
TotalControl

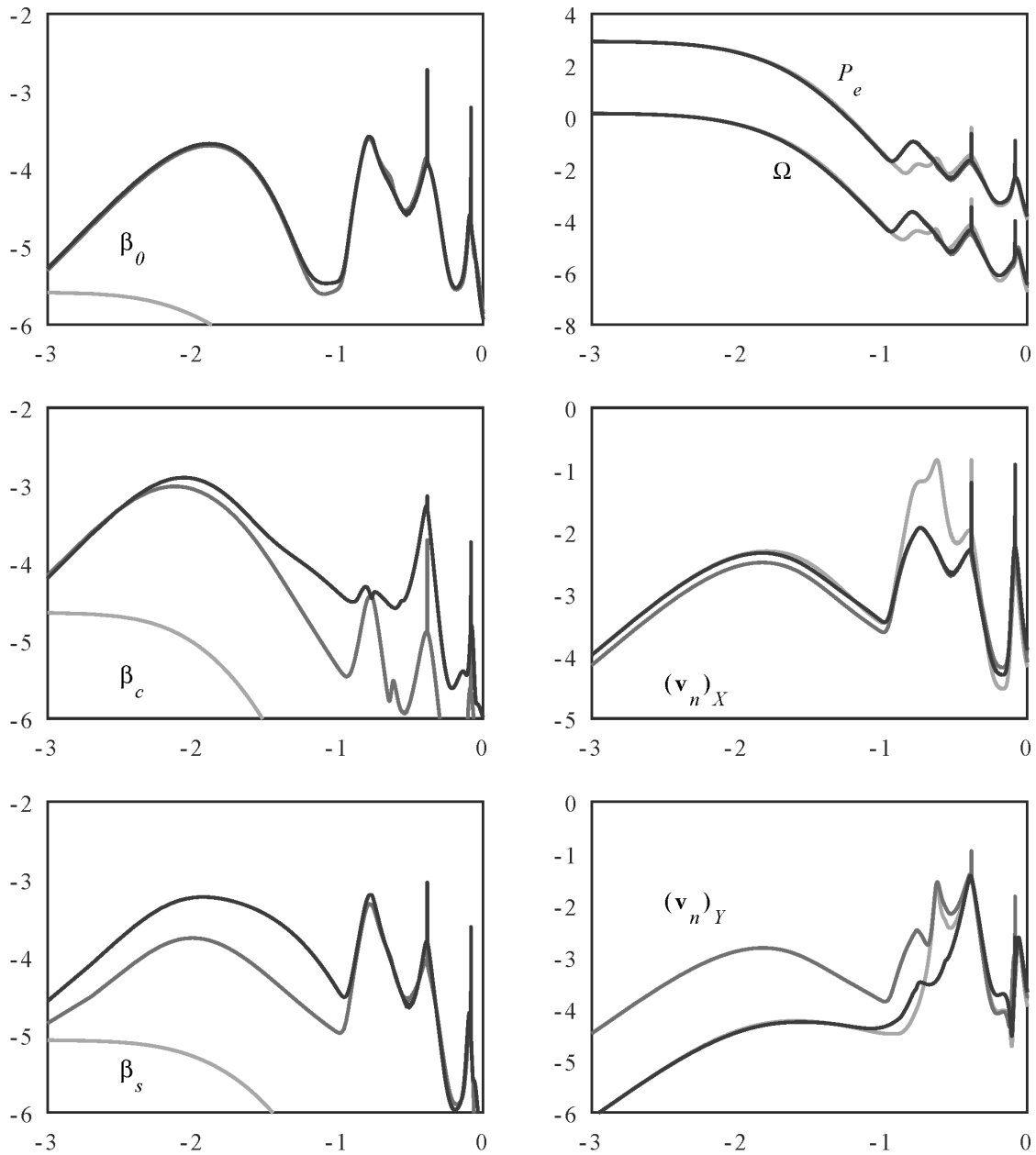REPORT NUMBER
2020:00257

VERSION
1.0

60 of 78

Figure 25: Case 10-2-30: Spectra of control actions and nacelle motions under realistic turbulent wind and ocean wave loading. Note that the tower motions are here shown in the global coordinate system (X downwind, Y cross-wind). Light: Controller RSC; medium: Controller AD2; dark: Controller IBP2.
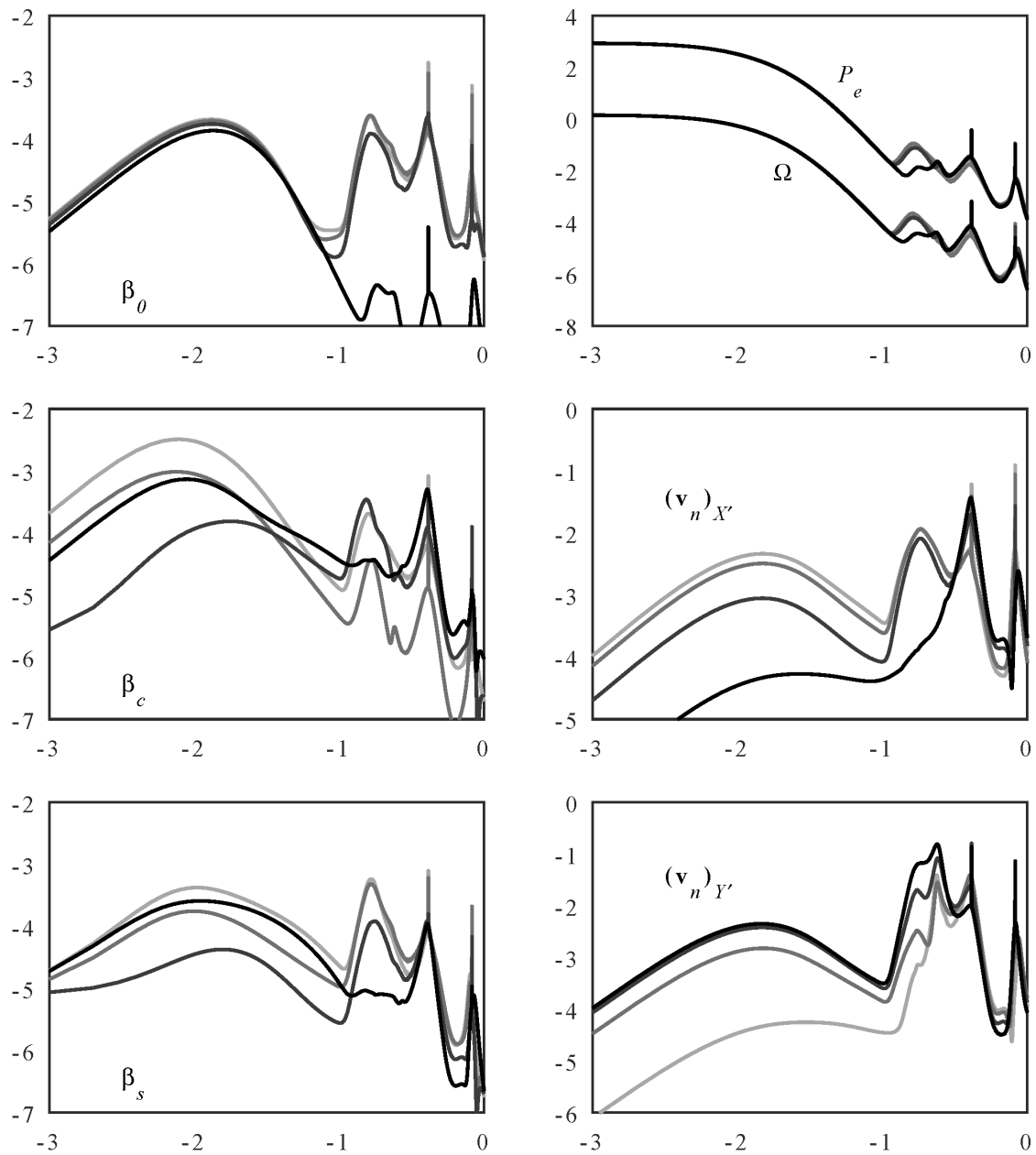
PROJECT
TotalControl

REPORT NUMBER
2020:00257

VERSION
1.0

61 of 78

Figure 26: Case 10-2-0, Controller IBP: Response spectra for the case where the wave and wind directions are aligned. The shading of the curves indicates the location of the defect: light is 0° and dark is 90°, with increments of 30°.

PROJECT
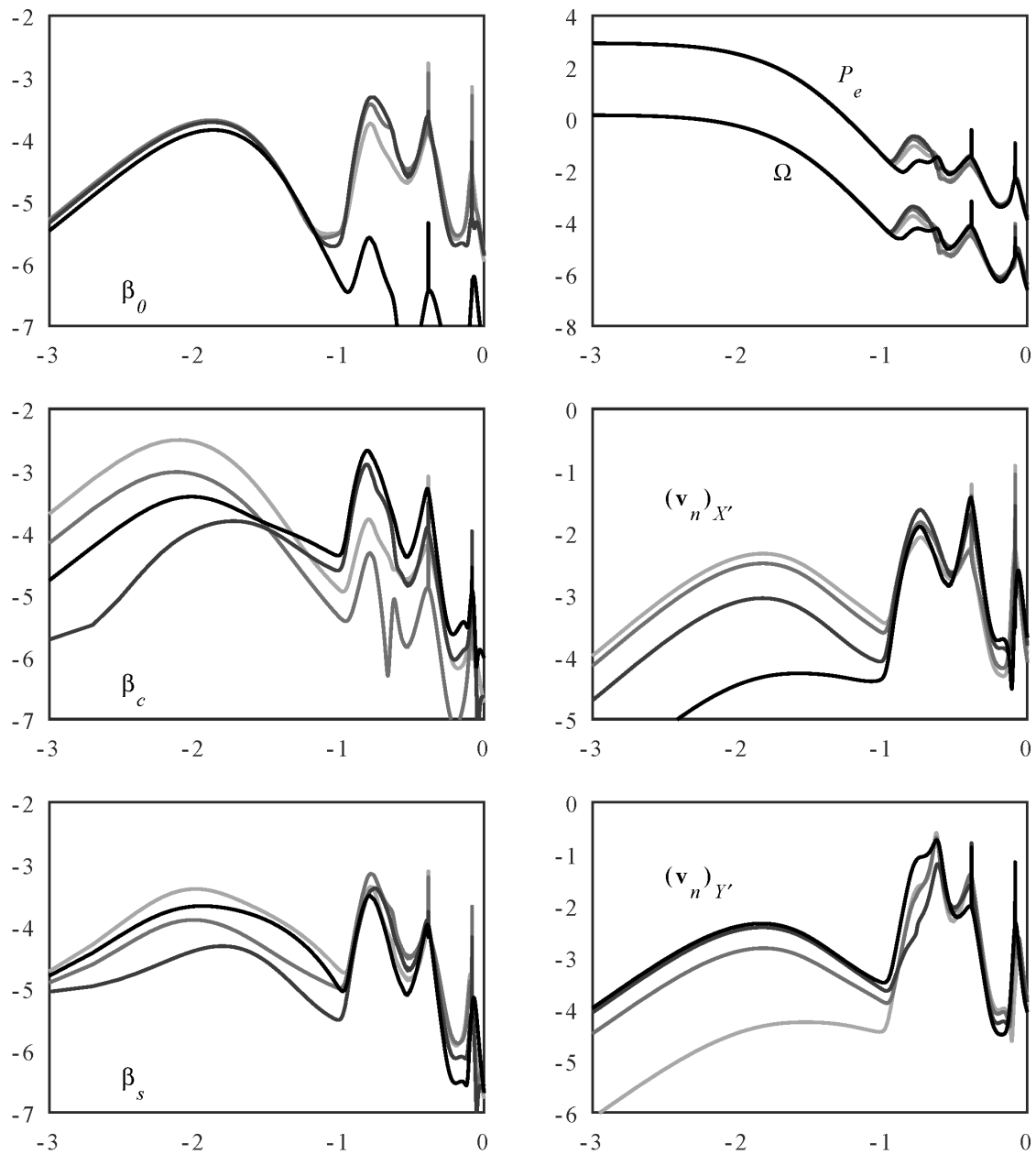TotalControl

REPORT NUMBER
2020:00257

VERSION
1.0

62 of 78

Figure 27: Case 10-2-30, Controller IBP: Response spectra for the case where the wave direction is offset by 30°. Light: defect is at 0°; dark: defect is at 90°.
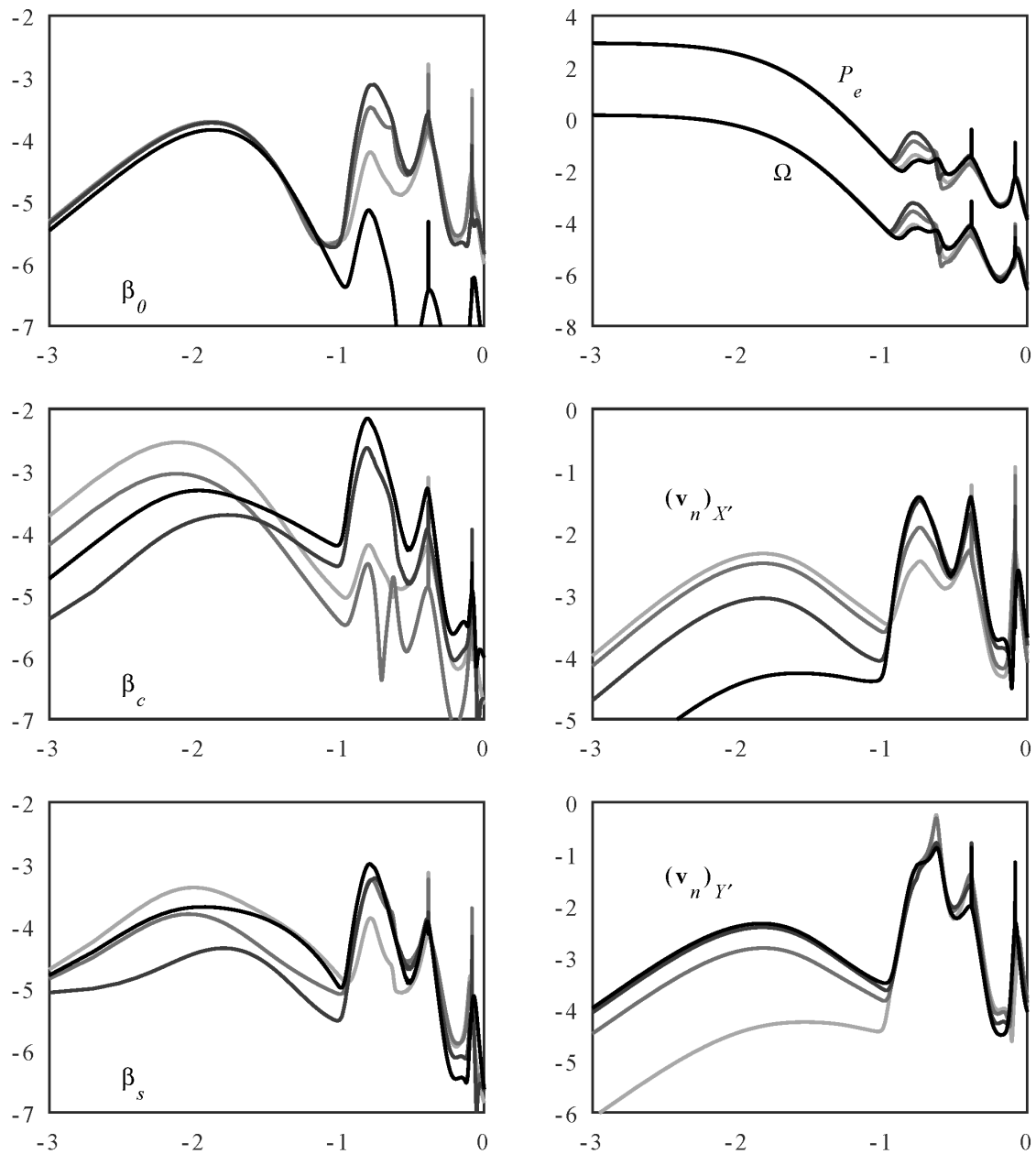
PROJECT
TotalControl

REPORT NUMBER
2020:00257

VERSION
1.0

63 of 78

Figure 28: Case 10-2-60, Controller IBP: Response spectra for the case where the wave direction is offset by 60°. Light: defect is at 0°; dark: defect is at 90°.

PROJECT
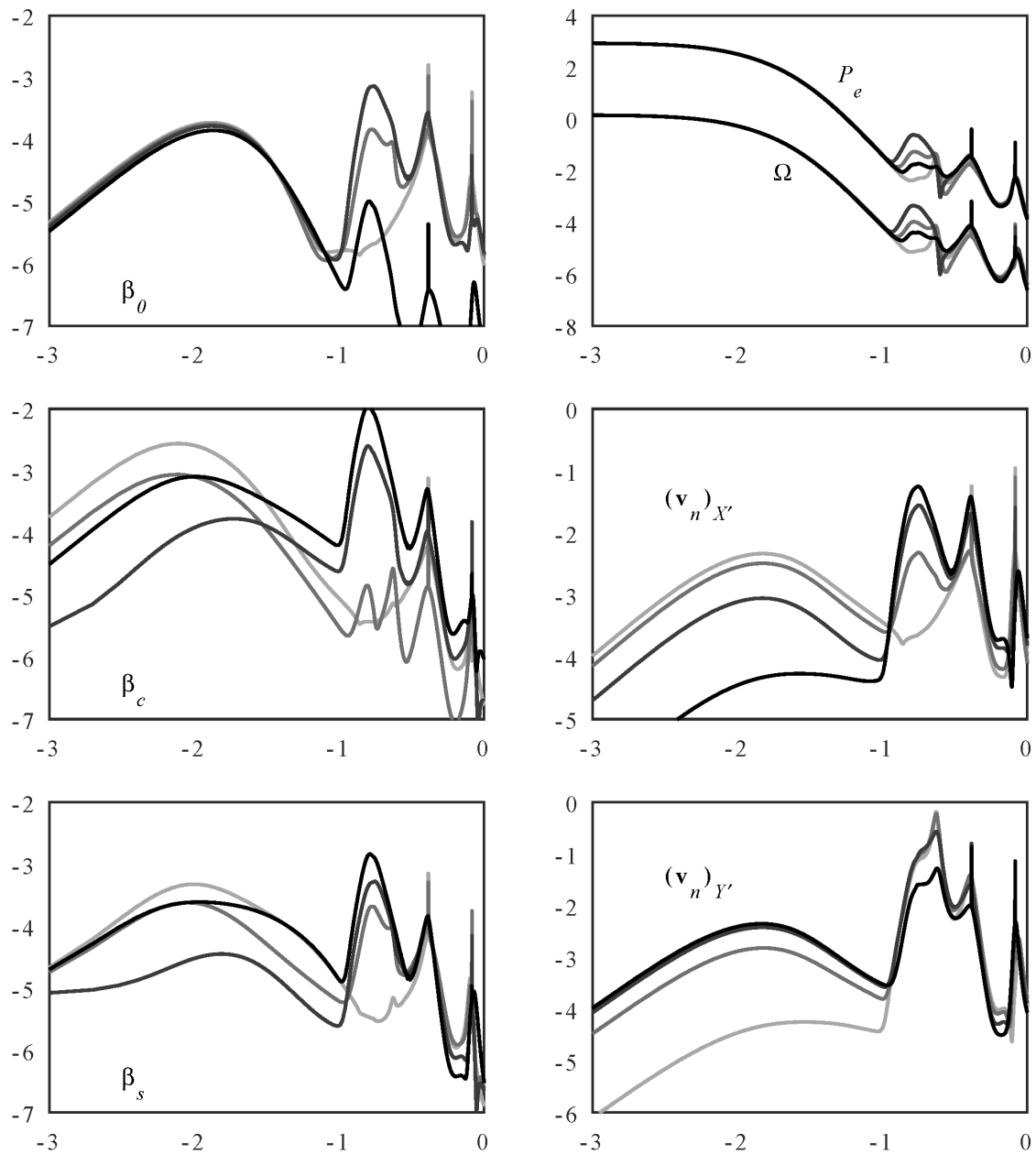TotalControl

REPORT NUMBER
2020:00257

VERSION
1.0

64 of 78

Figure 29: Case 10-2-90, Controller IBP: Response spectra for the case where the wave and wind directions are orthogonal. Light: defect is at 0°; dark: defect is at 90°.

PROJECT
TotalControl

REPORT NUMBER
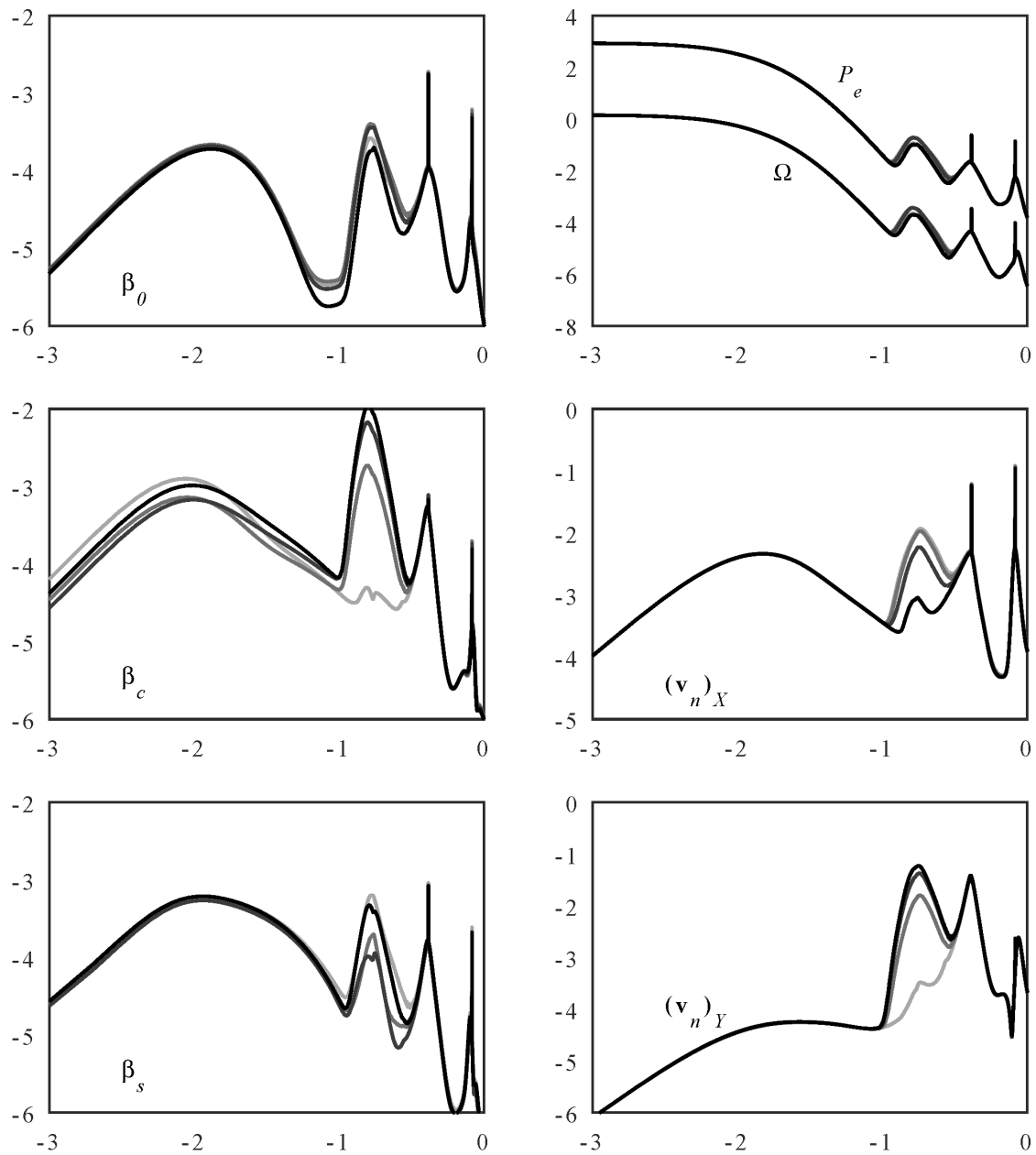2020:00257

VERSION
1.0

65 of 78

Figure 30: Case 10-2-30: Spectra of control actions and nacelle motions for Controller IBP2, under realistic turbulent wind and ocean wave loading, for wave directions of 0° (lighter shade), 30°, 60°, and 90° (darker shade).

PROJECT
TotalControl

REPORT NUMBER
2020:00257

VERSION
1.0

66 of 78

Table XVI: Case 2-3-0: Operating conditions selected for the investigation of active damping while idling.

Case	V_∞	Ω	$\beta_\emptyset$
2-3-0-1	2	0.1	14.0°
2-3-0-2	2	0.2	7.0°
2-3-0-3	2	0.3	4.7°

and effective controller is obtained if there is no directional preference, and all motions of the tower are rejected. Modulation of individual blade pitch provides a way to reduce tower motions without sending power fluctuations into the grid (Table VII).

5   Active load control of an idling wind turbine

When a wind turbine is idling in low winds, it loses much of the aerodynamic damping present during normal operation. The support structure is then prone to resonant oscillations excited by ocean waves. Despite the fact that the turbine is not generating power, it is conceivable to use active control to damp these oscillations. Two possibilities present themselves. One is to yaw the rotor such that it faces the incoming waves, and use the generator as a motor to spin up the rotor speed. The spinning rotor would then provide some aerodynamic damping. Another possibility is to yaw the rotor orthogonal to the waves, and use generator torque to oppose the "side-to-side" tower oscillations.

5.1   Aerodynamic damping control

Let the rotor be yawed such that it faces the direction from which the ocean waves approach; we assume long-crested seas for this conceptual study. The rotor is given some speed, either trimming the blade pitch, if there is a bit of wind, or else using the generator as a motor. What rotor speed should be chosen, and how effective is the blade pitch at damping the tower motions?

For this study we employ precisely the same control setup as in Section 4; the only change is the operating state of the wind turbine. Table XVI lists the three operating conditions considered. These were selected such that the rotor speed attained the desired value at a small margin above zero power.

Considering Case 2-3-0-2, where the rotor speed is 0.2 rad/s, transfer functions from wave load to the relevant control and response variables are shown in Fig. 31. Two sets of transfer functions are shown, comparing the baseline Controller RSC (Table XV) with Controller AD1. Engaging blade pitch increases the damping at resonance; it also has an influence on the rotor speed. As a consequence, the electric power fluctuations increase, particularly in the wave-frequency band.

Table XVII extends the comparison of Controllers RSC and AD to rotor speeds of 0.1 and 0.3 rad/s. It appears as though an idling speed between 0.2 and 0.3 rad/s allows the active damping control to be fully effective. This can be seen at the lower left of Fig. 32: the resonant peak in Case 2-3-0-3 is mostly eliminated. The dashed curves in Fig. 32 are the integrals under the spectra, whose final value is the variance. From this, we can discern that the standard deviation of blade pitch is around 0.01 rad, or about 0.6°.

5.2   Generator damping control

The effectiveness of the active damping strategy of Section 5.1 is a strong function of the rotor speed. It is ineffective when the rotor is rotating slowly, below around 0.2 rad/s. Keeping the rotor spinning at a high rate comes at a cost, if the winds are low and variable and the generator must be used as a motor. An alternate strategy that is not so dependent on the rotor speed is to yaw the turbine orthogonal to the prevailing wave direction, and apply some combination of individual blade pitch and generator torque.

PROJECT
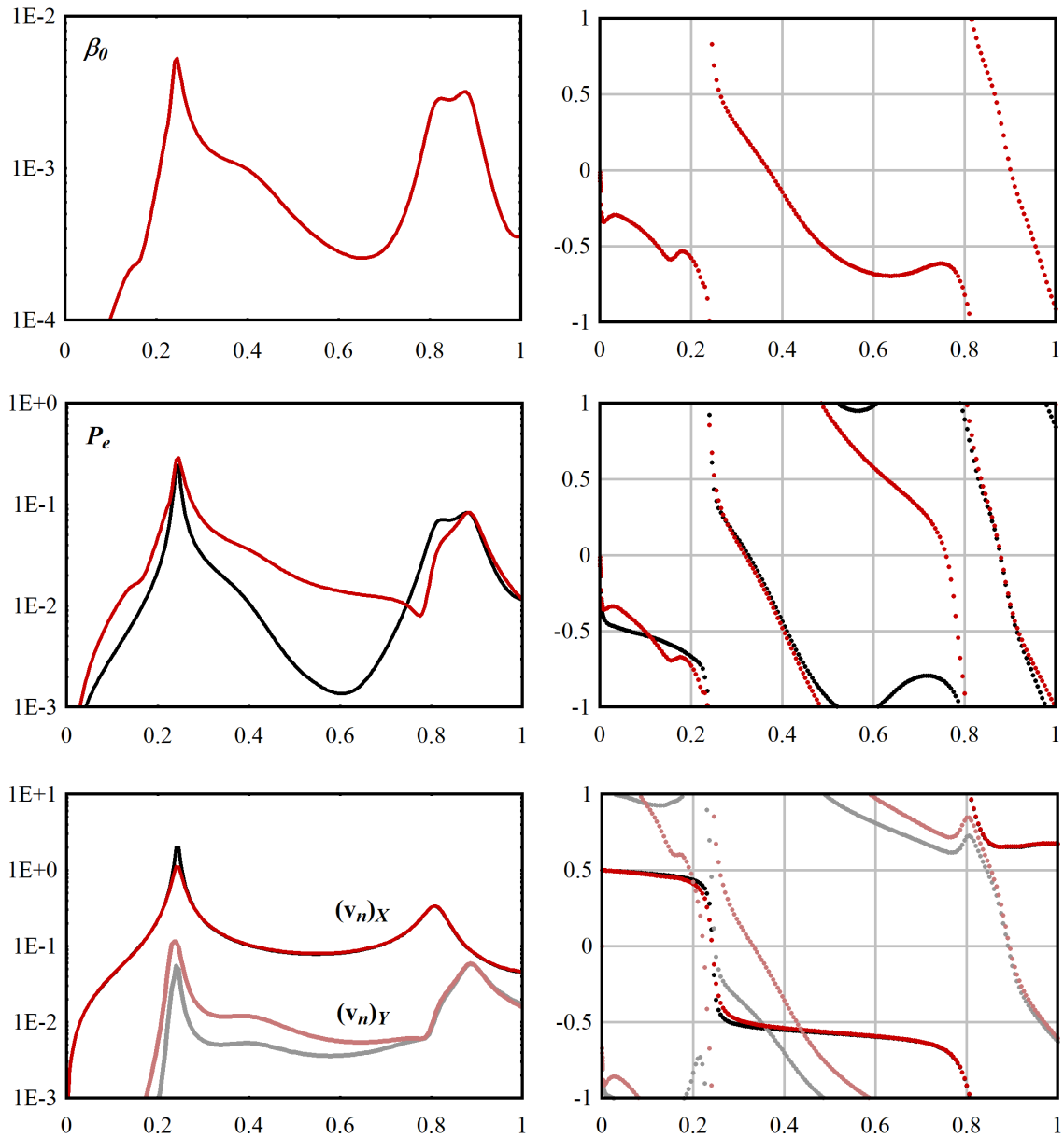TotalControl

REPORT NUMBER
2020:00257

VERSION
1.0

67 of 78

Figure 31: Case 2-3-0-2: Transfer functions from wave load to blade pitch (upper row), electric power (middle row), and nacelle velocities (lower row). The X axes in this and subsequent figures are scaled linearly (not logarithmically as in previous sections), and have units of Hz. Black curves: baseline case, Controller RSC (blade pitch is zero in the upper plots). Red curves: Controller AD.

Table XVII: Case 2-3-0: Modal properties of tower resonance, with and without active damping.

Controller	Case	Fore-aft		Side-to-side	
		f	ζ	f	ζ
RSC	2-3-0-1	0.242	0.012	0.226	0.026
RSC	2-3-0-2	0.242	0.020	0.228	0.035
RSC	2-3-0-3	0.242	0.027	0.229	0.041
AD	2-3-0-1	0.242	0.014	0.226	0.026
AD	2-3-0-2	0.242	0.040	0.228	0.035
AD	2-3-0-3	0.241	0.082	0.229	0.040

PROJECT
TotalControl

REPORT NUMBER
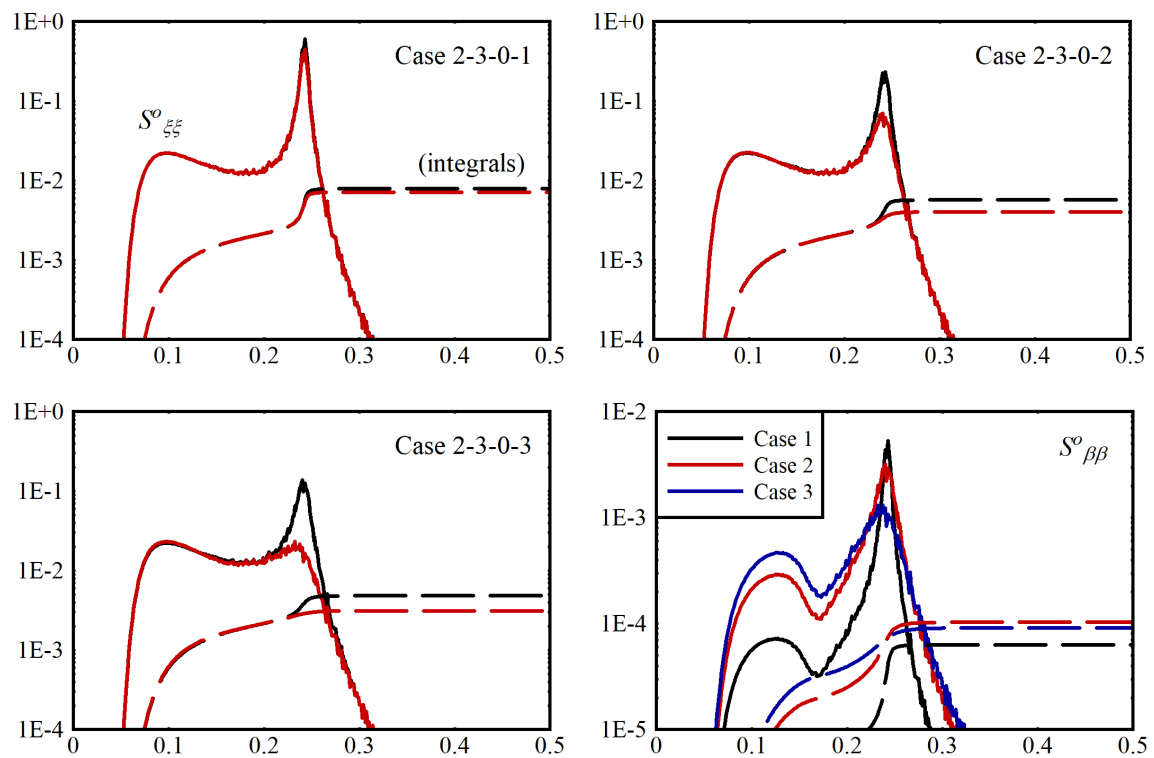2020:00257

VERSION
1.0

68 of 78

Figure 32: Case 2-3-0: Spectra of nacelle X displacement, for three rotor speeds, with and without active damping control. The plot at lower right shows the spectra of collective blade pitch for the same three cases.

PROJECT
TotalControl

REPORT NUMBER
2020:00257

VERSION
1.0

69 of 78

Table XVIII: Case 2-3-90: Tuning of the controller for active damping with the generator, while idling. RSI: rotor speed control, GI1: pure tower damping, GI2: tower damping with rotor speed control, ADI: active tower damping using the generator and collective pitch, IBI: same as ADI, plus individual blade pitch.

	RSI	GI1	GI2	ADI	IBI
ε_P	2	**0.2**	2	2	2
$\dot{\varepsilon}_P$	0	0	0	0	0
Ψ_P	10	**1**	**25**	25	25
$\dot{P}_e$	0.5	0.5	0.5	0.5	0.5
$\dot{\Omega}$	0	0	0	0	0
$(\mathbf{v}'_n)_X$	0	**15**	**20**	20	20
$(\mathbf{v}'_n)_Y$	0	**15**	**20**	20	20
$\dot{\beta}_\emptyset$	0	0	0	**10**	10
$\dot{\beta}_c$	0	0	0	0	**10**
$\dot{\beta}_s$	0	0	0	0	**10**
$\Psi_{\beta\emptyset}$	0	0	0	**20**	20
$\Psi_{\beta c}$	0	0	0	0	**1**
$\Psi_{\beta s}$	0	0	0	0	**1**
ε_χ	0	0	0	0	0
$\dot{\varepsilon}_\chi$	0	0	0	0	0
Ψ_χ	0	0	0	0	0
$\hat{\beta}_\emptyset$	(big)	(big)	(big)	**50**	50
$\hat{\beta}_c$	(big)	(big)	(big)	(big)	**50**
$\hat{\beta}_s$	(big)	(big)	(big)	(big)	**50**
$\hat{P}_e$	1	1	1	1	1
$\hat{\chi}$	(big)	(big)	(big)	(big)	(big)

Table XIX: Case 2-3-90: Modal properties of tower resonance, as a function of the active damping control strategy. Here the target rotor speed was 0.15 rad/s, and the mean blade pitch was 14°.

Controller	Fore-aft		Side-to-side	
	f	ζ	f	ζ
RSI	0.242	0.013	0.226	0.027
GI1	0.242	0.014	0.217	0.013
GI2	0.242	0.013	0.225	0.031
ADI	0.242	0.022	0.225	0.031
IBI	0.241	0.030	0.225	0.036

Simply opposing the nacelle velocity with a power command does not work. Such a scheme is implemented by Controller GI1 (G for "generator", I for "idling") in Table XVIII. Table XIX shows that the result is a decrease in damping, with respect to a baseline control strategy (RSI) without active load control. The reason for the poor performance is visible in the transfer functions of Fig. 33, where the phase of the electrical power is at 90° relative to the rotor speed. This implies that the generator is dissipating little power, rather it is transferring the power back and forth to the rotor. A successful active damping strategy, Controller GI2, adjusts the phase of the electrical power and speed through the Ψ_P penalty. With this tuning, there is a component of the electrical power in-phase with the speed: the generator is dissipating some of the rotor's kinetic energy. There is also a component in-phase with the tower side-to-side velocity, providing the desired damping.

Even at a low rotor speed of 0.15 rad/s, engaging blade pitch has some effect, as seen in the spectra of nacelle displacements, Fig. 34. Individual blade pitch further reduces the side-to-side motion by a small amount.

PROJECT
TotalControl
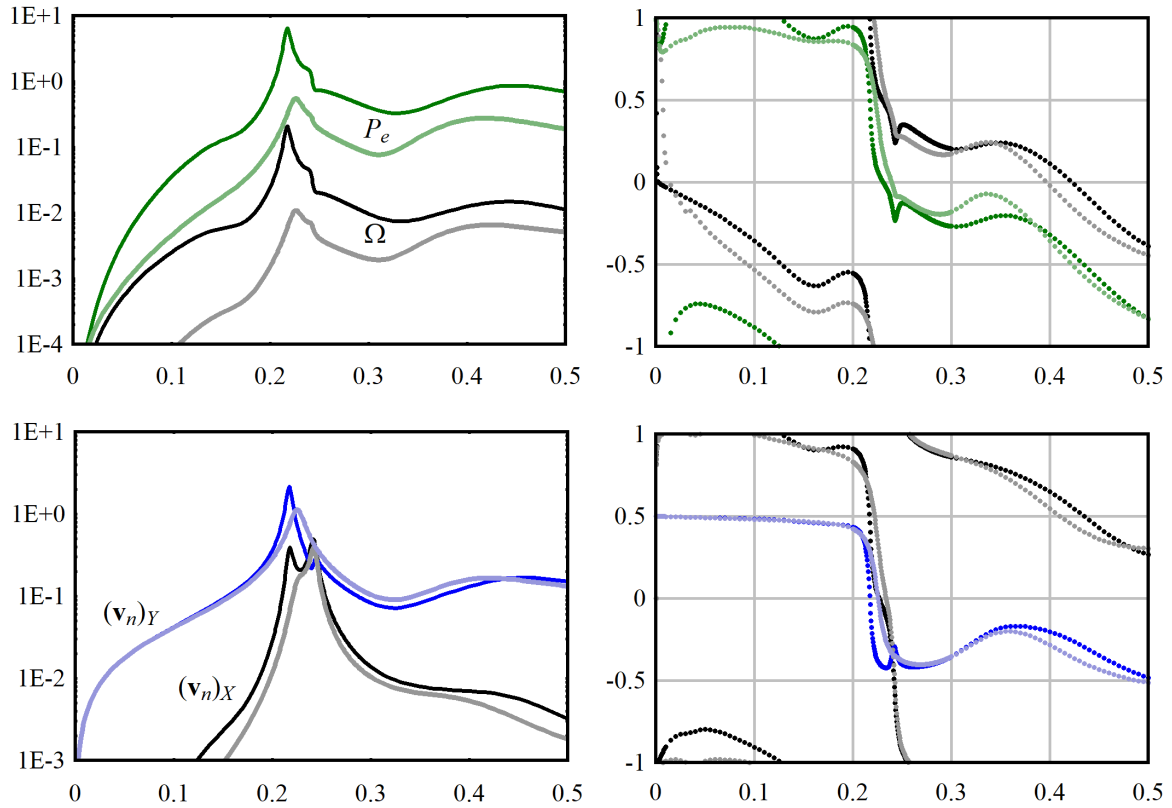
REPORT NUMBER
2020:00257

VERSION
1.0

70 of 78

Figure 33: Case 2-3-90: Transfer functions from wave load to rotor speed, electrical power, and nacelle motions, comparing Controllers GI1 (darker curves) and GI2 (lighter curves).
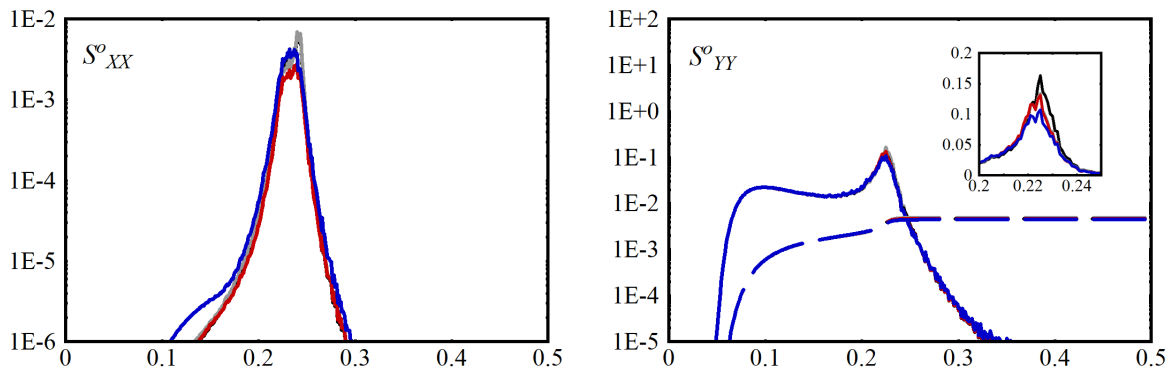

Figure 34: Case 2-3-90: Spectra of nacelle displacements obtained with selected controllers from Table XVIII. Gray: RSI. Black: GI2. Red: ADI. Blue: IBI. Dashed lines in the right-hand plot show the integrals, whose terminal value is the variance σ^2.

PROJECT
TotalControl

REPORT NUMBER
2020:00257

VERSION
1.0

71 of 78

6   Robustness of the resulting controllers

The controllers of Sections 4 and 5 were designed using a model of the plant that was closely similar to the nominal model – at least, in terms of the control-to-sensor and disturbance-to-sensor transfer functions. In practice there will be unavoidable discrepancies between the embedded model in the controller, and the actual wind turbine. A robust controller will be insensitive to these discrepancies.

There are a variety of types of modelling error, and a number of ways in which we can test and evaluate robustness. (Stengel 1994, Zhou *et al.* 1996) Mathematical approaches to robustness place much emphasis on stability, because it is a generic requirement for all systems and also comparatively easy to evaluate. There are certain formal guarantees about stability margins obtained with LQR control synthesis, but these are strictly valid only for the plant model with which the controller was synthesized. Tests for stability, and to some extent performance, under perturbations in the system parameters can be formulated in terms of singular values of closed-loop transfer functions. Stability is a necessary condition for good performance; but it is neither sufficient nor conservative, from an engineering standpoint, since the system is likely to exhibit poor performance well before becoming unstable. For instance, engaging an active damping controller that increased the rate of fatigue would be a colossal failure, even if the system remained stable and operational.

A crude but sure way to gauge the performance of the controller is to hook it up to a set of representative system models and test it. Some of the most likely and significant ways in which a real wind turbine could differ from the modelled version, in terms of the potential impact on the present control algorithms, are

1. The foundation conditions: There is uncertainty in the mechanical properties of the seabed. Not only is the monopile hammered into an uncertain substrate, but the properties change over time, in particular due to seabed erosion, and working in response to tower displacements. This is reflected in the natural frequency of the support structure.

2. Pitch actuator dynamics: Simple filters and spring-damper elements have been used to represent the actuator dynamics, whereas the real actuators are electromechanical devices with many subcomponents. In a real application the properties of the servos would be determined by testing, and would therefore be known; but some allowance is needed for degradation under long-term operation, or alterations as a result of maintenance.

3. Sensor degradation or failure: A sensor signal may accumulate a bias over time, or perhaps a corroded connection or electromagnetic interference leads to unanticipated noise in the channel.

The aerodynamic surfaces of the blades may also degrade over time, particularly at the outboard leading edge, which effects the effective lift and drag coefficients. This will impact performance, but it is not something that can be remedied by control, and it is not expected to influence stability.

The controllers of Sections 4 and 5 are not complete: they are prototypes that are valid around particular operating points.[21] Our consideration of robustness is limited to the same, and should be viewed as indicative. An evaluation over the full range of operation is outside the present scope. For illustration of robustness, focus is placed on the foundation and pitch actuator characteristics, for active load control during operation, using Controller IBP2 of Section 4.

Assuming that we have not been altogether too aggressive in setting the gains, we can expect that the linear optimal control will be less sensitive to errors in system parameters than an equivalent controller constructed from simple band-pass and notch filters. This was the conclusive finding of Fleming *et al.* (2013), and also a rational outcome of the use of the system model itself as a filter.

Indeed, we find that the controller of Section 4 is not sensitive to errors in the foundation properties, nor the pitch actuator dynamics. The foundation stiffness was perturbed by $\pm 10\%$, giving the modal

---

[21]To arrive at a complete controller would require additional control logic to schedule gains; transitions between operating modes; possibly hysteretic exclusion zones to avoid key resonant frequencies; shut-down, startup, and safety functions; and so forth.

PROJECT
TotalControl

REPORT NUMBER
2020:00257

VERSION
1.0

72 of 78

Table XX: Case 10-2-30: The influence of the foundation stiffness on the first resonant mode of the open-loop turbine. The stiffness factor was applied to the bending stiffness of the foundation and tower.

Factor	Fore-aft		Side-to-side	
	f	ζ	f	ζ
0.9	0.234	0.082	0.229	0.032
1.0	0.243	0.080	0.236	0.035
1.1	0.252	0.075	0.246	0.038

properties listed in Table XX. These are significant changes, larger than would be expected from normal processes of erosion or degradation of the foundation. Using the original controller, designed for the original stiffness, the resulting performance is shown in Fig. 35. There is hardly any change; the sensors detect the tower motion at its perturbed frequency, and the controller acts to compensate. Similarly, Fig. 36 shows the case where the corner frequency of the low-pass filter representing the limits of the pitch actuator was halved from 1 Hz to 0.5 Hz – that is, the characteristic response time was slowed from 1 s to 2 s. The original controller performs well; it is robust to alterations in the pitch actuator dynamics.

7 Conclusions

We have investigated a "top-down" strategy of control synthesis, and applied this to load-reducing control functions for offshore wind turbines. The usual, bottom-up approach to model-based control begins with a highly simplified physical model of the plant, the order of 10 state variables being typical for wind turbine applications. By contrast, the top-down approach begins with a high-resolution model of the plant, the one employed here having around 300 state variables.[22]

It was found that a top-down control design is workable, and useful for rapid prototyping of offshore wind turbine controllers. It was not difficult to ensure controllability and observability, for which modal analysis is the key; the algebraic Riccatti equation could be solved rapidly, even with 300 states; the resulting gain matrices could not be understood, but the performance could be quickly evaluated using transfer functions and spectral analysis.

It is not claimed that it is necessary to begin with a high-resolution model; simple observer models can result in good controllers, and are, naturally, simpler to work with. But by proceeding top-down we gain some advantages. We can be certain – at least, more certain than with other approaches – that the model includes the relevant dynamics. We can always reduce the order of the controller after synthesis, and formally quantify how much accuracy has been lost, and where. More subtly, and interestingly, there is the possibility that the synthesis of an optimal controller around a high-resolution model will find an unexpected control action that can improve performance. We encountered an example of this in Section 4, where the controller used modulation of individual blade pitch to augment load rejection over the resonant- and wave-frequency bands. This was in no way designed into the approach; rather, it was a natural outcome of the optimization. There exist many low-resolution control models that would not have found this solution.

Directional fatigue control of offshore wind turbine foundations does not appear to be especially promising, as better performance was obtained when rejecting loads omnidirectionally. There could be niche cases where some advantage of directional control, like reduced actuator usage, might be realized. We investigated the two bounding cases: full directional bias and no directional bias. It could be of interest to look at some of the intermediate scenarios, and perhaps other wind-wave climates.

It is practical to actively damp the wave-induced response of an offshore wind turbine when idling. Which strategy is preferred – yawing into the waves and using blade pitch, or yawing perpendicular to

---

[22]...and this *after* reducing the "full" structural and aerodynamic models through modal decomposition.
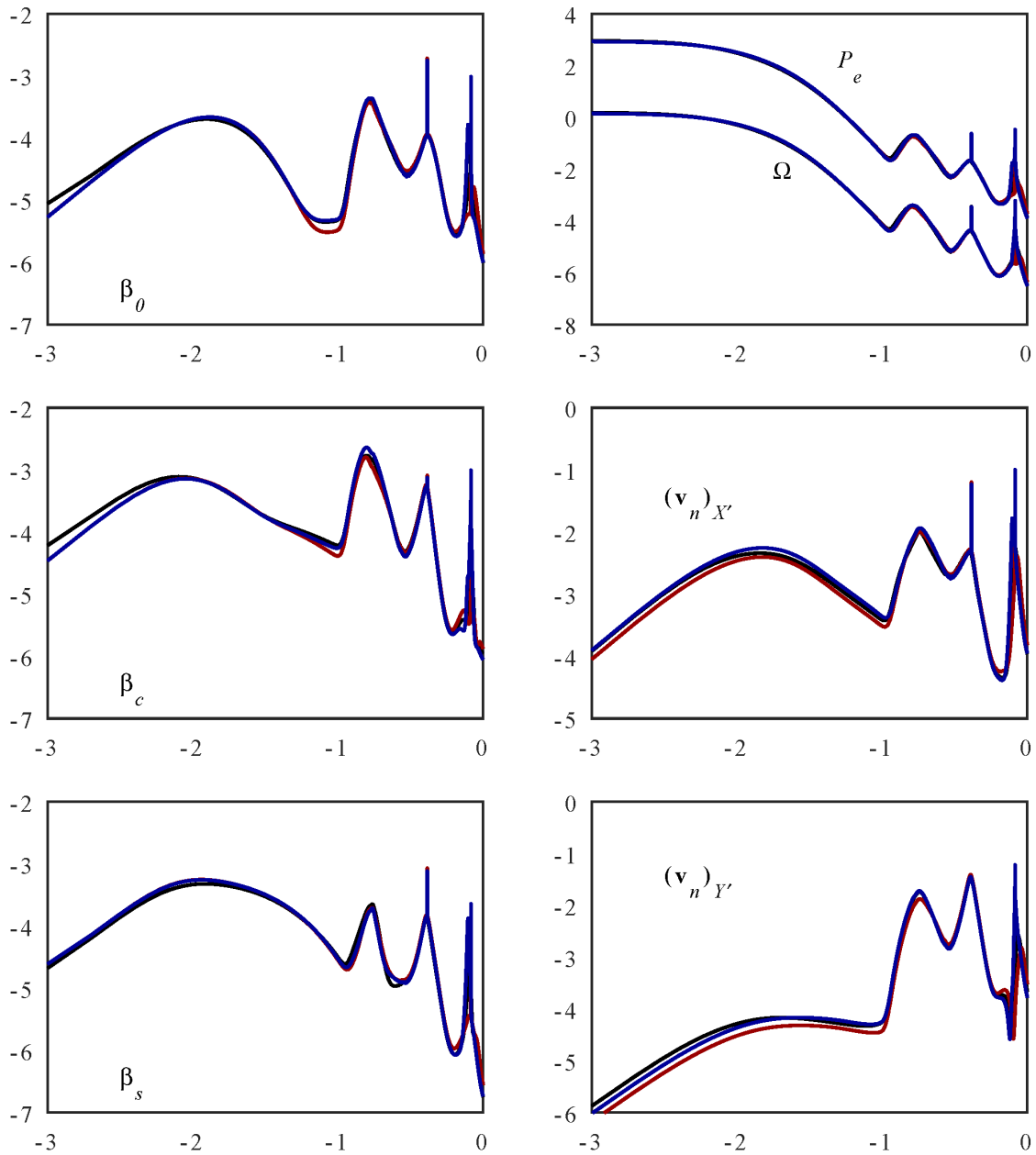
Figure 35: Case 10-2-30: Control and response spectra, showing the influence of changing the foundation stiffness, while keeping the original observer and controller gains. Black: original, blue: 90% stiffness, red: 110% stiffness.
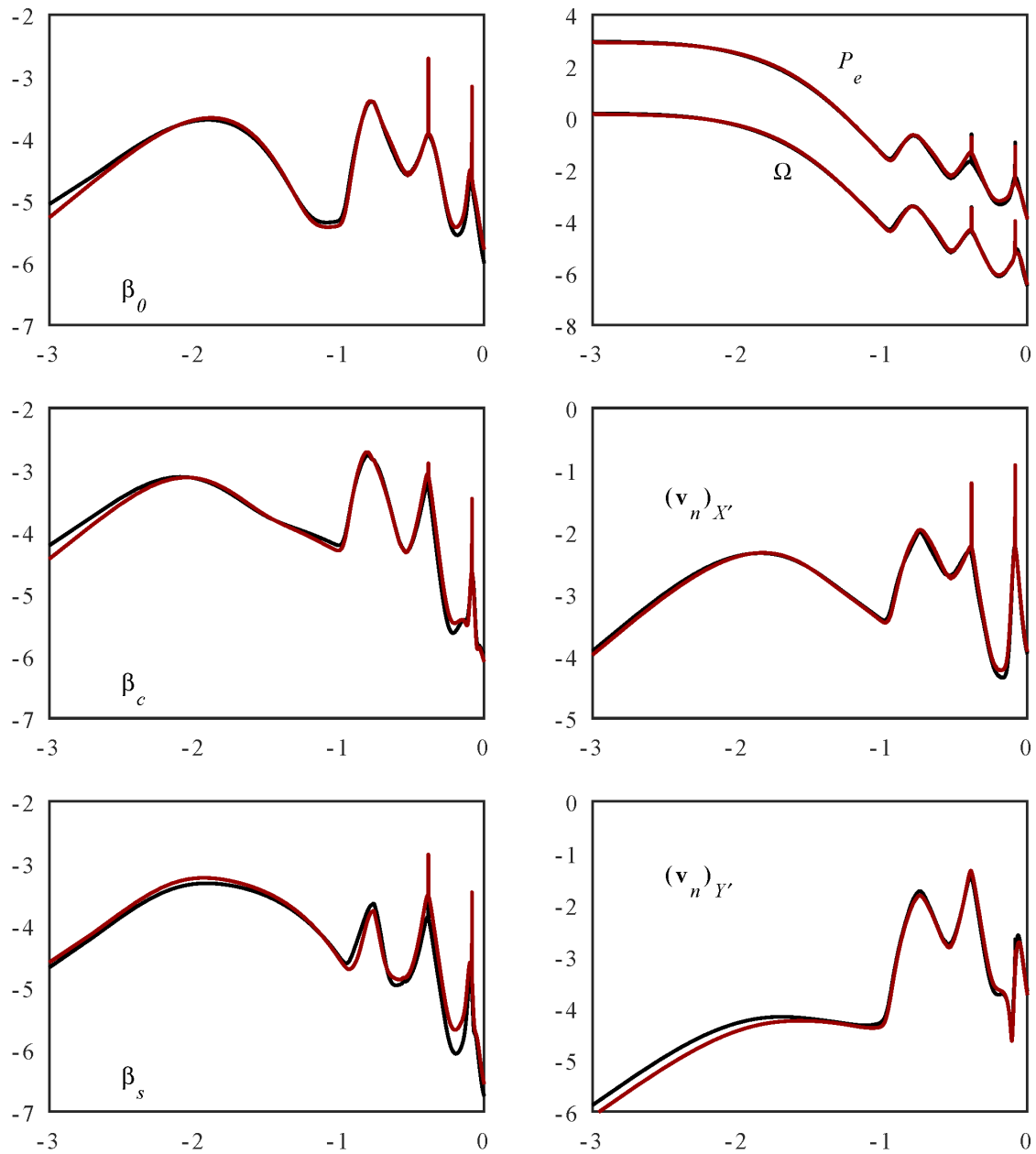
PROJECT
TotalControl

REPORT NUMBER
2020:00257

VERSION
1.0

74 of 78

Figure 36: Case 10-2-30: The influence of the pitch actuator responsiveness on performance. Black: $\alpha_\beta = 1$ Hz. Red: $\alpha_\beta = 0.5$ Hz.

PROJECT
TotalControl

REPORT NUMBER
2020:00257

VERSION
1.0

75 of 78

the waves and using the generator – depends on how fast the rotor can be spun. This in turn depends on the wind speed, its variability, and its direction relative to the waves. The best approach could be to include both options in the wind turbine controller, and apply one, the other, or neither, as wind and wave conditions dictate.

Acknowledgements

References

Anaya-Lara O, *et al.* (2018). *Offshore Wind Energy Technology*. Wiley.

Athans M, Falb PL (1966). *Optimal Control – An Introduction to the Theory and Its Applications*. McGraw-Hill.

Athans M, Tse E (1967). A direct derivation of the optimal linear filter using the maximum principle. IEEE Transactions on Automatic Control 6: 690-698.

Bak C, *et al.* 2013. *Description of the DTU 10 MW Reference Wind Turbine*. DTU Wind Energy Report-I-0092, Technical University of Denmark.

Bir G (2008). Multiblade coordinate transformation and its application to wind turbine analysis. Paper NREL/CP-500-42553, National Renewable Energy Laboratory. Presented at the ASME Wind Energy Symposium, Reno, NV, USA, January 7-10, 2008.

Blevins RD (1990). *Flow-Induced Vibration*. Second Edition, Van Nostrand Reinhold.

Bossanyi E (2003). Wind turbine control for load reduction. Wind Energy 6: 229-244.

Bottasso C, *et al.* (2013). Multi-layer control architecture for the reduction of deterministic and non-deterministic loads on wind turbines. Renewable Energy 51: 159-169.

Burton T, *et al.* (2001). *Wind Energy Handbook*. Wiley.

Connell JR (1982). The spectrum of wind speed fluctuations encountered by a rotating blade of a wind energy conversion system. Solar Energy 29: 363-375.

Davidson PA (2004). *Turbulence – An Introduction for Scientists and Engineers*. Oxford University Press.

Fischer T, *et al.* (2010). *Upwind Design Basis*. EU UpWind Project.

Fleming PA, *et al.* (2013). Field testing a wind turbine drivetrain/tower damper using advanced design and validation techniques. Americal Control Conference, Washington, DC, USA, 17-19 June, 2013.

Fossen TI (1994). *Guidance and Control of Ocean Vehicles*. Wiley.

Friedland B (1986). *Control System Design – An Introduction to State-Space Methods*. McGraw-Hill.

Hansen MH, Henriksen LC (2013). *Basic DTU Wind Energy Controller*. Report DTU Wind Energy E-0028, Technical University of Denmark.

Johnson W (1994). *Helicopter Theory*. Dover.

Jonkman J, *et al.* (2009). *Definition of a 5-MW Reference Wind Turbine for Offshore System Development*. Report NREL/TP-500-38060, National Renewable Energy Laboratory.

Kristensen L, Frandsen S (1982). Model for power spectra of the blade of a wind turbine measured from the moving frame of reference. Journal of Wind Engineering and Industrial Aerodynamics 10: 249-262.

Kundur P (1994). *Power System Stability and Control*. McGraw-Hill.

Liebst BS (1985). A pitch control system for the KaMeWa wind turbine. Journal of Dynamic Systems, Measurement, and Control 107: 47-52.

Merz KO (2015a). Environmental loads for frequency-domain aeroelastic analysis of offshore wind turbines. Memo AN 15.12.19, SINTEF Energy Research.

Merz KO (2015b). Design verification of the drivetrain, support structure, and controller for a direct-drive, offshore version of the DTU 10 MW Reference Wind Turbine. Memo AN 15.12.68, SINTEF Energy Research.

Merz KO (2015c). *A Linear State-Space Model of an Offshore Wind Turbine, Implemented in the STAS Wind Power Plant Analysis Program*. Report TR A7474, SINTEF Energy Research.

Merz KO (2018). *STAS Aeroelastic 1.0 – Theory Manual*. Report 2018:00834, SINTEF Energy Research.

Merz KO (2019). STAS Electric 1.0 – Theory Manual. Memo AN 19.12.07, SINTEF Energy Research.

Merz KO, Pedersen MD (2018). Offshore wind turbine controls. Chapter 5 of Anaya-Lara *et al.*, *Offshore Wind Energy Technology*. Wiley.

Merz KO, *et al.* (2019). *An Electromechanical Model of the TotalControl Reference Wind Power Plant*. Report 2019:00342, SINTEF Energy Research.

Mulders SP, van Wingerden JW (2018). Delft Research Controller: an open-source and community-driven wind turbine baseline controller. Journal of Physics: Conference Series 1037: 032009.

Munteanu I, *et al.* (2005). Optimization of variable speed wind power systems based on a LQG approach. Control Engineering Practice 13: 903-912.

Reistad M, *et al.* (2009). *A high-resolution hindcast of wind and waves for The North Sea, The Norwegian Sea, and The Barents Sea*. Report 2009/14, Norwegian Meteorological Institute.

Schultz DG, Melsa JL (1967). *State Functions and Linear Control Systems*. McGraw-Hill.

Smilden E (2019). *Structural control of offshore wind turbines – Increasing the role of control design in offshore wind farm development*. PhD Thesis, Department of Marine Technology, Norwegian University of Science and Technology.

Smilden E, *et al.* (2019). Wave disturbance rejection for monopile offshore wind turbines. Wind Energy 22: 89-108.

Stengel RF (1994). *Optimal Control and Estimation*. Dover.

Stevens BL, Lewis FL (2003). *Aircraft Control and Simulation*. Second Edition, Wiley.

PROJECT
TotalControl

REPORT NUMBER
2020:00257

VERSION
1.0

77 of 78

van der Hooft EL, *et al.* (2003). *Wind Turbine Control Algorithms*. Report ECN-C--03-111, Energy Research Centre of the Netherlands.

Wright A (2004). *Modern Control Design for Flexible Wind Turbines*. Report NREL/TP-500-35816, National Renewable Energy Laboratory.

Zhou K, Doyle JC, Glover K (1996). *Robust and Optimal Control*. Prentice Hall.